QUASIFREE ELECTROPRODUCTION OF Λ, Σ^o, AND Σ^- HYPERONS ON CARBON AND ALUMINUM

A Dissertation

By

WENDY LATRECE HINTON

Submitted to the Graduate College of
Hampton University
in partial fulfillment of the requirements
for the degree of

DOCTOR OF PHILOSOPHY

May 2001

This dissertation submitted by Wendy LaTrece Hinton in partial fulfillment of the requirements for the degree of Doctor of Philosophy at Hampton University, Hampton, Virginia, is hereby approved by the committee under whom the work has been completed.

Liguang Tang, Ph. D.
Chair

Oliver K. Baker, Ph. D.

Rolf Ent, Ph. D.

Dave Mack, Ph. D.

Rodney D. Smith, Ed. D.
Vice President for Planning and
Dean of the Graduate College

Date

ABSTRACT

Quasifree Electroproduction of Λ, Σ^o, and Σ^- Hyperons on Carbon and Aluminum. (August 2001)

Wendy LaTrece Hinton, B.S., Washington and Lee University;

M.S., Hampton University; Ph.D., Hampton University

Chair of Advisory Committee: Dr. Liguang Tang

The first study of (e, e$'$ K$^+$) on carbon and aluminum was performed at Thomas Jefferson National Accelerator Facility (Jefferson Lab) using the Continuous Electron Beam Accelerator Facility (CEBAF). The scattered electron and electroproduced kaon were detected in coincidence in the Hall C end station using the High Momentum Spectrometer and Short Orbit Spectrometer. The quasifree production of the Λ, Σ^0, and Σ^- hyperons was studied. The A-dependences of the effective nucleon number was obtained. The cross section data were fit to a power law ($\approx$ A$^\alpha$) with $\alpha = 0.88 \pm 0.10$, consistent with the K$^+$'s relatively long nuclear mean free path. A large enhancement in the $\frac{\Sigma^0+\Sigma^-}{\Lambda}$ ratio is seen. A feasibility test for hypernuclear spectroscopy on ^{12}C and ^{27}Al with the HMS-SOS was performed.

DEDICATION

To my parents George and Emma Hinton.

And

My spiritual parents Pastor Robert and Patricia Baker

... perplexed, but not in despair; ... II Cor. 4:8

ACKNOWLEDGMENTS

First giving thanks to my Lord and Savior Jesus Christ. I wish to thank my father and mother, George and Emma Hinton for their love and support. Thanks to my brothers, Gregory and Le'Ondra Hinton, nephews Danté and Desmond Hinton. My cousin Liza Peterson-Faunt and the entire Pinchem-Hinton family for all of their love and encouragement. I would also like to thank my spiritual parents Pastor and Mother Baker and my entire spiritual family of Christ Church for their prayers and encouragements. Thanks to the E91-16 and E93-18 collaborations and spokespersons Ben Zeidman and Keith Baker for allowing me the time to run this experiment and for all their help. Thanks to the Hall C scientists and technicians Dave Mack, Steve Wood, Bill Vulcan, Chen Yan, Hamlet Mkrtchyan, Joe Beaufait and Joe Mitchel for their nuggets of wisdom and help. Thank you to my advisor Dr. Liguang Tang for all his help and words of advice. Special thanks to Dr. Keith Baker (*Mr. Encouragemanet himself*), and the Hampton postdocs especially Paul Gueye, Ketevi Assamagan and Robert Williams for all of their help and support. I would like to thank the staff and faculty of Hampton University Carlane Pitman, Vevelyn Nazario, Dr. Donald

Whitney, Dr. Jose Goity, Dr. Khin Maung Maung, Dr. Cynthia Keppel and Dr. Demetrius Venable. Thank you to my undergraduate professors at Washington and Lee University for not giving up on me Prof. Ronald Reese and Prof. Thomas William. I also would like to thank the Hampton students especially Mark Harvey, Steve Avery, Jinseok Cha, Gabriel and Ioana Niculescu, Alicia Uzzle, Tony Cochran, Leon Cole, Romuald Davis, Michael Watson, and our adjunct student Pawel Ambrozevicz. Thanks to all the students that went before me Dipangkar Dutta, Derek Van Westrum, John Arrington, Chris Armstrong, Chris Bochna, Bart Terburg, and David Meekins. A special thanks goes out to the the kaon '*krew*' Doug Koltenuk, Richard Morning, Gabriel Niculescu, Jinseok Cha, Joreg Reinhold, and Paul Gueye for everything. Thanks to Dr. Warren Buck for starting the journey. Thank you to Dr. Donald Lyons for all his encouragement along the journey. I would like to thank my dissertation committee, Dr. Liguang Tang, Dr. Keith Baker, Dr. Rolf Ent, and Dr. Dave Mack for all their hard work in putting this collection of thoughts in a systematic order.

Thank you to each and everyone that influenced this work in any way.

TABLE OF CONTENTS

LIST OF TABLES

TABLE Page

LIST OF FIGURES

CHAPTER 1

INTRODUCTION

Nuclear physics and high energy physics overlap in the region of intermediate energy, where the interaction between nucleons inside the nucleus can be studied. Strange physics permits a new degree of freedom to be introduced into the nuclear system. This new degree of freedom permits these *strange* baryons to occupy energy levels which are inaccessible by protons or neutrons. Kaon electroproduction on nuclear targets leaves a residual hyperon and recoiling nucleus. A hyperon is a baryon with strangeness; it contains an s-quark. Hyperons were first observed in 1952 by Danysz and Pniewki as hyperfragments.[1] The lightest of the strange baryons, Λ hyperon has a mass of 1115.6 MeV/c^2 with strangeness S=-1 and isospin I=0. It occupies the same SU(3) octet representation of spin-parity $\frac{1}{2}^+$ as the neutron and proton (figure 1.1). The Λ is 177 Mev/c^2 heavier than the proton, with a free lifetime of 260 ps. Its quark constituents are up, down and strange ($u\ d\ s$).

A hypernucleus is a many-body system composed of conventional nucleons and one or more of these hyperons bound to the nuclear core. When incorporated into the nucleus the hyperon provides another degree of freedom, strangeness. This additional degree of freedom allows the hyperon to populate energy levels

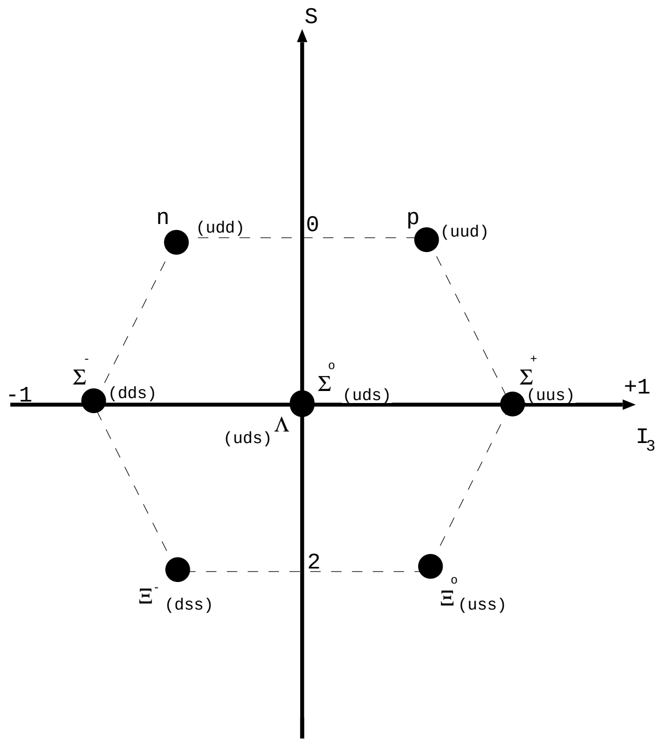

Figure 1.1: Isospin and strangeness of the baryon octet of the spin-parity $\frac{1}{2}^+$ particles.

forbidden to protons and neutrons by the Pauli principle. The Pauli exclusion principle excludes two fermions, half integral spin particles, from occupying the same quantum state. The particle-stable hypernuclear system is a powerful tool for new many-body spectroscopy. From it we can learn about hyperon interactions and hypernuclear structure. The role of the Pauli exclusion principle for Λ can be explored, when a u quark is converted to a s quark inside the nucleus. Quasifree hyperon production also takes place in electro-kaon production. These higher energy hyperons allow the study of hyperon-nucleon (Y-N), kaon-nucleon (K-N), and kaon-hyperon (K-Y) interactions.

1.1 Production Mechanisms

The majority of hypernuclei and hyperon studies were performed through associated strangeness production with the (π, K) reaction and hadronic strangeness exchange with the (K, π) reaction. With the development of high duty factor, high quality electron accelerators, hyperon studies have begun to include electromagnetic production with virtual photons (e, e$'$ K$^+$) and real photons (γ, K$^+$). The electromagnetic and hadronic production mechanisms are complementary to each other. The combination of these different production mechanisms provides a more complete study of the hyperons.

1.1.1 Strangeness/Associated Production

The earlier studies of hypernuclei used the (K,π) reaction with stopped kaon beams in the targets. Bubble chambers were used for these first low intensity K$^-$ beam in-flight studies. The advantages were the good, low-momentum energy resolution, and complete solid angle coverage of the decay products. The disadvantages were the low statistics and the range of hypernuclei which could be studied. [2]

With the availability of higher intensity kaon beams a more systematic study began [2]. In hadronic strangeness production the strange quark is transfered from the K$^+$ to the Λ. The (K$^+$, π^-) reaction has low momentum transfer and excites low total angular momentum states. This reaction tends to remove the neutron and replace it with a Λ in the same nuclear shell. The Λ is essentially recoilless at the magic momentum. This is the momentum at which the Λ remains at rest in the lab system. Figure 1.2 shows the spectra from various nuclear targets using the (K, π) reaction [2] .

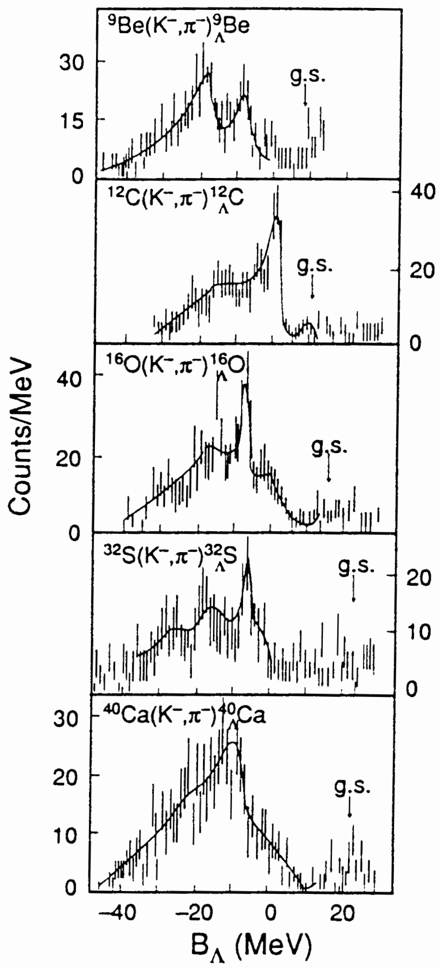

Figure 1.2: (K, π) reactions on various nuclear targets(^{9}Be,^{12}C, ^{16}O, ^{32}S, ^{40}Ca) from [2].

The study of associated production began at Brookhaven National Laboratory in 1983 [4]. The (π, K) reaction has a large momentum transfer and it also

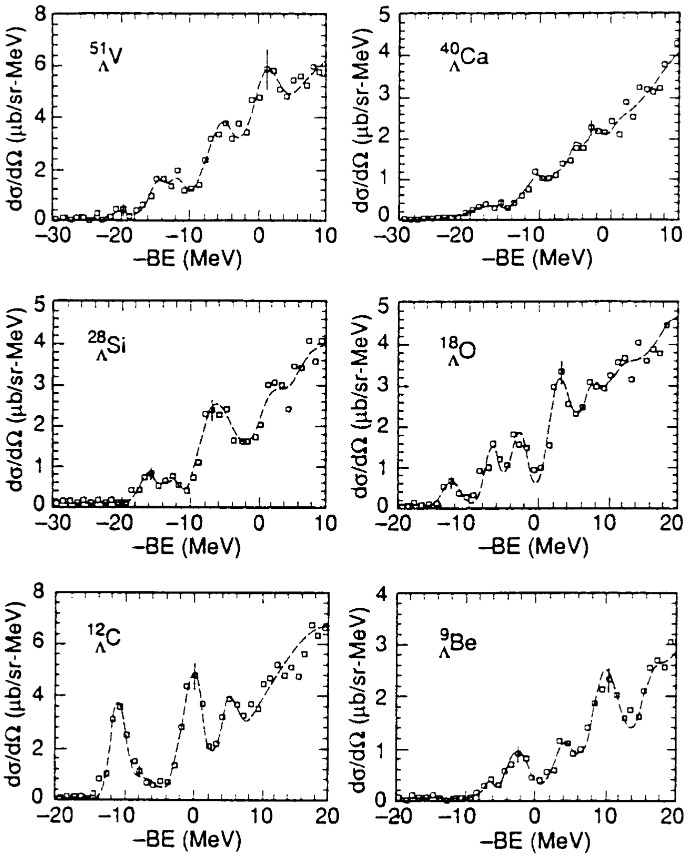

Figure 1.3: (π,K) reactions on light to medium nuclear targets (^{9}Be, ^{12}C, ^{18}O, ^{28}Si, ^{40}Ca, ^{51}V) from [2]. Hypernuclear spectra are plotted in terms of binding energy (MeV). The peaks below 0 MeV represent bound Λ states.

converts a neutron in the target nucleus to a Λ hyperon. The large momentum transfer of the (π,K) reaction, makes the quasifree process dominant in the highly excited region where a Λ is knocked out from a nucleus.[5] Figure 1.3 shows the (π, K) reactions on light and medium nuclear targets [2].

1.1.2 Electromagnetic Production

Electromagnetic production will be complementary to the reactions described previously. Electrons, as a nuclear probe, have some advantages over hadronic probes for studying the structure of the nucleus. The electron interaction via a virtual photon is well known and governed by quantum electrodynamics (QED). The electromagnetic interaction allows coupling to the charge ρ and the current distributions J of the nucleus. It is a weak interaction allowing the electron to probe the entire nucleus while only mildly disturbing the target. An electron beam is very 'clean' compared to a hadronic beam which may contain other unwanted particles in the beam. The disadvantages of electron scattering is that the cross sections are much smaller than hadronic cross sections. Also, the light weight electron will easily emit Bremsstrahlung radiation giving rise to a radiative tail.

Electro- and photo- production of hyperons are characterized by a large momentum transfer [6], hence reducing the Λ sticking probability (the probability of creating a hypernuclei) thus increasing the free Λs. Electromagnetic production of strange nuclear systems provides access to hypernuclear levels difficult or impossible to be reached by the pseudoscalar meson reaction [2]. The photon introduces spin into the system, exciting spin-flip states [7] as well as the non-spin-flip states, and additionally both natural and unnatural parity states are excited [6]. The (e, e$'$ K$^+$) reaction cross section is about a hundred times smaller than the corresponding hadronic productions using (π, K) reaction but it can be compensated by the availability of high intensity and high duty factor electron beams [8]. Figure 1.4 shows the first measurement of $^{12}C(\gamma,\ K)$ [3] where one can see the bound and quasifree regions. These data are compared to the results from the experiment described in a later section.

In quasifree scattering the incident particle transfers sufficient momentum to the target nucleus that the interaction is considered to take place with a single nucleon. Quasifree reactions are the tools used to study the propagation of nucleons in the nuclear medium. [9] A strongly interacting particle is unable to scatter from every nucleon within a complex nucleus.[10] The electron weakly interacts with the nucleus allowing the electron to penetrate the nuclear interior. The photon is able to illuminate the entire nuclear volume. This allows the study of the behavior of nucleons and a hyperon in the nuclear interior with less distortion. The behavior of the quasifree process must be taken into account when discussing the absolute cross section of specific hypernuclear states.[11]

1.2 Motivation

Electroproduction using virtual photons offers a new opportunity to explore the production of hyperons. It is this new opportunity which motivated this experiment to study the quasifree production mechanism. The quasifree production of Λ, Σ^0 and Σ^- were studied on the carbon, aluminum nuclear targets. The A-dependence of the effective nucleon number of various nuclear targets (^{2}H, ^{12}C,

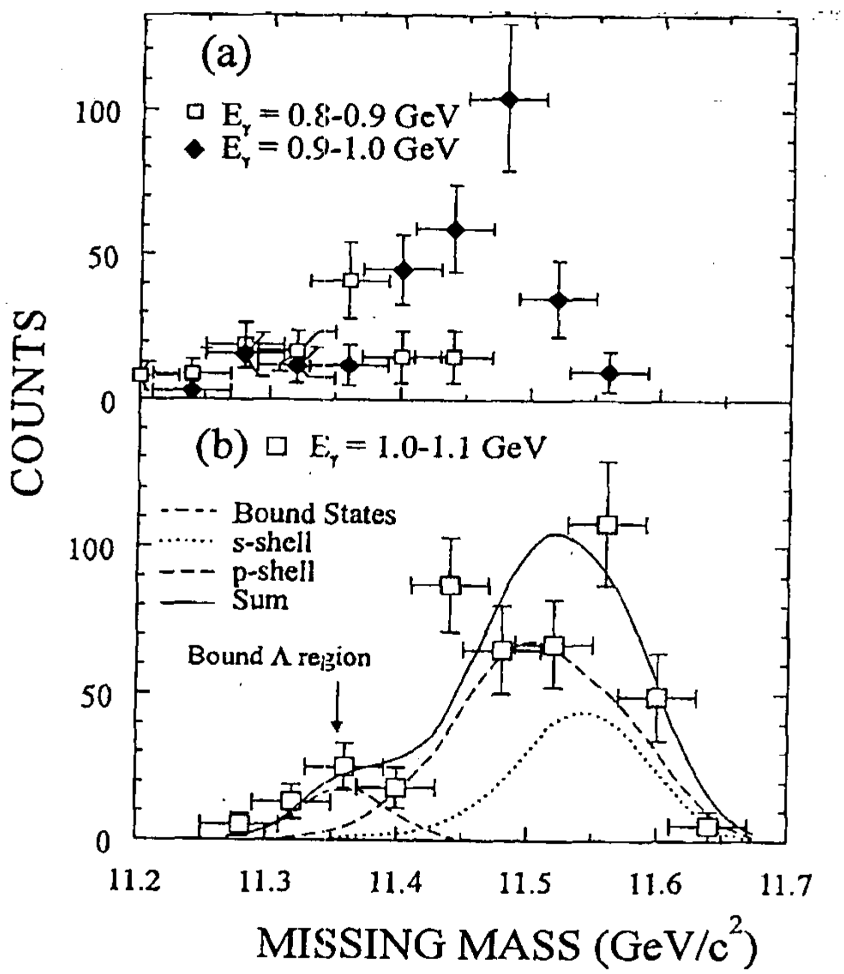

Figure 1.4: Missing mass distribution of ^{12}C(γ,K$^+$) from [3]. The strength around M$_x \approx 11.5$ Gev/c^2 is the quasifree distribution. The arrow indicates the $^{12}_{\Lambda}$B ground state.

^{27}Al) were studied using the elementary process p(e,e$'$ K$^+$)Λ(Σ^o) from hydrogen as the reference. The overall sigma production was studied to gain an understanding of the Σ^0 to Σ^- ratio in the heavier nuclear targets. The experimental setup was not optimized for the production of bound hyperons. The standard Hall C spectrometers are not capable of reaching the extreme forward angles to maximize the cross section for hypernuclei production. Therefore the motivation for this experiment was not to create hypernuclei but to study the feasibility of performing hypernuclear spectroscopy with high resolution at the Jefferson Lab facility Hall C end station.

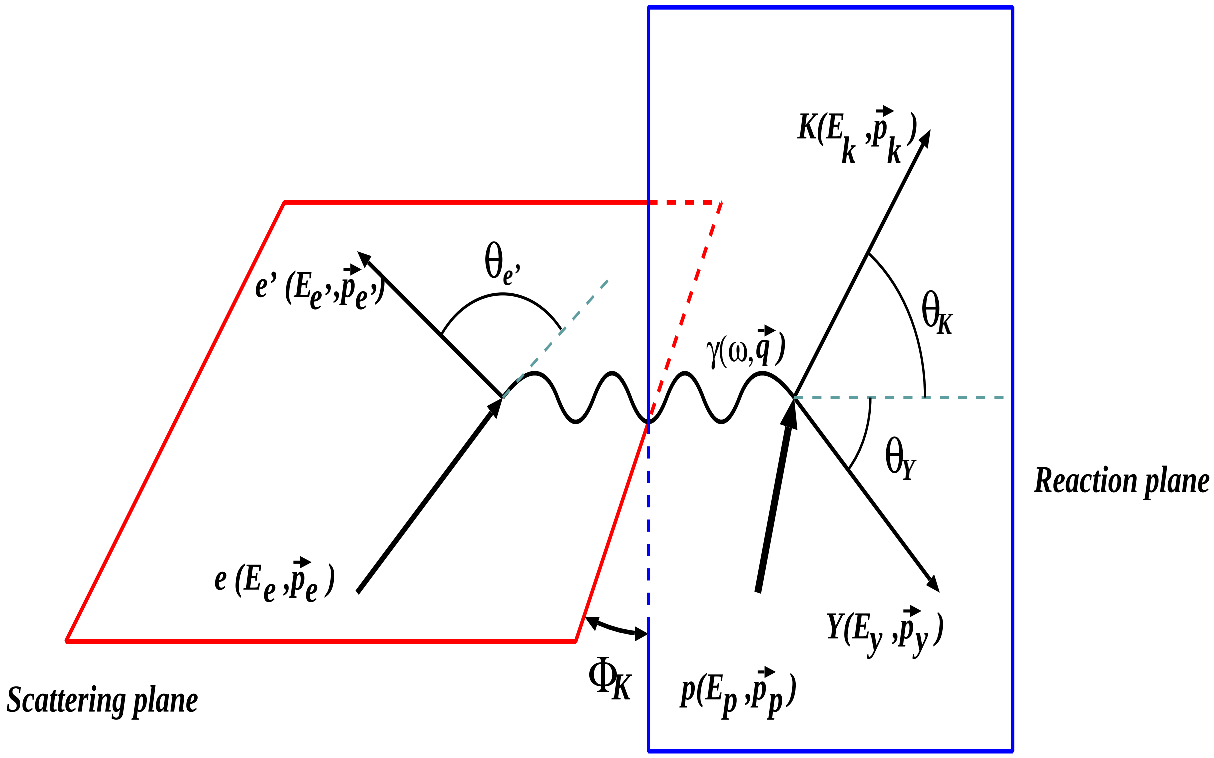

Figure 1.5: Reaction plane for (e,e'K$^+$)Y reaction.

1.3 Theory

The elementary reaction (e,e$'$ K$^+$) is depicted in Figure 1.5. The incident electron (e) interacts with the target proton via a virtual photon (γ). The scattered electron (e') travels at the angle $\theta_{e'}$ with respect to the direction of the incident beam, and is detected in the High Momentum Spectrometer (HMS). The incident and scattered electrons define the scattering plane. The virtual photon carries the momentum and energy transfered from the electron to the nucleon target. A kaon (K$^+$) and a hyperon (Y) are formed from the virtual photon and nucleon interaction. The kaon is emitted at the angle $\theta_{\gamma K}$ with respect to the virtual photon direction and is detected in the Short Orbit Spectrometer (SOS). The kaon and hyperon define the reaction plane. The out-of-plane angle, Φ_K is the angle between the scattering and reaction plane.

The elementary process of the kaon electroproduction for the A(e, e′ K$^+$)(A-1)Y reaction is depicted by the Feynman diagrams in Figure 1.6. In the elementary reaction, an electron interacts with a single proton

$$e + p \rightarrow e' + K^+ + \Lambda^o, \Sigma^o \tag{1.1}$$

or a single neutron

$$e + n \rightarrow e' + K^+ + \Sigma^- \tag{1.2}$$

The corresponding diagrams are shown in Figures 1.6b-d which consist of Born terms in the s, t and u channels where the photon couples to the nucleon, kaon, and hyperon, respectively. The incident and scattered electrons are omitted from the diagrams and only the virtual photon interaction is shown.

The cross section can be expressed in terms of the five-fold differential cross section $\frac{d^5\sigma}{dE_{e'}d\Omega_{e'}d\Omega_K}$. This cross section is reduced to a center-of-mass cross section by

$$\frac{d^5\sigma}{dE_{e'}d\Omega_{e'}d\Omega_K} = \Gamma J \frac{d^2\sigma}{d\Omega_K} \tag{1.3}$$

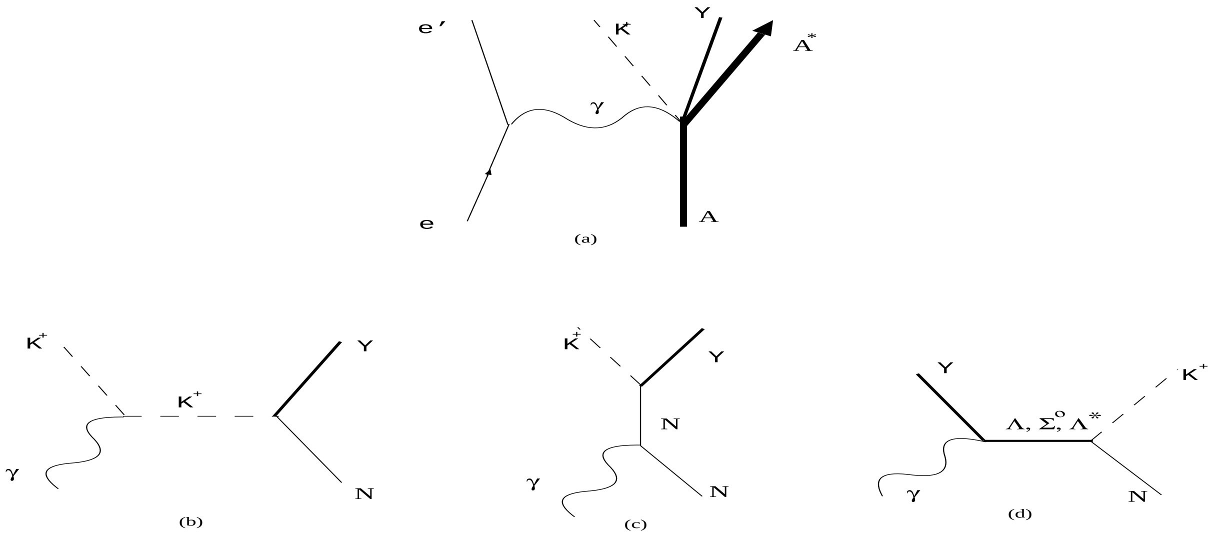

Figure 1.6: (a)Feynman diagrams for the elementary process in the A(e,e′K$^+$)A$^*Y$ reaction. (b)-(d) diagrams for the elementary reaction of the (b)t, (c)s, and (d)u channel exchanges.

where Γ is the virtual photon flux factor,

$$\Gamma = \frac{\alpha}{2\pi^2}\frac{E'}{E}\frac{W^2 - M}{2MQ^2}\frac{1}{1-\epsilon} \quad , \tag{1.4}$$

and J is the Jacobian. E is the initial electron energy, E′ is the scattered electron energy, M is the mass of the target nucleon, W is the invariant mass of the virtual photon plus proton system, Q^2 is the square of the four-momentum transfer carried by the virtual photon, and ϵ is the transverse linear polarization of the virtual photon

$$\epsilon \;=\; \frac{1}{1 + 2\frac{|q|}{Q^2}\tan\left(\frac{\theta_e}{2}\right)} \quad . \tag{1.5}$$

The center of mass cross section can be decomposed further as [12]

$$\frac{d^2\sigma}{d\Omega_K} = \left(\frac{d^2\sigma_T}{d\Omega_{cm}}\right) + \epsilon_L\left(\frac{d^2\sigma_L}{d\Omega_{cm}}\right) + \sqrt{2\epsilon(\epsilon+1)}\frac{d^2\sigma_{TT}}{d\Omega_{cm}}\cos\phi + \epsilon\frac{d^2\sigma_{LT}}{d\Omega_{cm}}\cos 2\phi \quad (1.6)$$

where $\frac{d^2\sigma_T}{d\Omega_{cm}}$ is the cross section due to transversely polarized virtual photons, $\frac{d^2\sigma_L}{d\Omega_{cm}}$ is the cross section due to the longitudinally polarized photons, $\frac{d^2\sigma_{TT}}{d\Omega_{cm}}$ is the interference between the two different states of transversely polarized virtual photons, and $\frac{d^2\sigma_{LT}}{d\Omega_{cm}}$ is the interference between the transverse and longitudinal components. The missing mass is equal to the sum of the masses of the undetected particles in the final state. The differential cross section of quasifree production can be written as

$$\left(\frac{d\sigma}{d\Omega}\right)_{nucl} = \int\left(\frac{d^2\sigma}{d\Omega dp}\right)_{nucl} dp \quad (1.7)$$

$$\left(\frac{d\sigma}{d\Omega}\right)_{nucl} = \int\left(\frac{d\sigma}{d\Omega}\right)_{elem} \zeta R(q,\omega)\frac{d\omega}{dp}dp \quad (1.8)$$

$$\left(\frac{d\sigma}{d\Omega}\right)_{nucl} = \left(\frac{d\sigma}{d\Omega}\right)_{elem} Z_{eff} \quad (1.9)$$

$$Z_{eff} = \frac{\left(\frac{d\sigma}{d\Omega}\right)_{nucl}}{\left(\frac{d\sigma}{d\Omega}\right)_{elem}} \quad (1.10)$$

where $\left(\frac{d\sigma}{d\Omega}\right)_{nucl}$ and $\left(\frac{d\sigma}{d\Omega}\right)_{elem}$ are the differential cross sections for the nuclear and proton target, respectively [3]. R(q,ω) is the nuclear response function as a function of momentum transfer q and energy transfer ω. ζ is defined in terms of masses of the Λ and proton

$$\zeta^2 = \frac{(M_\Lambda - M_p)}{2M_p} \tag{1.11}$$

Z_{eff} equation(1.10), is the effective number of protons which take part in the production of the quasifree Λ. One of the goals of this experiment was to determine the effective proton number of various nuclear targets for quasifree Λ production.

1.4 Kinematics

E93-18 is a coincidence measurement of the H(e,e$'$K$^+$)Y reaction. E91-16 was also a coincidence measurement but with a deuterium target. Prior to these experiments kaon electroproduction data were limited [13],[14],[15]. The first photoproduction experiment on a carbon target was performed in 1995 [3].

The carbon target was a 0.5 g/cm solid target and the kinematic settings are listed in Table 1.1. The carbon data were collected in two different periods, October and November 1996, which amounts to a total of 32 hours of beam time. The kinematic settings chosen were to allow both the study of quasifree and bound Λ regions in the same spectrometer settings. The forward angles of the e$'$ and K$^+$ spectrometers permits the feasibility study of hypernuclear spectroscopy while including the quasifree spectra.

The aluminum target, corresponding to the “dummy” cryogenic target, is made up of two aluminum foils 4 cm apart and 0.5215 g/cm thick each. The

	Q^2 (GeV/c)^2	$\theta_{\gamma K}$ (degrees)	θ_{HMS} (degrees)	θ_{SOS} (degrees)	P_{HMS} (GeV/c)	P_{SOS} (GeV/c)	I (μA)
I	0.394	0	15.42	15.53	1.684	1.268	35
II	0.353	0	14.30	15.60	1.750	1.200	20

Table 1.1: Carbon Kinematic Setup E_{beam}= 3.245 GeV.

E_{beam} GeV/c	Q^2 (GeV/c)^2	$\theta_{\gamma K}$	θ_{HMS} (degrees)	θ_{SOS} (degrees)	P_{HMS} (GeV/c)	P_{SOS} (GeV/c)
4.045	0.52	0	13.20	18.25	2.433	1.126
2.445	0.75	0	37.95	13.42	0.725	1.188
3.245	0.75	0	22.44	17.62	1.526	1.188
4.045	0.75	0	16.23	19.75	2.326	1.188
2.445	1.00	0	29.27	13.42	0.833	1.126
3.245	1.00	0	28.43	18.20	1.435	1.220
4.045	1.00	0	19.14	20.78	2.326	1.216
4.045	1.00	0	23.73	23.39	2.191	0.935
3.539	1.25	0	27.65	18.21	1.544	1.385
3.245	1.25	0	32.31	16.80	1.244	1.385
4.045	1.25	0	22.34	20.00	2.044	1.385
4.045	1.50	0	22.73	23.39	2.191	0.935
4.045	2.00	0	19.86	18.66	2.078	1.432
3.539	2.00	0	41.11	15.67	1.145	1.634
3.539	2.00	0	20.76	15.95	1.629	1.440
3.539	2.00	0	27.65	18.21	1.544	1.385
3.539	2.00	0	24.41	17.18	1.578	1.432

Table 1.2: Aluminum Kinematic Setup from Exp 93-18.

aluminum was also used to study the cryotarget cell wall background contribution to the hydrogen and deuterium cryogenic targets. The kinematics were optimized for these studies. The data were sufficient to study quasifree hyperon production on the heavier aluminum nucleus. Tables 1.2 and 1.3 show the kinematic settings for aluminum. Table 1.2 includes the kinematic settings for hydrogen from Exp 93-18 and Table 1.3 the kinematic settings for hydrogen and deuterium from Exp 91-16.

E_{beam} GeV/c	Q^2 $(GeV/c)^2$	$\theta_{\gamma K}$	θ_{HMS} (degrees)	θ_{SOS} (degrees)	P_{HMS} (GeV/c)	P_{SOS} (GeV/c)
2.445	0.376	1.5	24.60	13.42	0.847	1.15
3.245	0.376	1.5	15.42	15.483	1.593	1.240
3.245	0.376	11	15.42	25.00	1.593	1.240
2.445	0.50	1	27.25	15.48	0.918	0.929
3.245	0.50	0	17.19	17.67	1.723	1.077
3.245	0.50	4.33	17.19	21.97	1.723	1.077
3.245	0.50	8.78	17.19	26.45	1.723	1.077
3.245	0.50	13.3	17.19	31.00	1.723	0.929

Table 1.3: Aluminum Kinematic Setup from Exp 91-16.

CHAPTER 2

INSTRUMENTATION

The experiment took place at the Thomas Jefferson National Accelerator Facility (Jefferson Lab) in Newport News, Virginia. The electron beam provided by the intermediate-energy electron accelerator, Continuous Electron Beam Accelerator Facility (CEBAF) at Jefferson Lab is capable of probing both nucleon and quark structure in nuclei. The accelerator delivers an electron beam with continuous wave (CW) beam at 100% duty factor, high intensity, and high energy resolution ($\approx 10^{-4}$). The beam can be delivered to three experimental halls, Hall A, B and C, simultaneously. The experiment presented here was carried out in Hall C using its two standard spectrometers, the High Momentum Spectrometer (HMS) and the Short Orbit Spectrometer (SOS).

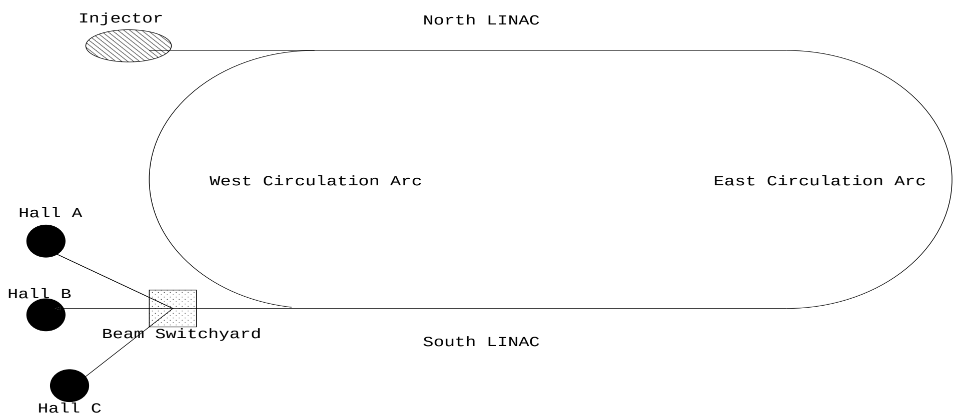

Figure 2.1: The Continuous Electron Beam Accelerator at Jefferson Lab.

2.1 Accelerator

One complete cycle of the accelerator at CEBAF has a track length of a 7/8 mile, figure 2.1. The electron beam is accelerated by two linear accelerators (North and South LINACs) and circulated by the arc sections between the two LINACs using a series of bending magnets . From the injector, which uses a thermionic electron gun as the electron source, the electron beam is extracted with an energy of 45 MeV under standard setup. The LINAC is formed by a series of super-conducting radio frequency cavities (RF), while the circulation arc contains a series of bending and focusing magnets. A single pass (one complete circle) will increase the electron energy by 800 MeV with a standard tune. The arc consists of five layers of magnets. Each layer is used to circulate the beam with a specific energy which increments 800 MeV per pass. An electron that goes through five complete passes will have a maximum beam energy of 4.045 GeV. The maximum current the machine can reach is 200 μA. The beam structure consists of 1.67 ps bunches at a frequency of 1497 MHz of 0.668 ns bunch separation. Each hall receives beam with a fraction of the total frequency with 2 ns bunch separation. The beam is separated at the beam switch yard and delivered to the three independent halls. The dispersion of the beam is $\Delta E/E \leq 10^{-4}$ with a typical emittance of 2 x 10^{-9} mrad. During the period of the presented experiment, Hall C was the only experimental hall receiving beam.

2.2 Hall C arc and beamline

The beam is extracted at the beam switch yard and sent to Hall C through the arc. Various beamline instrumentation in Hall C are used to better determine the beam energy and position. Figure 2.2 shows the instrumentation in the arc and hall.

The beam profile is monitored using a series of harps and superharps. The harps and superharps do this by passing three thin sets of tungsten wires across the beam. Two wires measure the position and spread in the horizontal direction (x) and one the vertical direction (y). An Analog-to-Digital Converter (ADC) measures the induced signal size and a position encoder measures the position of the ladder as the wires pass through the beam. The distribution of signal size as a function of position provides a measurement of the beam size. The superharps are similar to harps but are more accurate due to the surveyable absolute position. The spot size of the beam determined by the harps was typically ≤ 200 μm. They provide absolute position measurements, when these devices are in use, data can not be taken because they disrupt the beam.

Beam Position Monitor (BPM) measures the beam center position in order to determine the trajectory and can be used continuously without disturbing the beam. A BPM is a resonant cavity which consist of four antennae located 45° with the horizontal and vertical axes. As the beam passes through the cavity the antenna picks up a harmonic frequency from the beam which is proportional to the distance from the beam center to the antennas. The BPMs are calibrated using the superharps, then used online continuously through data taking.

There are two types of current monitors used to measure the current transported into Hall C. The unser which is a parametric current transformer, is used to determine the absolute current. It is used to calibrate the beam current monitor (BCM) made of microwave cavity. Three sets of BCMs are used to determine the integrated beam current which is a measure of the number of incident electrons.

The high intensity beam was rastered with a high frequency to prevent damage to the targets. The raster was done by using two bending magnets with very small inductance, one for the (x) direction and another for the (y) direction to create a combined two dimensional motion. Such motion is a sinusoidal oscillation both in the vertical and horizontal planes (Lissajous pattern). The raster size was 1 mm $\times$ 1 mm. Due to the sinusoidal design of the rastering pattern the beam spent more time at the edges of square rastered pattern than it does at the center as seen in figure 2.3.

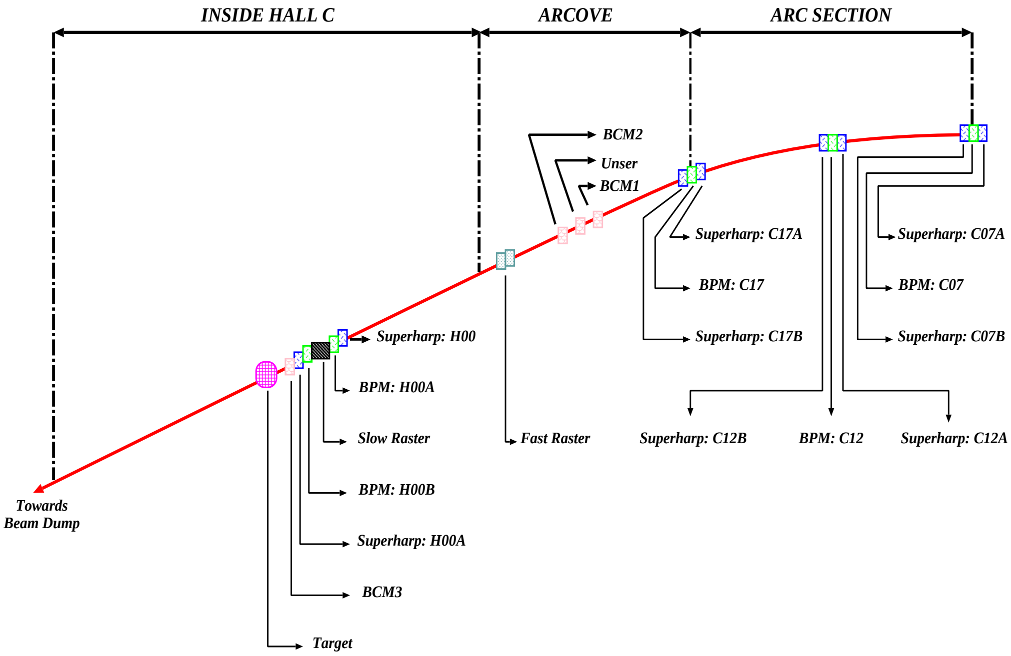

Figure 2.2: Hall C beam line and arc

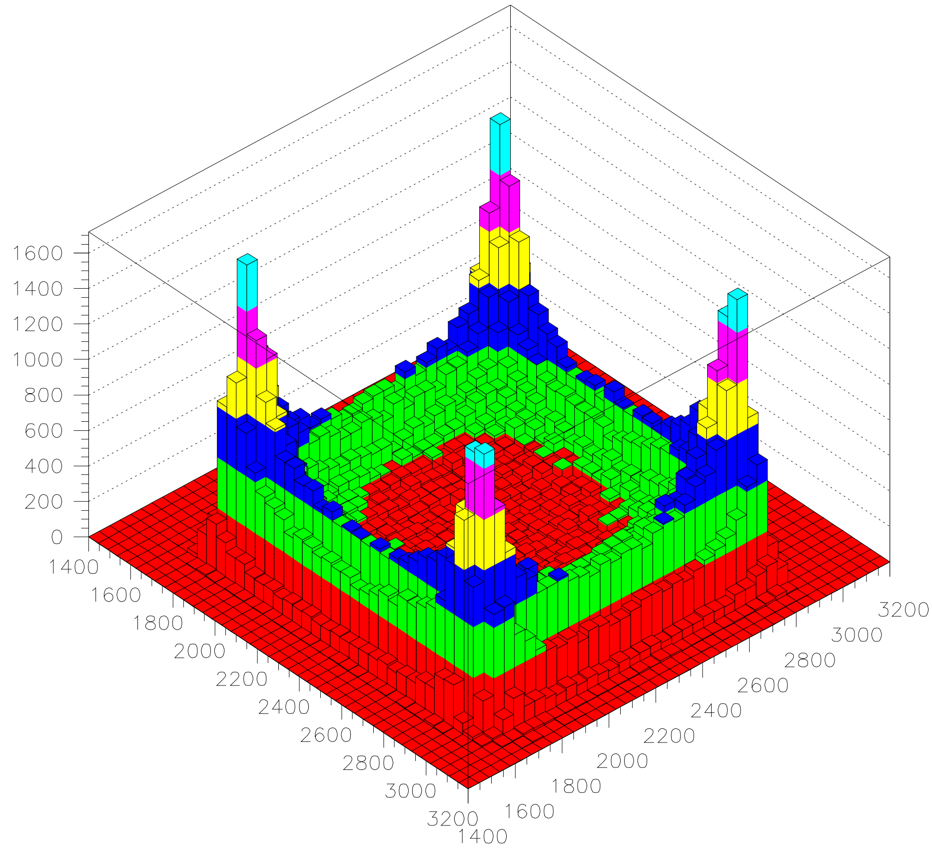

Figure 2.3: Beam profile with the fast raster in use.

2.3 Target

The target scattering chamber is a large cylindrical aluminum chamber 136.5 cm high, 123.2 cm diameter and 6.35 cm thick. The chamber was connected directly to the beamline, under high vacuum. The beam exit window is made of titanium foil approximately 70 mg/cm^2 thick.. The beam pipe towards the beam dump is filled with helium gas under atmospheric pressure. The exit windows of the two spectrometers, HMS and SOS (see descriptions in a later section), are made of aluminum foil.

The targets for the experiment include both cryogenic, hydrogen and deuterium, and solid targets, carbon and aluminum. The cryogenic and solid targets were mounted on separate target ladders. Both target ladders could be rotated 90° remotely to insert the other ladder.

The cryotarget system contains three loops each loop consisting of a 15 cm cell and a 4 cm cell. Figure 2.4 shows the three cryotarget loops and the two empty targets slots, one 15cm and one 4cm. Within each loop there is a circulation fan, heat exchangers, and high and low power heaters. Each cell is made of a 0.0178 cm thick aluminum cylinder. The temperature and pressure of the targets were monitored continuously during the experiment. The nominal temperature and pressure for hydrogen is 19 K and 24 psi, and deuterium's nominal temperature and pressure is 22 K and 20 psi. Each cell loop thus provides one type of liquid target with two different thickness. Only 4 cm liquid targets were used in this

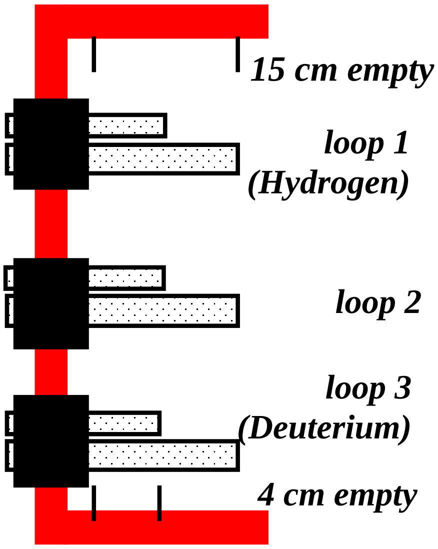

Figure 2.4: Hall C crytotarget ladder.

experiment. The aluminum target is actually the front and back walls on the 4 cm empty cell. It was used to extract the contribution of the cell walls to the data from the cryogenic target cells.

The solid target ladder is capable of holding five targets, three thin targets and two thick. A 0.5 g/cm^2 carbon target was used for this experiment. The ladder is cooled by water on all four sides that circulated through a copper tube attached to the ladder. The active target area is 2.0 cm $\times$ 3.3 cm; this allows plenty of clearance ($\approx$5 mm) from the ladder's frame. Figure 2.5 shows the solid target ladder and the five target positions.

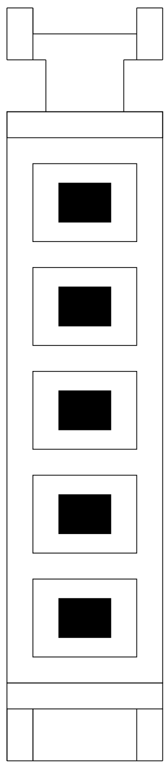

Figure 2.5: Hall C solid target ladder. The 0.5 g/cm^2 carbon target was located in the fourth target space from the top.

2.4 High Momentum Spectrometer

The HMS consists of four superconducting magnets, three quadrupoles (Q1,$\overline{Q}$2,Q3) and one dipole(D), with a momentum resolution of 1.2×10^{-3} (FWHM). Q1 and Q3 focus the particles in the dispersive direction while Q2 focuses in the transverse direction. The dipole has a central bending angle of 25°. The spectrometer has a momentum acceptance of 20%. The magnets are cooled with 4K liquid helium. The spectrometer was operated in the standard point-to-point tune, which provide a large momentum and solid angle acceptances to match the SOS momentum bite. The HMS was used to detect electrons in a background of pions. Table 2.1 list the HMS and SOS main parameters.

2.5 Short Orbit Spectrometer

The SOS consists of one quadrupole (Q) and two oppositely bending dipoles (D$\overline{D}$), with a momentum resolution of better than 10^{-3}. The quadrupole was designed to horizontally focus the particles. The first dipole bends the particles upward 33° and the second dipole bends the particles downward 15° for an over all bending of 18°. The dipoles share a return yoke. The fringe field of the dipole was designed to provides focusing in the dispersive direction. All three magnets are cooled with pressurized water. The spectrometer has a large momentum acceptance of 40% and a short optical length, 10 m to the last hodoscope. The spectrometer was calibrated and used a point-to-point focus tune for this experi-

Parameter	SOS	HMS
Maximum central momentum	1.75 GeV/c	7.3 GeV
Momentum acceptance	±20%	±10%
Momentum resolution	0.1%	0.12 %
Solid angle acceptances	10.7 msr	8.1 msr
Angular acceptance (scattering plane)	±70 msr	±32 msr
Angular acceptance (out of plane)	±40 msr	±85 msr
Scattering angle reconstruction accuracy	4.0 mr	0.5 mr
Out of plan angle reconstruction accuracy	0.5 mr	1.0 mr
Vertex reconstruction accuracy	1-2 mm	2-3 mm

Table 2.1: HMS and SOS spectrometer parameters.

ment [16]. The short orbit length is ideal for detecting the short-lived K^+ meson, which has a lifetime of 1.2×10^{-8}s. Table 2.1 list the SOS and HMS main parameters.

2.6 Detector Packages

The detector packages for both the HMS, figure 2.6, and the SOS, figure 2.7, are similar. Both packages contain two drift chambers for tracking, four hodoscope planes for time-of-flight (TOF) measurement, a gas Čerenkov detector for π/e separation, and a shower counter array for e^-/e^+ detection. The SOS has two additional Čerenkov detectors, the aerogel and lucite Čerenkov, to reduce the background trigger rate: the aerogel was used to suppress π^+ rate, while the lucite was used to suppress protons and heavier particles rates.

The drift chambers are located immediately following the exit vacuum windows in both detector huts to minimize multiple scattering effects when trying to

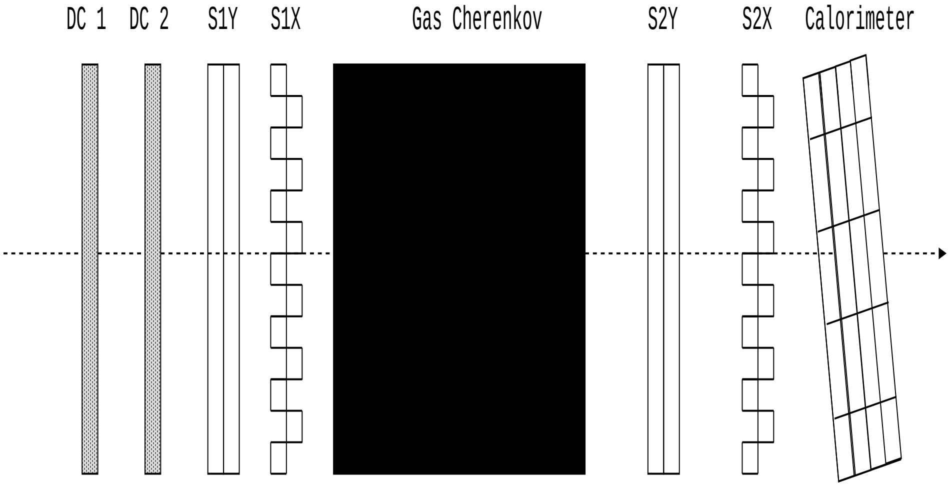

Figure 2.6: HMS detector hut

define the particles track. A 50:50 argon-ethane gas mixture was used in both HMS and SOS drift chambers.

Each of the HMS chambers have six wire planes, two measuring dispersive direction (x, x'), two measuring the non-dispersive direction (y, y') and two stereo planes rotated by $\pm15°$ (u, v) relative to the x planes . The HMS has an active area of approximately $107{\times}52\text{cm}^2$

The SOS chambers also have six wire planes per chamber. The (x, x') measured the dispersive direction. The (u,u') planes were rotated 60° clockwise from the x plane. The (v v') planes were rotated 60° counterclockwise. The active area of the SOS is approximately $63{\times}40$ cm^2.

The scintillator hodoscopes were used to form the primary trigger for charge particle detection. They also provided time-of-flight and dE/dx information. Both detector stacks contain four scintillator planes, two planes measure the x-direction and two the y-direction. Each plane has several segments, each of which are made of 1 cm thick light-tight plastic scintillator. The scintillator overlaps its immediate neighbor by 5 mm in order to maximize the charged particle detection efficiency. The SOS has 9 scintillators in both y planes and 9 scintillators in the front x plane and 16 scintillators in the back x plane. The HMS has a larger active area thus it has 16 scintillators in the x planes and 10 scintillators in the y planes.

Čerenkov detectors detect the Čerenkov radiation emitted by particles when they enter a medium at a velocity greater than the speed of light in that medium. The gas Čerenkov in the HMS uses CO_2 at atmospheric pressure and room temperature. This allows the detector to be sensitive to the detection of electrons. The silica aerogel Čerenkov in the SOS has an index of refraction of $n = 1.034$ giving a threshold $\beta \approx 0.967$ and thus allows the separation of the particles which travel above threshold. Therefore, the purpose of the aerogel is to detect and separate pions from the heavier hadrons, such as kaons and protons. A detailed description of the aerogel Čerenkov can be found in [17]. The index of refraction of the lucite detector is 1.49, which allows almost all the charged particles to radiate light. However, due to low velocity the photons from protons and heavier particle are emitted with smaller angles than the total internal reflection angle. Using the principle of total internal reflection protons are separated from the K^+or π^+. The lucite Čerenkov detector is discussed in more detail later.

The lead glass calorimeters of both the HMS and SOS are located at the back

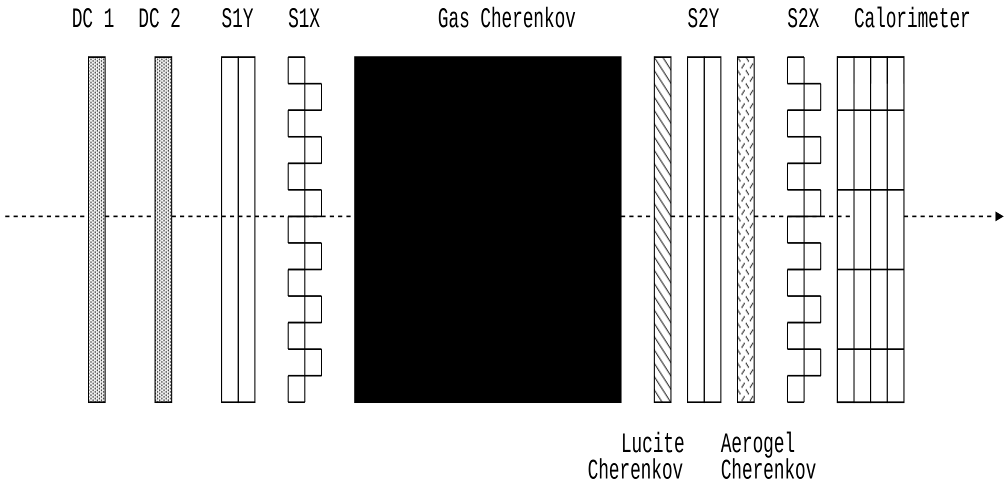

Figure 2.7: SOS detector package with the additional Čerenkov

of the detector stacks and are for e/π separation. They consist of four stacks of lead glass blocks. The electron radiate bremsstrahlung photons while traveling through the calorimeter that in turn create e^+ e^-pairs, hence creating an electromagnetic shower. The separation of e/π comes from the fact that electrons will deposit almost all of their energy into the lead glass whereas the pions deposit only a small fraction of theirs. Neither the SOS lead glass nor the gas Čerenkov were used during the experiment. Positron (e^+) were not a background problem for particle identification due to the kinematic settings. Any e^+ in the SOS were removed with the aerogel Čerenkov and additional detectors were not needed.

2.7 Lucite Čerenkov

2.7.1 Introduction

The lucite Čerenkov detector was tested during the running of Experiment 91-16 and was used in the online trigger during the hypernuclear spectroscopy feasibility test. The lucite Čerenkov is a threshold detector designed to discriminate between p^+ and K^+ particles [18]. Čerenkov radiation occurs when a particle enters a transparent medium where the index of refraction is greater than one. When the velocity of the particle is greater than the velocity of light inside the medium, the particle will radiate Čerenkov light. The radiation forms a cone surface centered along the particle's momentum. The angle of the radiation cone, θ_i, depends on the index of refraction of the medium *(n)* and the velocity of the particle (β) defined in equation (2.1). The radiation angle is given by equation (2.2).

$$\beta = (\frac{v}{c}) \tag{2.1}$$

$$\theta_i = \cos^{-1}(\frac{1}{n\beta}) \tag{2.2}$$

The $\beta_{threshold}$ is the relative velocity of the particle below which no Čerenkov radiation is emitted [19]. $\beta_{threshold}$ is given by equation (2.3). The index of refraction for ultra-violet transmitting lucite is 1.49. Therefore any particle with a $\beta > 0.672$

will radiate Čerenkov light.

$$\beta_{threshold} = \frac{1}{n} \tag{2.3}$$

The central momentum setting of the SOS during the experiment was 1.2 GeV/c. The protons have a mean $\beta = 0.830$ and will radiate Čerenkov light. Therefore a threshold of 0.672 is too low to discriminate between protons and kaons.

However the inclusion of the principle of total internal reflection (TIR), raises the threshold of detected radiation to $\beta = 0.905$, as seen by equation (2.4). When the incident radiation angle θ_i is greater than the critical angle θ_{crit}, given in equation (2.5), the light is internally reflected inside the material and detected by both phototubes attached at both ends of the radiator,as shown in figure 2.8. [20] When θ_i is less than θ_{crit} , figure 2.9, the light will be transmitted out of the material. By requiring TIR, the Čerenkov detector will be able to discriminate between protons and kaons.

$$\beta_{(TIR\,threshold)} = \frac{1}{\sqrt{n^2 - n_o^2}} \tag{2.4}$$

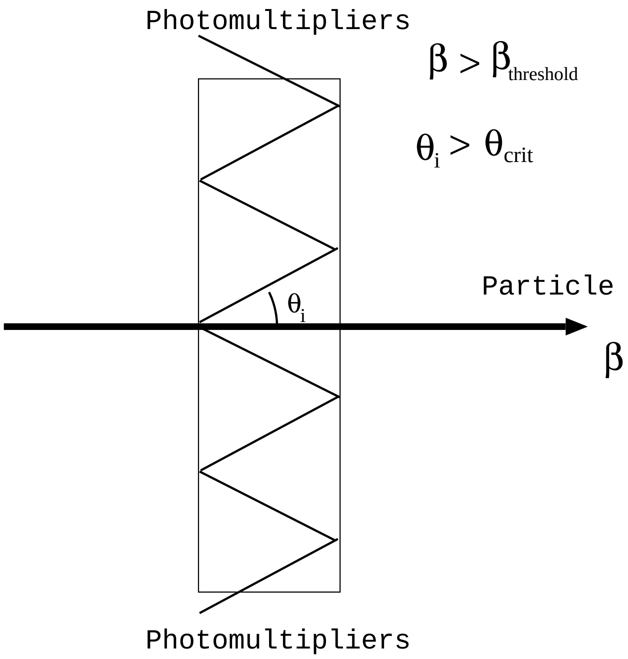

Figure 2.8: Particle with an incident angle greater than the total internal reflection angle of the material.

$$\theta_{crit} = \sin^{-1}\frac{n_o}{n} \tag{2.5}$$

One of the advantages of using a solid medium instead of a gas or liquids as a medium for the radiator can be seen in equation (2.6). N, the number of photoelectrons generated, is equal to the product of A,the characteristic number of light collection and quantum efficiency of the photomultiplier cathode, L, the thickness or length of the radiator and θ, the Čerenkov radiation angle. By using a solid material such as lucite with a high index of refraction, n=1.49, a large radiation angle θ is generated and therefore a large signal N. A gas medium can only provide

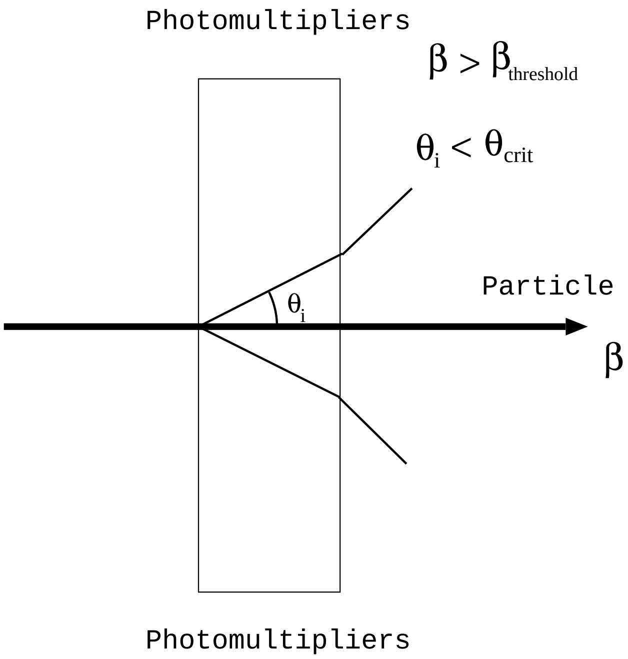

Figure 2.9: Particle with an incident angle less than the total internal reflection angle of the material.

a refractive index from $1.0 \leq n \leq 1.13$ below critical points and $1.13 \leq n \leq 1.35$ above their critical points. [21] The gas medium compared to the solid medium will require a longer radiator, L, to yield the same number of photoelectrons, N. Larger signal from the solid lucite medium permits a slimmer detector volume. The space constraint in the SOS detector hut requires a detector which would not take up a lot of space as figure 2.7 shows.

$$N = AL\sin^2\theta \tag{2.6}$$

Čerenkov radiation has a continuous spectrum, with a stronger intensity in the short wavelength, ultra-violet region. [21] The scattering and absorption length of the material are both dependent on the wavelength. Equation (2.7) shows that Rayleigh-scattering dominates in the short wavelength region. The scattering length is much smaller than the absorption length. For a detector with a long transmission length ($\geq$10cm) most of the light is scattered. In a TIR detector the radiation angle changes and the light is transmitted out of the detector and absorbed. Therefore, it is important to use uvt (ultra-violet transmitting) lucite to minimize the light lose due to absorption. Figure 2.10 shows the transmission curve for the uvt lucite used for the lucite Čerenkov.

$$I \approx \frac{1}{\lambda^4} \tag{2.7}$$

2.7.2 Detector

The lucite detector was designed and built jointly by the Hampton and Temple University groups. It consists of eight individual uvt lucite bars wrapped in black Teflon foil as absorber, see figure 2.11. Each bar has two 15 cm long light guides at each end tapered to a 6 cm width to fit the 3 inch Phillip photomultiplier tubes on each end. The photomultipliers were housed in polyvinyl chloride pipes for stability. The dimensions of the bars are 40$\times$13.7$\times$2.5 cm. The detector was mounted on a metal frame in the SOS detector hut between the gas Čerenkov and

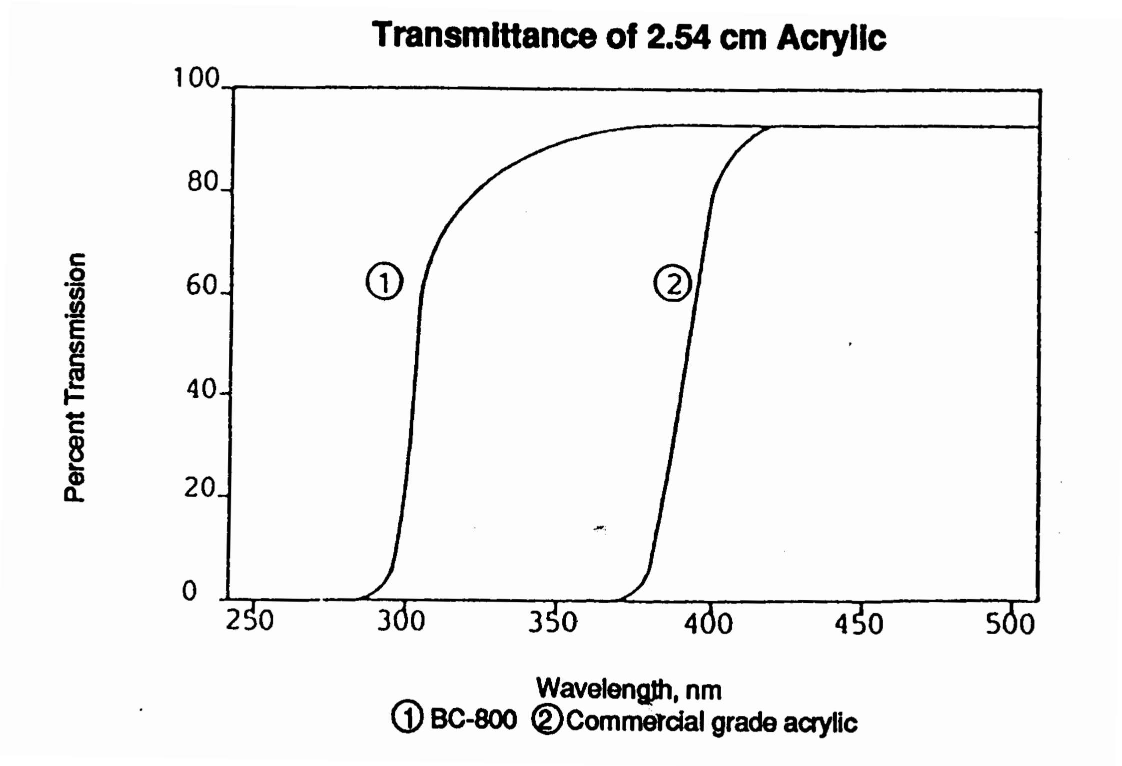

Figure 2.10: Transmission versus wavelength of the uvt lucite, curve 1. Curve 2 is the commercial grade acrylic.

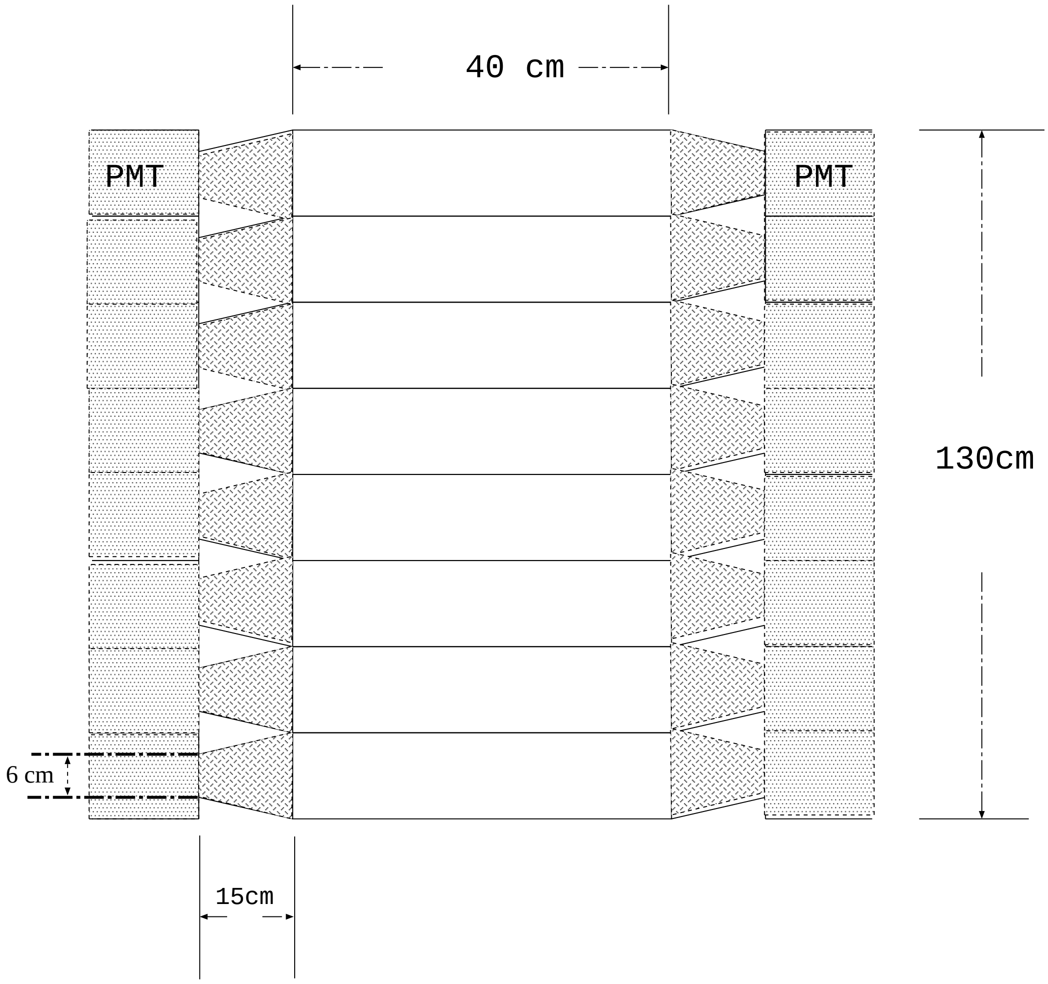

Figure 2.11: Diagram of the 8 lucite detector bars. Each with two photomultipler tubes.

the S2Y hodoscope. The frame for the detector was attached to the S2Y hodoscope frame. This can be seen in the SOS detector hut figure 2.7. The lucite bars are numbered 1 thru 8 from the top to bottom with the positive y direction, looking downstream, defined as the plus tubes and the negative y direction defined as the minus tubes. The detector was designed to discriminate protons from kaons at a threshold β=0.90.

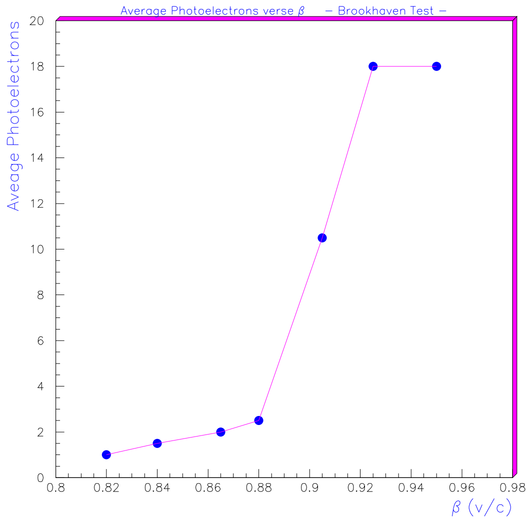

Figure 2.12: Average Number of Photoelectrons test at Brookhaven National Laboratory using a K^+ beam.

During the design and development phase, a prototype detector was tested at Brookhaven National Laboratory using the Alternating Gradient Synchrotron (AGS) secondary K^+ beam to determine the average number of photoelectrons. Figure 2.12 shows the results of this test which served as a base for the final detector design. The average number of photoelectrons for β =0.91 is 10 photoelectrons and for β =0.88 it is 2 photoelectrons. This minimum amount of output is due to large incident angle which can accidentally cause the light from slow proton transmitting to one side of the bar. This allows the discrimination between the proton at β =0.88 and the kaon at β =0.91 when an electronic threshold is set to accept events greater than 3 photoelectrons.

2.7.3 Electronics

The lucite detector system consists of 8 lucite bars with a total of 16 photomultipler tubes (PMT). Each signal from the PMT was amplified by a factor of ten and gain matched by adjusting the high voltage. The amplification of the signals was necessary to insure that one photoelectron signal could be accepted as a real signal and not as noise. This amplified signal was split, $\frac{1}{3}$ of the signal goes to an ADC. The other $\frac{2}{3}$ of the signal from all 16 PMT are sent to a summing module. The signal from each PMT is summed and then sent to a discrimintor. If the summed signal from the lucite Čerenkov was above 3 photoelectrons then the event was kept. The 16 signals are summed instead of requiring a coincidence between 2 PMT signals of the same bar to increase the detectors efficiencies for K^+ detection. Figure 2.13 is the drawing of the electronic setup up for the eight lucite bars. The entire trigger system is discussed later.

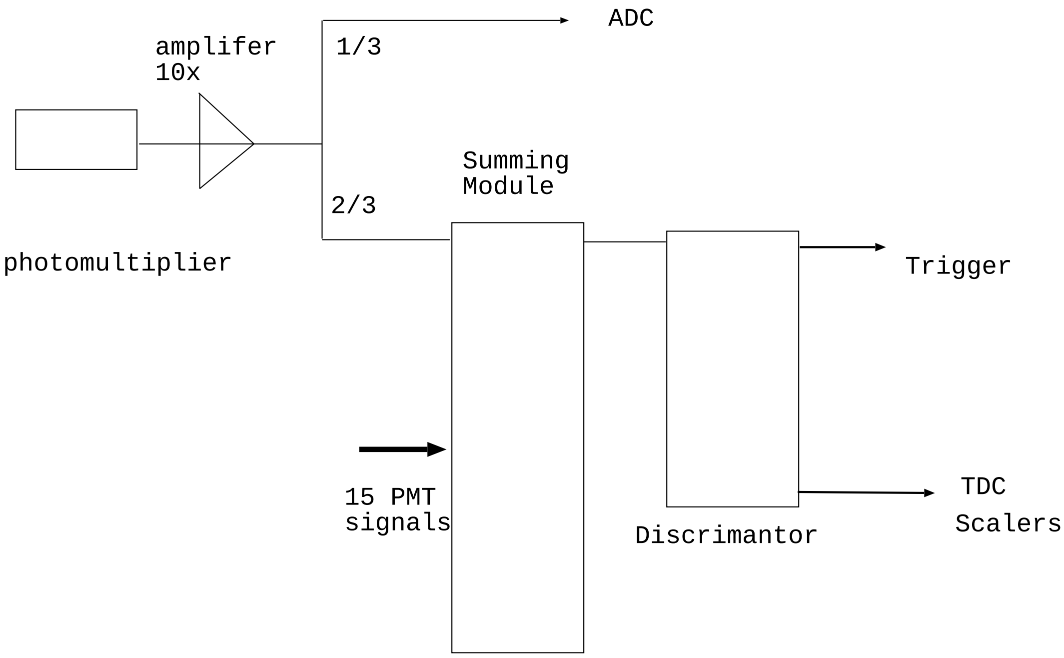

Figure 2.13: Lucite bars electronic setup

2.7.4 Performance

The detector efficiency was measured by comparing the data taken with the lucite in and out of the trigger at different threshold values. Figure 2.14 shows the comparison of three different test runs. The data was first taken without the lucite in the trigger and then at 1 photoelectron (PE) threshold level and again at 6 PE level. By requiring the signal to be larger that 1 PE the protons are reduced by 45%. Figure 2.14 shows qualitatively the ability of the lucite to decrease the proton background rate significantly in order to reduce the number of junk events written to tape. The aerogel Čerenkov veto in the trigger reduced the pion background in figure 2.14. The lucite is not necessarily needed off-line as a particle identification device due to the fact that protons and kaons can be effectively separated by TOF in the detector hut. Figure 2.15 shows the offline cut efficiency for the lucite detector. The three curves are for three different β regions: β greater 0.96 (pion region), β greater than 0.90 (kaon region), and β less than 0.9 (the proton region). The cut efficiency for the protons at 3 PE is 75% efficient and 98% efficient for kaons. Ideally the lucite Čerenkov detector in the trigger should have removed all protons from the data stream. From figure 2.14, the spectrum shows that there are still a significant amount of protons. The model is based on particle incident perpendicular to the detector. In the SOS detector hut the outgoing angle of particles may vary with $\pm 8°$. When a particle which is below the TIR threshold has an angle other than $0°$, then light can be collected at one end of the lucite

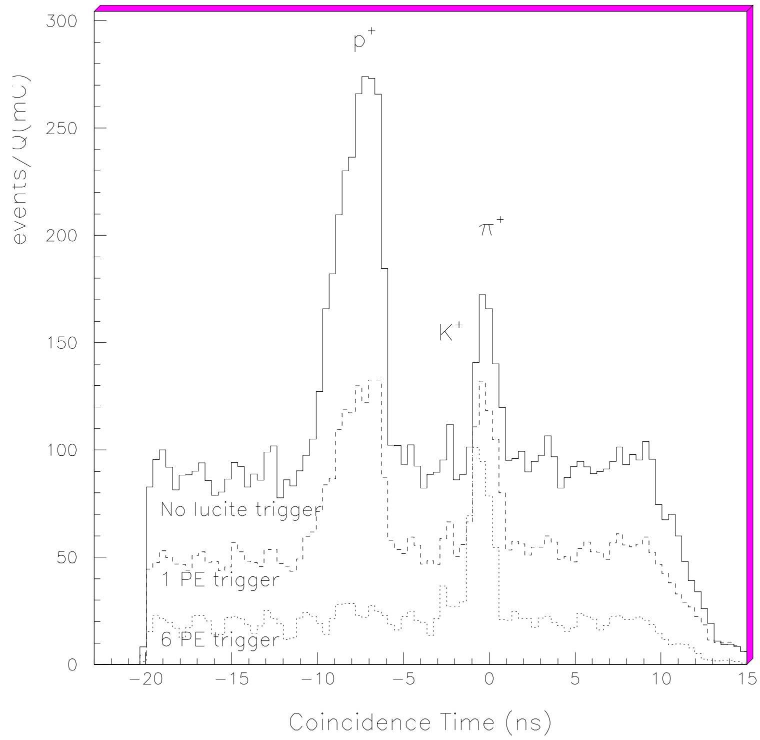

Figure 2.14: Lucite detector in the SOS kaon trigger at 1 photoelectron (PE) and 6 PE discrimination level.

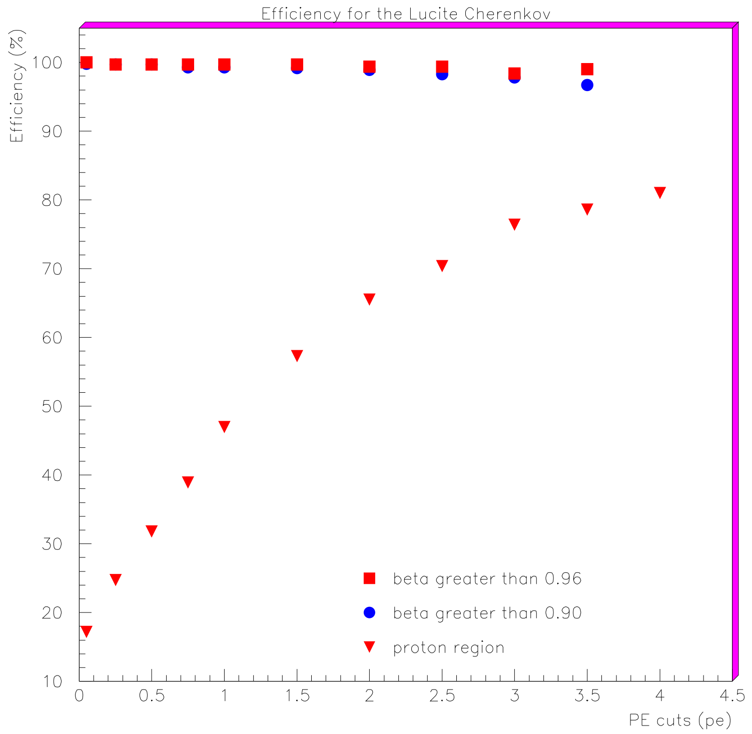

Figure 2.15: Cut efficiency for the Lucite detector. The different symbols represent the various particle regions.

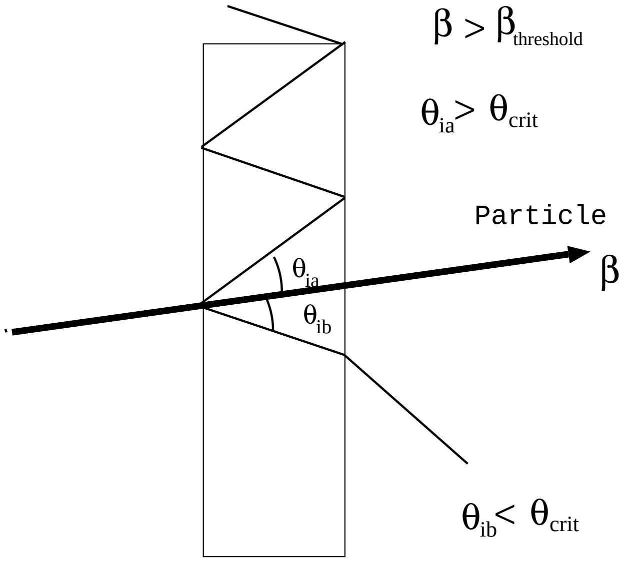

Figure 2.16: Particle incident $\pm 8^{\circ}$. Light TIR only on one side.

bar as seen in figure 2.16. The same is possible for a particle that is above the TIR threshold but lose signal from one side. Because of this all 16 photmultipliers signals were in OR mode and then discriminated, instead of requiring a coincidence between the two PMTs' on the same bar. Requiring a coincidence between PMTs would throw away many good K^{+} events. Therefore some protons are in the spectrum due to the incident particle's angle. In Figure 2.12, the prototype test in BNL shows this minimum background of two photoelectrons at $\beta = 0.88$. Ideally there should have been no photoelectrons seen by the PMT in this case because the threshold cutoff for TIR is at $\beta = 0.90$.

2.8 Coincidence kaon trigger

The experiment was (e,e$'$K$^+$), where the scattered electron and kaon were detected in coincidence. The trigger was setup to accept coincidence events and also single events from both spectrometers. Each spectrometer has its own separate trigger system.

2.8.1 HMS trigger

The HMS was used to detect the scattered electron. The background events were mainly π^-. The first part of the HMS trigger is formed by a 3 out of 4 (3/4) hodoscope plane signal. This signal is produced every time a charged particle, either e$^-$ or π^-, passes through the scintillators. The next part of the trigger is formed by the gas Čerenkov or calorimeter for particle identification (PID). The gas Čerenkov trigger was formed by summing the two PMT's and setting a threshold discrimination for signals above 1 photoelectron. Electrons could be identified in the lead glass calorimeter when it registered two logic signals. The sum of all blocks were discriminated to form a **'SHSUM'** signal. The sum of all blocks in the first layer were discriminated to form the preradiator signal **'PRSUM'**. The preradiator had two outputs,**'PRHI'** and a lower threshold **'PRLO'** using a high and low discriminator threshold setting, while the total energy signal has one output **'SHLO'**. For an event to be accepted as a valid electron it must meet one of two conditions **'ELHI'** or **'ELLO'**. **'ELHI'** requires a high calorimeter signal and

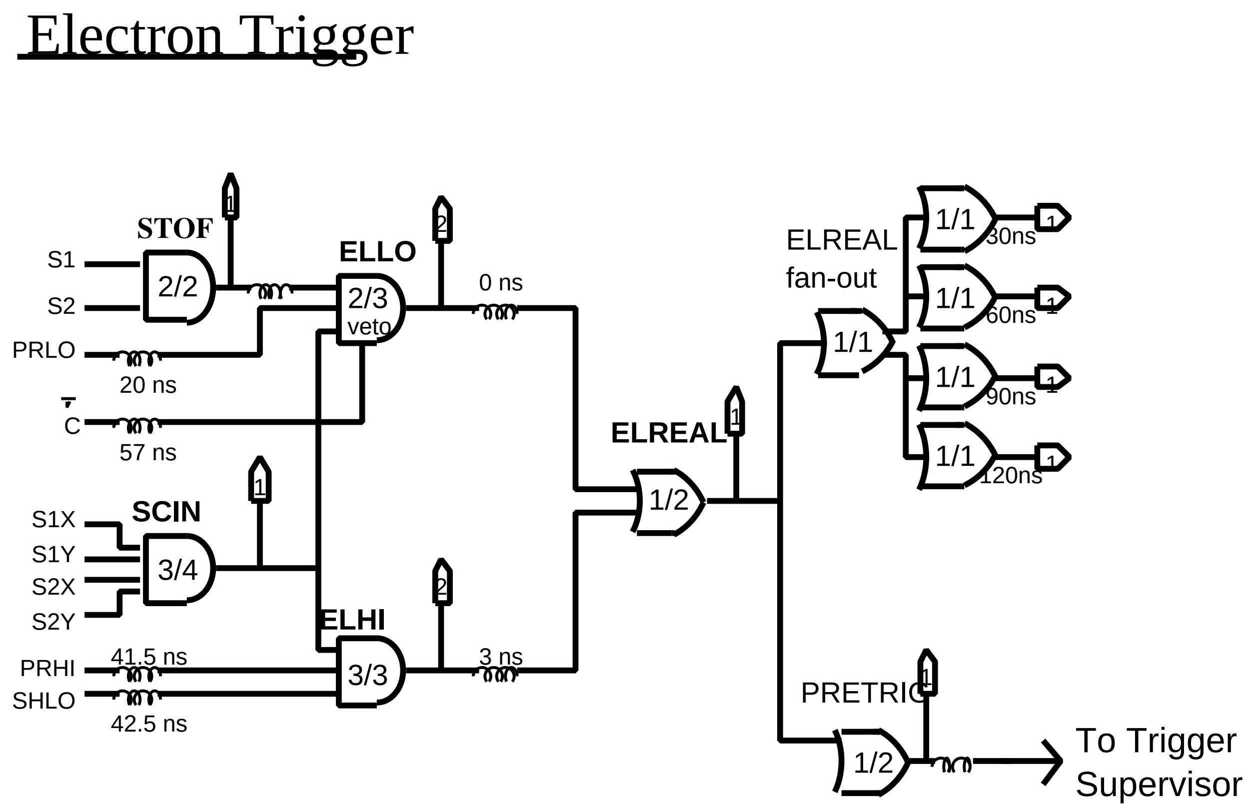

Figure 2.17: HMS electron pretrigger logic diagram describing the pretrigger for electrons.

no Čerenkov. It is defined as the coincidence of the 3/4 hodoscope planes, high preradiator sum, and total energy sum from the calorimeter. A Čerenkov signal is required for **'ELLO'**. It is defined as a either a 3/4 coincidence of the hodoscope planes or a less restrictive coincidence of one of the front planes and one of the back planes, and a shower counter signal along with the Čerenkov signal. These form the HMS trigger **'ELREAL'** either **'ELLO'** OR **'ELHI'**. Figure 2.17 shows the logic diagram of the electronic setup of the HMS trigger.

2.8.2 SOS trigger

In the hadron arm, the SOS, K^+ mesons were detected in a large background of protons and π^+ mesons, and potentially a small contamination of e^+'s. The first part of the trigger is identical to the HMS, with 3/4 hodoscope planes. The PID part of the trigger requires different detectors. The aerogel Čerenkov was used to reduce the π^+ background. The aerogel's PMTs were summed in a "shoelace" configuration, alternating from +y to -y sides. Each of these summed signals were discriminated at 3.5 PE. These logic signals were sent to the main pretrigger as a veto signal. The 16 lucite PMTs were summed and then discriminated at 3 the PE level. The kaon trigger consist of 3/4 hodoscope, veto aerogel Čerenkov, and lucite Čerenkov. Figure 2.18 is the logic diagram of the electronic setup for the kaon trigger.

2.8.3 Trigger Supervisor

The signals from the pretriggers are sent to the trigger supervisor, hardware scalers, and TDCs. The scalers allow us to look at raw rates. The coincidence between the HMS and SOS signals are formed at the programmable logic module, 8LM. The trigger supervisor (TS) reads out all the needed detector information. The logic diagram for the TS and 8LM is shown in figure 2.19. The 8LM receives six different signals. Three of these signals are received from the TS. **'TS GO'**

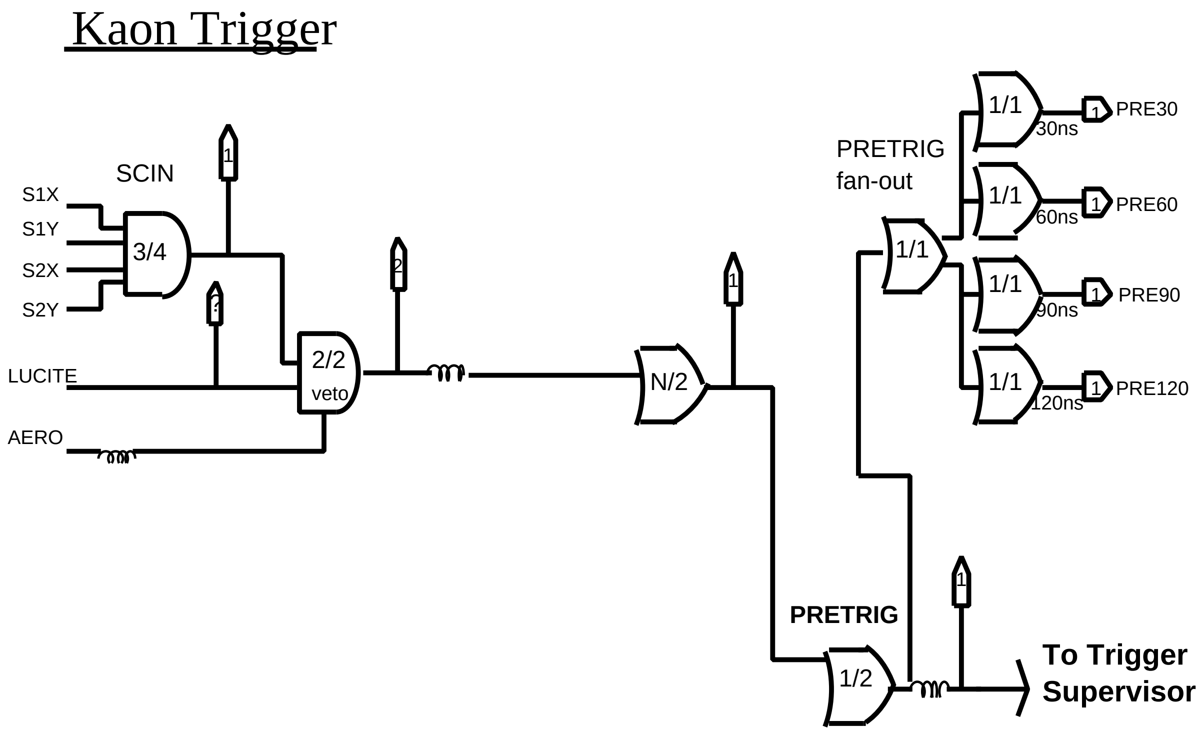

Figure 2.18: SOS kaon pretrigger logic diagram describing the pretrigger for kaons

indicates that a run is in progress. **'TS EN1'** signals that normal data are being taken. These are true events and not pedestal events. When the TS is processing events then the 8LM receives the signal **'TS BUSY'**. The other two signals come from the HMS pretrigger and SOS pretrigger. The signal **'PED PRETRIG'** is present at the beginning of the run when 1000 pedestal events are taken. The 8LM in turn forms eight outputs. The original HMS pretrigger, SOS pretrigger are produced as outputs. When a HMS and SOS pretrigger signal coincide then a **COIN PRETRIG** is produced. The other four outputs are the trigger signals corresponding to the pretrigger outputs. The **HMS PRETRIG** signal width was approximately 30 ns at the input of the 8LM, and the **SOS PRETRIG** signal

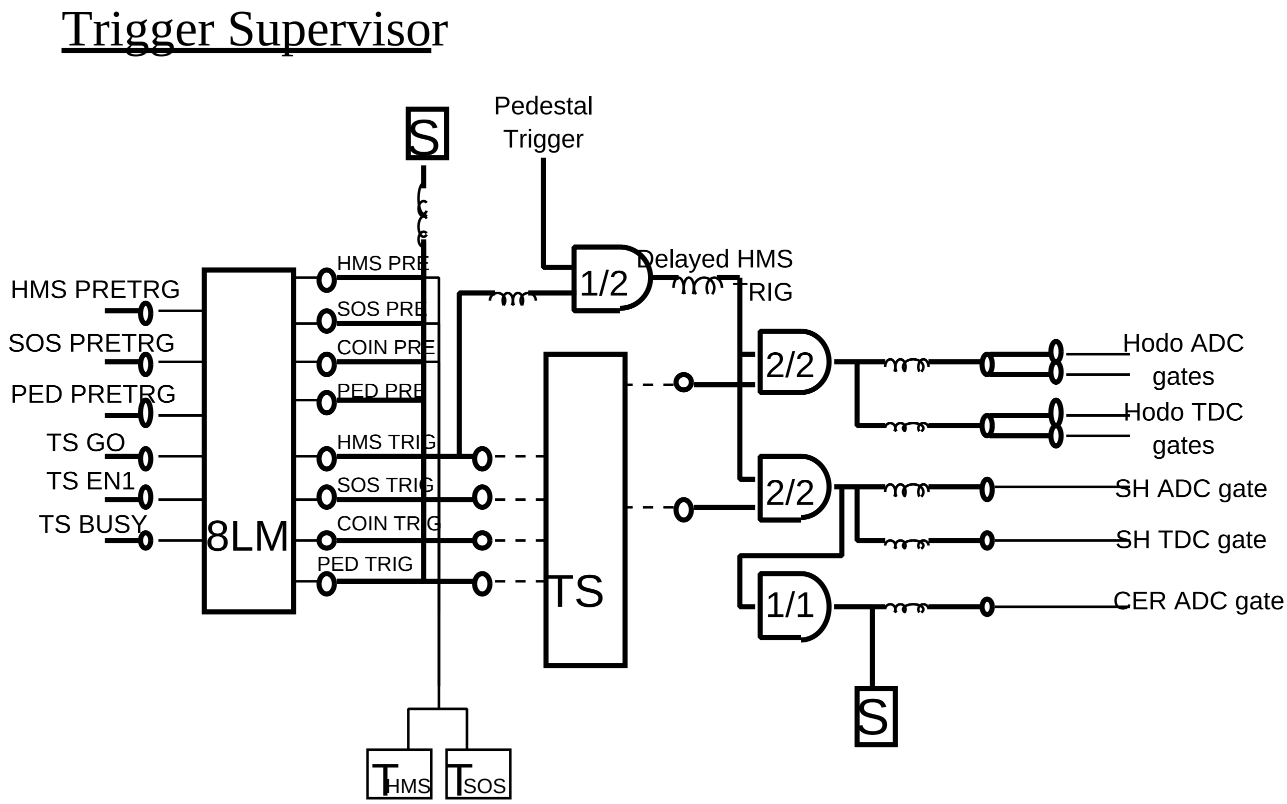

Figure 2.19: Trigger supervisor and 8LM coincidence logic diagram.

width was approximately 10 ns. This creates a coincidence time window 40 ns wide for a **COIN TRIG**. The TS prescales away all singles events which do not have a **COIN TRIG** signal.

CHAPTER 3

DATA ANALYSIS

3.1 Replay Engine

The data acquisition was managed by CODA (CEBAF Online Data Acquisition) software system. The raw ADC, TDC, and scaler information are analyzed using the standard Hall C event reconstruction software package. These raw data events were analyzed using a FORTRAN code called replay ENGINE. [22] ENGINE decodes the raw data, generates tracks and detector identification information for each event. This information is put into three different files, scaler report files, PAW ntuples and histograms. [23] The scaler report files contain information about the various detectors such as efficiencies, dead time correction factors,beam line information, and the integrated charge of the beam. The histogram files contain detector summary information which can be used to check the hardware during a run. The PAW ntuples contain the event-by-event physical information,tracking information, reconstructed quantities, and particle identification information which allows the data to be manipulated for physics analysis.

3.2 Tracking

The tracking information is gathered from the drift chambers in both spectrometers. Before tracking is attempted at least 5 out of the 6 wire planes must have a hit. The tracking algorithm defines a 'space point' from each 'hit' wire. The 'space points' between planes are linked to form 'stubs'. The 'stubs' between the two chambers with the minimum χ^2 is selected as the best track. There can be more than one track and sometimes there may be no track found for an event. The best track is projected to the focal plane to give the position x_{fp}, y_{fp} and slope x'_{fp},y'_{fp} at z=0. A detailed account of the tracking algorithm is found in [24]. The focal plane quantities are then used to reconstruct the target quantities and momentum. Each spectrometer has a transport matrix $M^{(i)}$.

$$R_{tar} = \sum^{n} M^{(i)}(x_{fp})(y_{fp})(x'_{fp})(y'_{fp})$$

R_{tar} are the reconstructed target quantities. The transport matrix was initially determined by COSY INFINITY [25] model transport code. The matrix elements were fine-tuned by taking calibration data with a sieve slit between the spectrometer and target. The sieve slit collimator is a solid piece of Heavymet with holes drilled through it. The center of each hole defines a specifically measured θ and ϕ from a point target. The calibration data were collected from a thin carbon target, slanted, 30° with respect to the horizontal. By reconstructing back to the holes in the sieve slit transport matrix elements and the angular reconstruction resolution were determined by a fitting procedure. [26] This is done for both spectrometers. The final matrix elements were used in the analysis replay ENGINE.

3.3 Particle Identification

The first task in analyzing the data was to identify the coincidence particles, e^- and K^+. The trigger decreases the number of background particles but does not eliminate them. There were a significant amount of π^+,p^+, and π^- in the data stream. Particle identification was performed with the aid of the ADC and TDC of various detectors in the hut and the time of flight (TOF) calculation. TOF is the amount of time it takes the particles to travel the distance between the first and last scintillator planes.

3.3.1 Electron Identification

The scattered electron were detected in the HMS. Along with the scattered electron were background π^- hadrons. The β of e^- and π^- are indistinguishable, as seen in figure 3.1, therefore a TOF cut could not be used. Figure 3.2 shows that the gas Čerenkov is capable of separating π^- and e^-. The average yield for electrons in the gas Čerenkov is 15 photoelectrons whereas the π^- have no signal in the gas Čerenkov at this momentum. A software cut of 3 photoelectrons in the

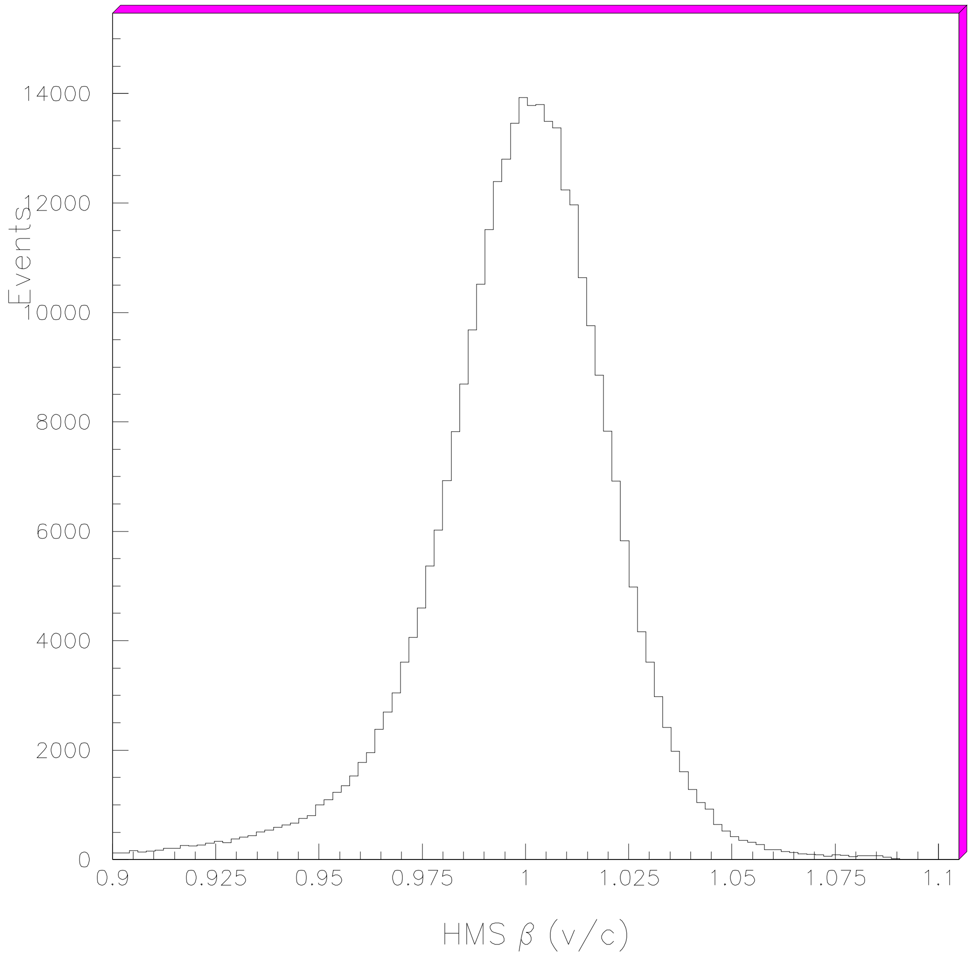

Figure 3.1: HMS β spectrum with both π^- and e^-.

gas Čerenkov eliminated the π^-. This cut was sufficient to remove 99.8% of the π^- background.

3.3.2 Kaon Identification

The K^+ mesons detected in the SOS were identified after applying various software cuts to remove the pion and proton background. Figure 3.3 shows the

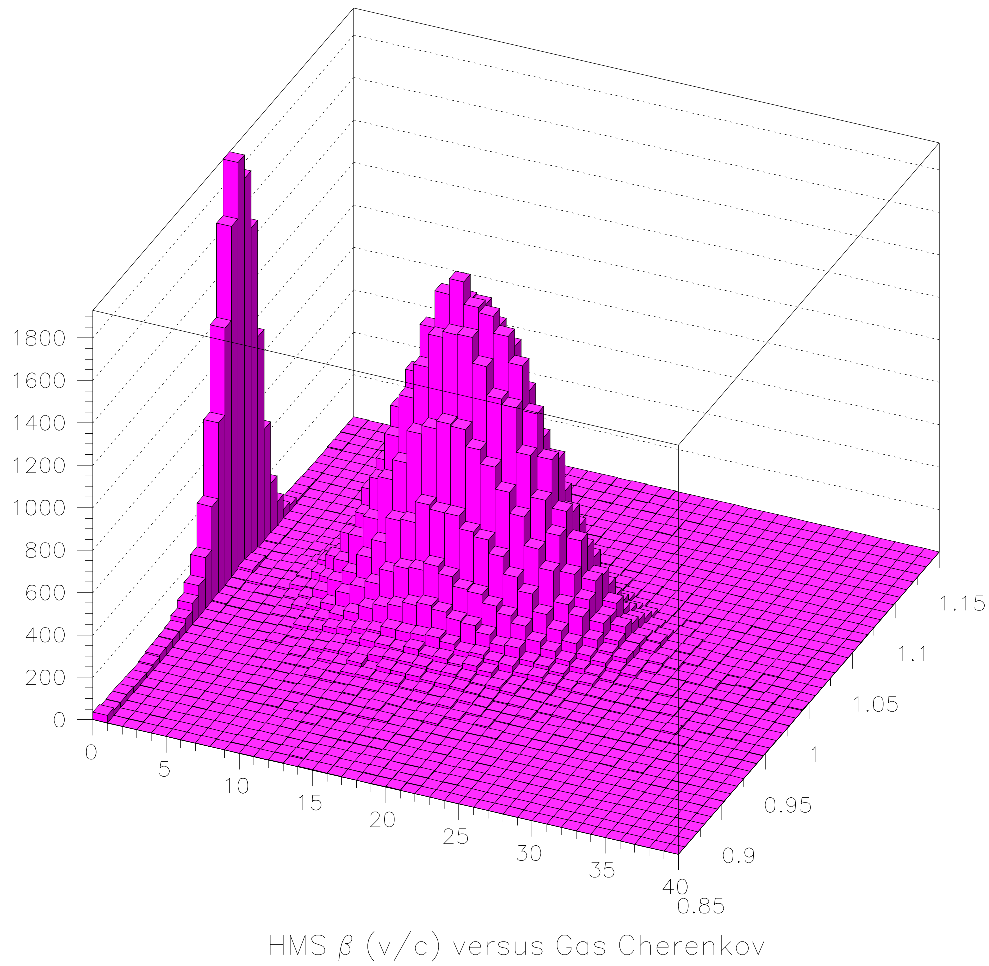

Figure 3.2: HMS β versus gas Čerenkov. Where the separation of the pions (left) and electrons(right) can be seen.

velocities of the hadron in the SOS. The π^+ and p^+ are easily recognized but the K^+ is barely seen as a shoulder on the π^+ peak. The lucite Čerenkov was not in the trigger for this particular run shown in figure 3.3. The protons and kaons are easily separated with a TOF cut at $\beta = 0.89$, to remove the proton background. A tighter aerogel cut of 3 photoelectrons reduces the pions, but does not remove them. The TOF information was used in the form of a mass square cut ($\mathcal{M}^2$), where $\mathcal{M}^2$ is defined by equation (3.1) and P_{SOS} is the momentum of the particles in the SOS. Table 3.1 list the square and masses of each charged hadron. A double gaussian was used to fit the pion and kaon peaks after removing the protons. The fit parameters were then used to generate the gaussian function for the pion peak, F_π, and the kaon peak, F_k, the solid lines in figure 3.4 represent these distributions. These function were subtracted to remove the pions background from the kaons. The dash line in figure 3.4 represents the remaining kaons after the function subtraction.

$$\begin{aligned}
\beta &= \frac{P_{sos}}{E} \\
E &= \sqrt{P_{sos}^2 + m^2} \\
\beta^2 &= \frac{P_{sos}^2}{P_{sos}^2 + m^2} \\
\mathcal{M}^2 &= (\frac{1}{\beta^2} - 1) \times P_{sos}^2
\end{aligned} \tag{3.1}$$

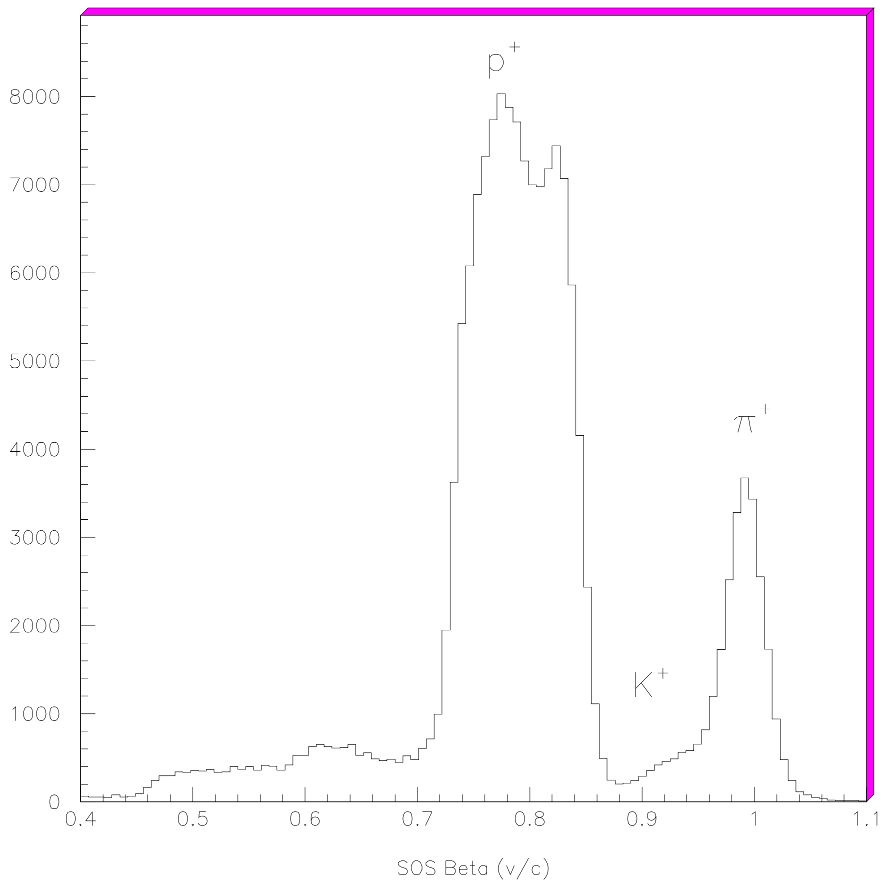

Figure 3.3: SOS β spectrum with aerogel in the trigger at a total of 7 photoelectrons threshold.

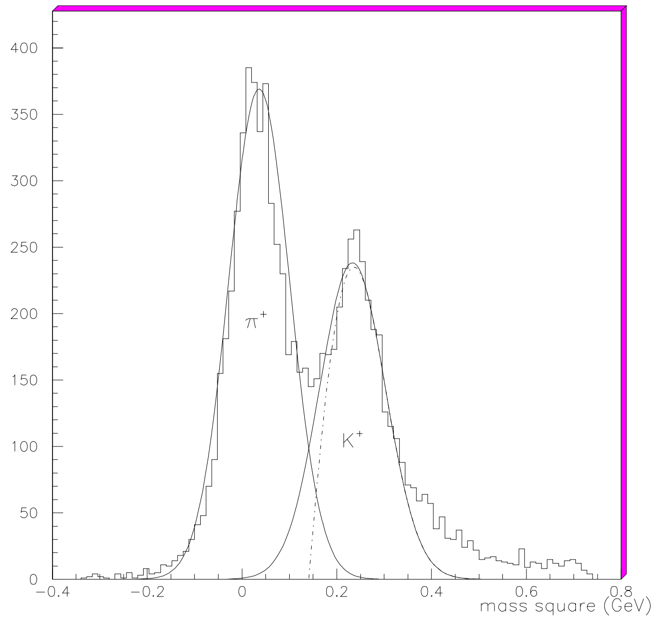

Figure 3.4: Plot of the mass squared of the π^+, K^+, with the aerogel software cut and β cut for p^+.

Particles	mass (GeV)	$\mathcal{M}^2$ (GeV^2)
π^+	0.1396	0.0195
K^+	0.493	0.243
p^+	0.938	0.880

Table 3.1: Hadron mass and $\mathcal{M}^2$ values

3.3.3 Coincidence Cuts

The final cut on the data was a cut in the coincidence timing window. The electron and kaon were detected in coincidences with each other to form a coincidence event, which is the timing difference between the two arms. There are also random coincidences between uncorrelated kaon and electron events. The real coincidence events, kaons at 0 ns, pions at +2 ns and protons centered at -5 ns, the darker distribution, shown in figure 3.5, along with the lighter random coincident events. Figure 3.5 does not include the previously discussed PID cuts. These random coincidences were subtracted from the real and random coincidences. The plot has been offset to place the real kaons at 0 ns. The path-length of the particle through the spectrometer has been corrected with the assumption that the particle was a kaon. [27] This creates a better resolution for the K^+, but broadens the proton and pion distribution. A 2 ns cut was placed around the 'real' coincidence kaon, the large shaded peak at 0 ns in figure 3.6. A sample of seven random peaks, for carbon, were used to get a good statistical estimate of the random events. The random peaks were selected so as not to contaminate them with real pion and proton feed through. Four peaks were selected beginning 4 ns after the real kaon peak in the positive direction to avoid the real pion peak. Three peaks, 8 ns before the kaon peak in the negative direction were selected to insure no real coincidence proton was selected. The weighted average of the 7 peaks were subtracted from the 'real' peak to obtain the 'true' kaon coincidence.

During the first running of carbon it was discovered that a temperature problem in the electronics room caused a fluctuation the coincidence timing. Figures 3.7 and 3.8 show the variation of the average coincidence time from run to run. Figure 3.8 show the temperature of the electronic room variation from run to run. The data were taken during one 24 hour period.

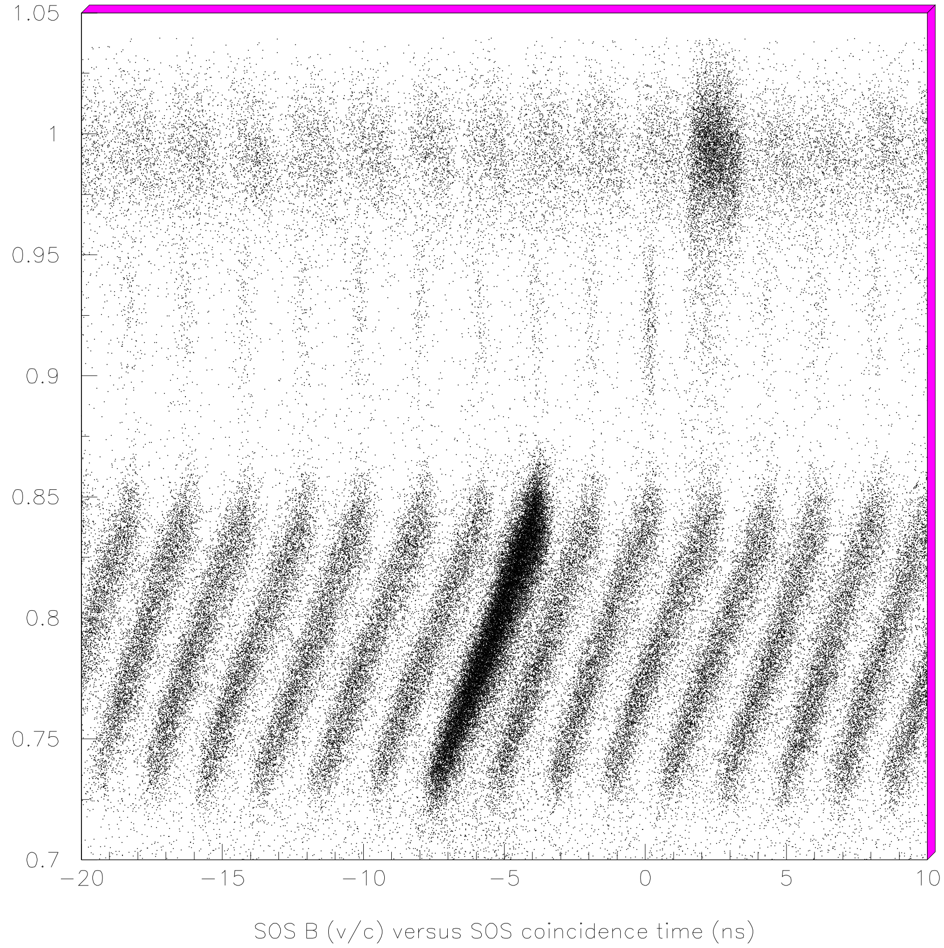

Figure 3.5: Coincidence timing (ns) versus β. More denser areas correspond to real coincidence events. The real coincidence K^+ have been boxed.

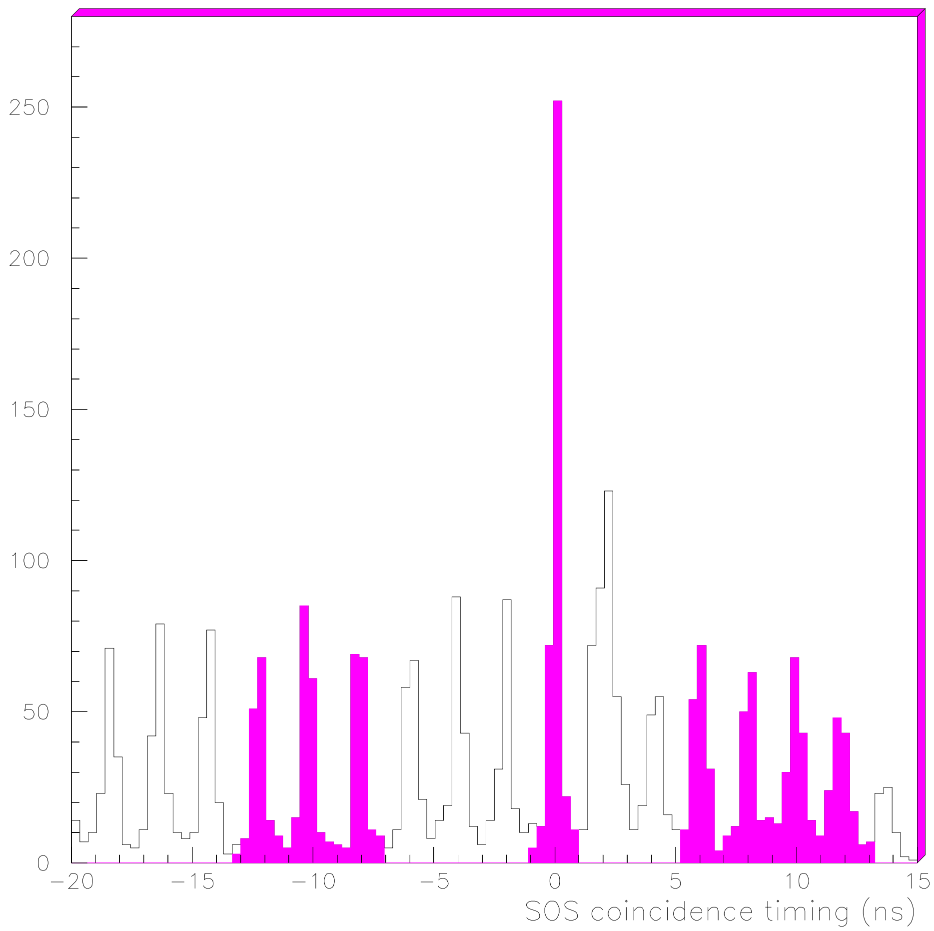

Figure 3.6: SOS Coincidence timing with random and real kaon events. Shaded events represent the real and random events.

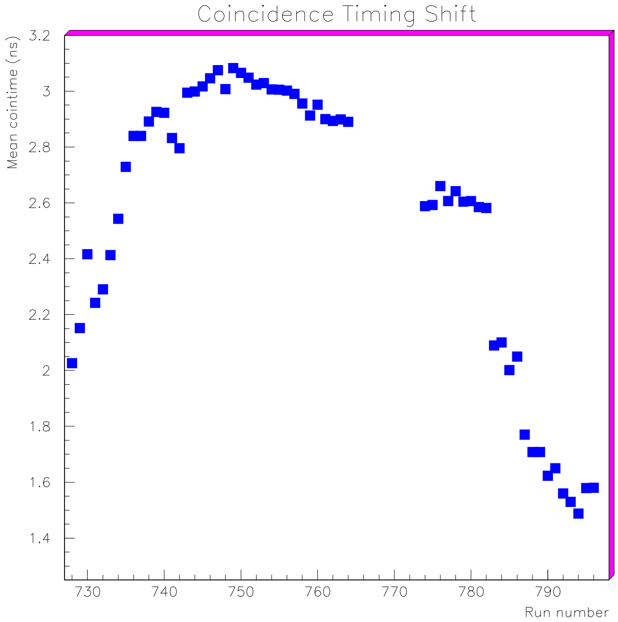

Figure 3.7: Plot of coincidence timing shift versus run number.

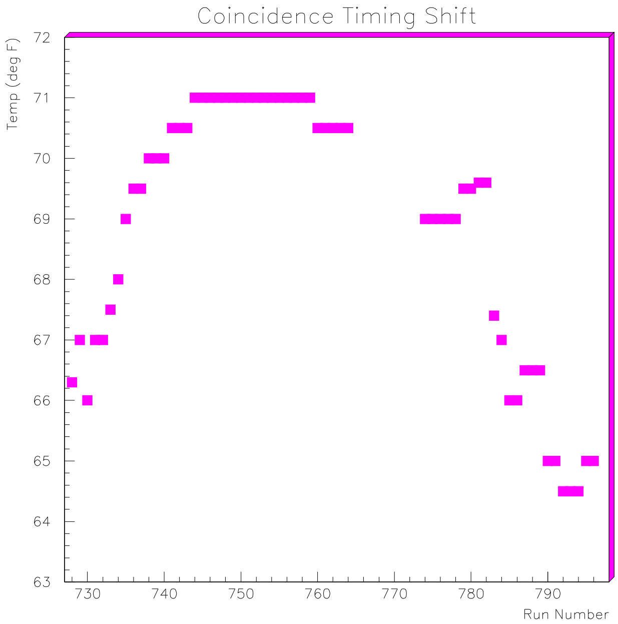

Figure 3.8: Plot of electronic room temperature versus run number.

3.4 Corrections to the Data

Following the identification of the 'true' coincidence e' and K^+ events, the missing mass was calculated. The yield has to be corrected for losses due to kaon decay, absorption, and detection efficiencies. The various corrections and the associated errors are discussed in the following section.

3.4.1 Energy Correction

During the running the of the experiment, it was discovered that the beam energy was unstable at the level of 5×10^{-4}. Movement of the beam position in the Hall C beam line was observed in the beam position monitoring system. Figure 3.9 and 3.10 show the energy drift for both carbon I and carbon II runs. By monitoring the beam position inside the Hall C arc, a correction factor on the beam energy drift can be computed. The corresponding BPM information was recorded every 30 seconds. This does not provide enough information to adequately correct the energy shifting. The uncertainty of the beam energy results in a broader energy resolution and the possible smearing of states with smaller cross section.

There are some known corrections that were not included in the final analysis of Engine replay, such as, the SOS momentum setting is incorrect by 0.25% for a 1.20 GeV/c central setting, the beam energy is incorrect by 0.15% from an incorrect magnet setting. The reconstruction of the missing mass of the hydrogen

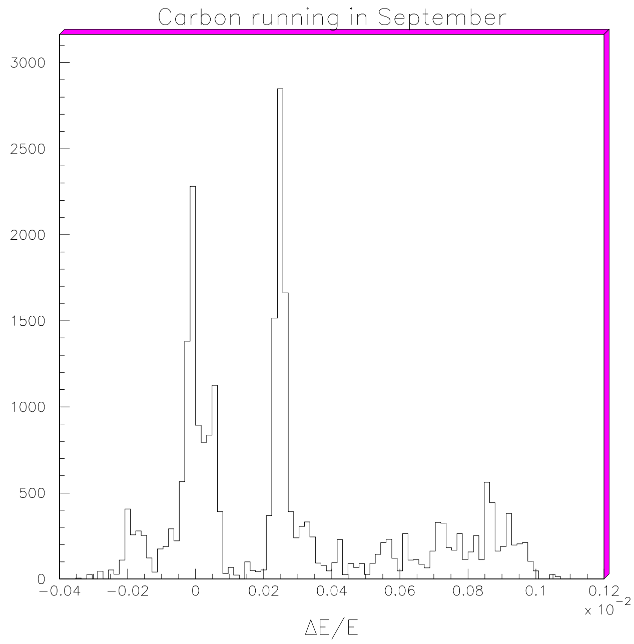

Figure 3.9: ΔE/E for carbon I running in September.

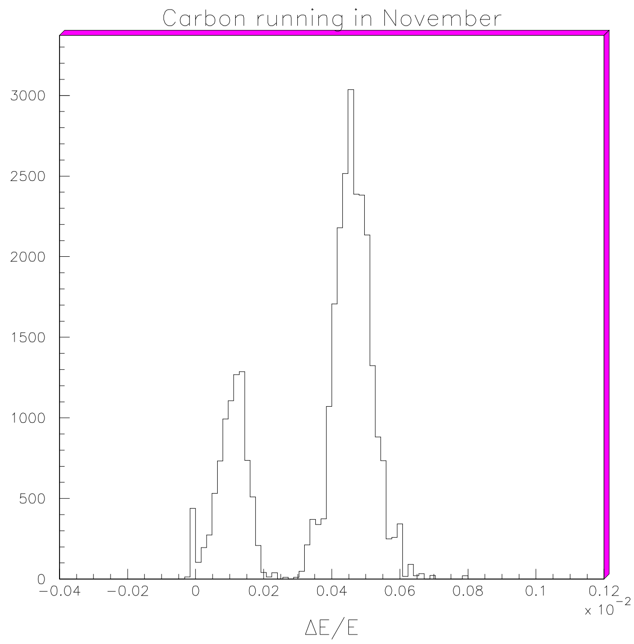

Figure 3.10: ΔE/E for carbon II running in November.

target has an offset of 9.0 Mev in missing mass for the Λ centroid peak. Figure 3.11 shows the uncorrected Λ and Σ^o missing mass plot. The dashed line indicates the correct value, 1.115 Gev, for the Λ peak. To correct this offset an overall correction was applied to the HMS momentum value. This takes the corrections of the entire system; beam, target, and spectrometers, and places the error in the HMS spectrometer. The HMS momentum was adjusted until the Λ peak lined up at the correct value. The correction to the momentum was estimated to be 0.0125 GeV/c (0.7%). This offset in momentum was also included in the deuterium, carbon and aluminum data analysis.

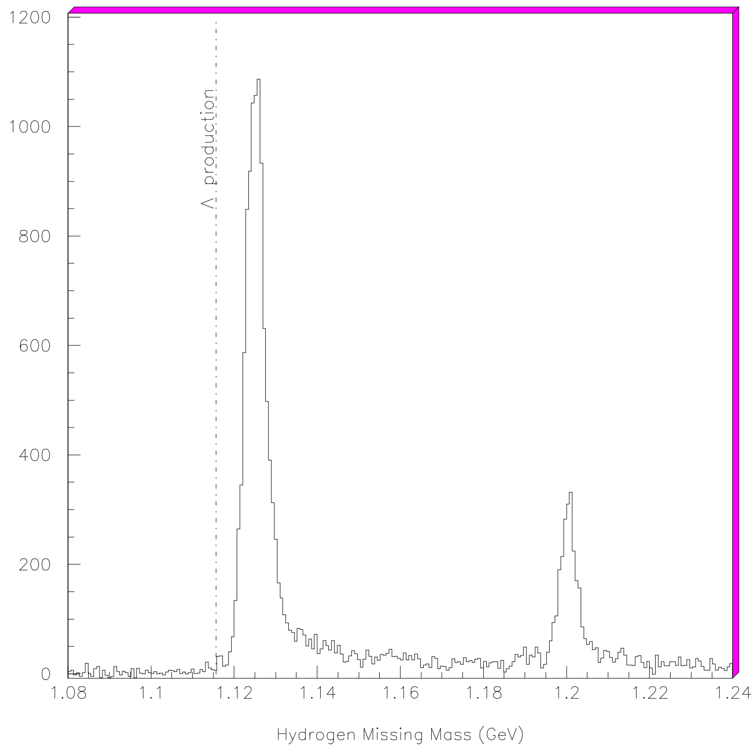

Figure 3.11: Uncorrected missing mass of Λ and Σ^o. Dash line represents the correct position of the Λ mass at 1.115 GeV.

3.4.2 Tracking and Trigger Efficiencies

Tracking efficiency is a measure of the events for which a track could not be found. The wire chamber tracking information is not part of the trigger, so a trigger event may not have good tracking information. This could be caused by having too much or too little information for an event. Tracking efficiency for kaons was not directly tested due to the low statistics. The efficiency is a measure of tracks that pass through the center of the spectrometer. This is a fiducial cut and it only includes events for which central paddles of the scintillator fired.

The tracking efficiency is calculated by dividing this value by the number of these events that have good tracks. This is called the fiducial tracking efficiency. The HMS wire chambers are on the order of 96% efficient. The SOS wire chambers are on the order of 89 % efficient.

The hodoscope are considered 99.8% efficient for each scintillator bar. Section 2.8 discussed the coincidence trigger which required 3/4 scintillators fire as defined in the trigger for both the HMS and SOS. The efficiency of the hodoscope is measured by comparing events which have 3/4 hits as opposed to those which have 4/4 hits. The scintillator trigger efficiency was compared on a run-by-run basis and the error associated with the trigger is 0.1%.

3.4.3 Computer and Electronic Dead time

When the data acquisition is busy processing an event no other events may be processed during this time and results in a computer dead time. The dead time for the computer is calculated by dividing the triggers by the pretriggers minus one. Triggers are events which are processed by the Trigger Supervisor (TS) and pretriggers are the total number of triggers formed.

$$dt_{comp} = \frac{Trig}{Pretrig} - 1 \tag{3.2}$$

By running in buffered mode the dead time is decreased. Buffered mode allows events to be stored in a buffer while the computer processes the earlier events. The major concern when running in buffer mode is the possible loss of synchronicity where TDC readouts for one event are attached to a different event. Synchronicity was checked for every thousand events and the buffers were flushed to enforce a resynchronization. Most of the data were collected in buffered mode which resulted in a computer dead time of typically 11%.

Electronic dead time occurs when two events arrive at the logic module within the same window, hence the second event is not processed. The window for the logic modules were set to 30 ns for data taking. The number of triggers lost during the 30 ns window was compared to the number of triggers when using windows set at 60 ns and 120. The differences between triggers from the 120 ns window and 60 ns window is divided by 2; and then divided again by the triggers from a 30 ns window to obtain the electronic dead time.

$$dt_{elec} = \frac{[N(120) - N(60)]/2}{N(30)} \tag{3.3}$$

The dead time for the electronics in each spectrometer for the carbon target was about 1%.

3.4.4 Coincidence Blocking

When a random single event arrives at the trigger supervisor before a coincidence event, it can lead to a mis-timing in the coincidence time logic. The coincidence time for that event will be offset by a significant amount, and that event falls outside the 40 ns coincidence window cut. Figure 3.12 is the total picture of the coincidence window. The shaded areas are outside the 40 ns coincidence window. Some of the events in the shade area contain 'true' coincidence events. The ratio of the blocked coincidences over the total number of coincidences give a coincidence blocking correction of 10% for the carbon target. This is a larger correction compared to the hydrogen, 3%, or deuterium, 4% cases. The higher correction for the carbon data is due to the higher singles rates for carbon. A complete discussion of coincidence blocking can be found in [17].

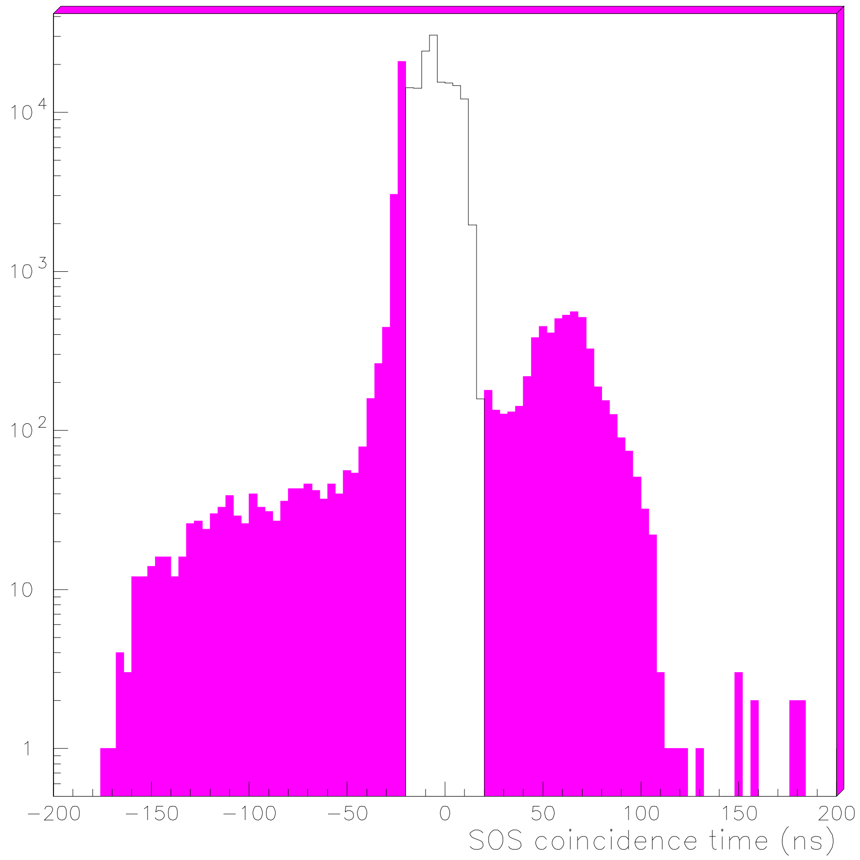

Figure 3.12: Coincidence timing in the SOS. The shaded area is outside the 40 ns coincidence window.

3.4.5 Kaon Decay

The K^+ meson has a mean life time of $\tau = (1.237 \pm 0.0029) \times 10^{-8}$ s. The kaon survival probability $\mathcal{E}_K$ is given in equation (3.4) [28].

$$\mathcal{E}_K = \exp\left(\frac{-L}{\gamma_K * L_o}\right) \tag{3.4}$$
$$\gamma_K = \frac{E_K}{m_K}$$

Where L is the length from the target to the aerogel plane, equal to 9.8 m. L_o is the decay length of kaon (371 cm). This gives a survival probability of 37%. The Monte Carlo simulation code, which is discussed later, includes this kaon decay. Table 3.2 lists the decay channels of the K^+ meson. When K^+ decays in the spectrometer magnet the decay products do not often contribute to the detection of a K^+. A fraction of the decay products which form in the detector hut will trigger as a kaon. If the decay particle was detected as a K^+ this would lead to double-counting. This overall double-counting correction is on the order of 3%.

Decay modes	Branching Ratio
$\mu^+\nu_\mu$	$(63.51\pm0.18)\%$
$\pi^+\pi^0$	$(21.16\pm0.14)\%$
$\pi^+\pi^+\pi^-$	$(5.59\pm0.05)\%$
$\pi^+\pi^0\pi^0$	$(1.73\pm0.04)\%$
$\pi^0\mu^+\nu_\mu$	$(3.18\pm0.08)\%$
$\pi^0 e^+ \ \mu_e$	$(4.82\pm0.06)\%$

Table 3.2: K^+ decay modes with branching ratios. The values come from the Particle Data Book.

3.4.6 Kaon Absorption

The kaon can be absorbed as it travels from the target to the detectors. The particle generally travels in a vacuum system. Various vacuum windows, portions of detectors and even the target are potential points of absorptions through elastic/inelastic scattering. The materials which the kaon interacted with is listed in Table 3.3. The expected fraction of particles absorbed can be calculated by the expression in equation (3.5), n_o is the number of particles entering the material, N_A is Avogadro's number 6.022×10^{23} mol^{-1}, A is the mass number of the material, t is the thickness, and σ_o is the absorption cross section given in equation (3.6). Taking all the materials into account an over all absorption correction of 5% was used to correct the yields.

$$n = n_o \frac{N_A \rho}{A} t \sigma_o \tag{3.5}$$

$$\sigma_o = 21.065 p_K^{-0.99} A^{0.79} \tag{3.6}$$

3.4.7 Cut Efficiencies

The various PID cuts discussed in the previous section are listed in Table 3.4. These cuts where used to select a clean sample of coincidence K^+-e' event. The efficiencies of the PID cuts were evaluated and are included in table 3.5.

Material	ρ (g/cm^2)	Thickness (cm)	λ (g/cm^2)	X (g/cm^2)	X/λ x1000
Aluminum chamber window	2.70	0.0203	88	0.0548	.62
Spectrometer					
Air	0.00121	15	75	0.0182	0.24
Kevlar	.74	0.0127	70	0.0094	0.13
Mylar	1.39	0.0076	72	0.0106	0.15
Kevlar	.74	0.0127	70	0.0094	0.13
Mylar	1.39	0.0076	72	0.0106	0.15
Detector Hut					
Air	0.00121	15	75	0.0182	0.24
Mylar cathode	1.39	0.0076	72	0.0106	0.15
Wire	19.3	0.0024	147.7	0.0463	0.31
Ar/Ethane	0.0015	3.7068	70	0.0056	0.08
Mylar	1.39	0.0076	72	0.0106	0.15
Wire	19.3	0.0024	147.7	0.0463	0.31
Ar/Ethane	0.0015	3.7068	70	0.0056	0.08
Mylar	1.39	0.0076	72	0.0106	0.15
Polystyrene scint S1Y	1.03	1.10	70	1.133	16.19
Polystyrene scint S1X	1.03	1.04	70	1.0712	15.3
Čerenkov windows	1.39	0.06	70	0.0834	1.19
CO_2	0.002	100	76.5	0.200	2.61
Mirror			70	0.45	6.43
Lucite	1.1600	2.5400	71.4	2.9464	41.27
Polystyrene scint S2Y	1.03	1.10	70	1.133	16.19
Aluminum housing for aerogel	2.7	0.159	88.0	0.4293	4.88
Aerogel	0.2	8	80.6	1.6	19.85
Total					126.80

Table 3.3: SOS materials contributing to kaon absorption and multiple scattering.

Acceptance cuts for data and SIMC	
HMS	
$\|hms\ delta\|$	< 10 (%)
$\|hms\ xptar\|$	0.08 (rad)
$\|hms\ yptar\|$	0.04 (rad)
SOS	
$\|sos\ delta\|$	< 20 (%)
$\|sos\ xptar\|$	0.04 (rad)
$\|sos\ yptar\|$	0.07 (rad)
PID cuts on data	
hms Čerenkov	> 1 (npe)
sos aerogel Čerenkov	< 2 (npe)
$\|cointime - (K^+\ peak\ position)\|$	< 1 (ns)
β	> 0.88
mass square(beta calculation)	>0.40

Table 3.4: Summary of cuts applied to the data and SIMC.

	Correction (%)
SOS tracking	11
HMS tracking	4
Electronic dead time	1
Computer dead time	11
Coincidence blocking	10
Lucite Čerenkov	3
Aerogel Čerenkov	4
Gas Čerenkov	.2
Hodoscope trigger	.2
($\mathcal{M}^2$) mass square cut	4
β cut	4
Decay	6
Absorption	5

Table 3.5: Data Correction due to inefficiencies in the detectors, electronics and cuts.

CHAPTER 4

MONTE CARLO SIMULATION

In order to analyze the quasifree strangeness production on carbon and aluminum targets a Monte Carlo simulation of the data was needed. The Monte Carlo simulation used for Hall C is called SIMC. It is based on the code SIMULATE [29] developed for the SLAC NE18 color transparency (e,e′p) experiment. The code was adapted to model Hall C and the HMS and SOS. The code was tested by comparing the simulated data to elastic (e,e′) and (e,e′p) data. After the data was verified it was then modified for (e,e′K^+) on hydrogen [30], [17] and deuterium[31], [32]. For this experiment SIMC was further modified to include (e,e′K^+) on carbon and aluminum targets.

4.1 Event Generation

The simulation begins by randomly generating the 4-vectors for the outgoing kaon and electron. The 4-vector for the target proton is needed in order to solve the kinematics. The momentum distribution of the proton in the carbon and aluminum targets were modeled as per figure 4.1 for carbon and figure 4.2 for aluminum. The Brueckner-Bethe-Goldstone (BBG) hole-line expansion was used to calculate the momentum distributions in the finite nuclei. The nucleons are assumed to occupy the single-particle orbits up to the Fermi level. The wave functions of the single-particle are taken from a harmonic oscillator. The length parameter are adjusted to fit the nuclear mean-square charge radius. The relative motion is dominated at short distances by the strong nucleon-nucleon repulsion and the wave function deviates sharply from the mean-field solution. This contribution replaces the wave function of a pair of nucleons in the Slater determinant by the multiscattered two-body wave function obtained from the Beth-Goldstone equation for finite nuclei.[33][34]

A random number is chosen and then the probability of the momentum is increased in step, until a value is found where the random number is greater than the probability of the momentum but less than one. P_{low} and P_{high} are calculated. P_{low} is the average between the chosen momentum value and the lower momentum value, equation(4.1). P_{high} is the average between the chosen momentum value and the higher momentum value, equation (4.2). The P_{fer} is given in equation (4.3), where $\mathcal{R}$ is a randomly generated number. The energy conservation was adjusted to included the recoil of the carbon residual and the aluminum residual and the respective hyperon.

$$P_{low} = \frac{P_{val-1} + P_{val}}{2} \tag{4.1}$$

$$P_{high} = \frac{P_{val} + P_{val+1}}{2} \tag{4.2}$$

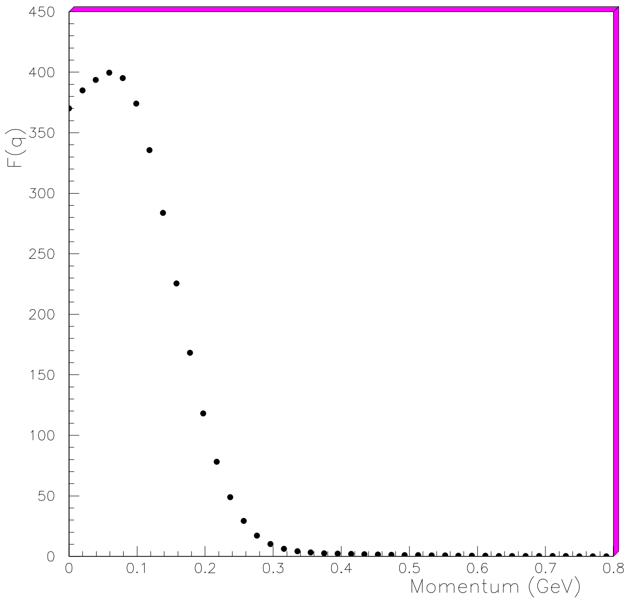

Figure 4.1: Momentum distribution for carbon.

$$P_{fer} = P_{low} + (P_{high} - P_{low}) * \mathcal{R} \tag{4.3}$$

The event fails at this point if the random choices of variables make the kinematics unsolvable. The event generator randomly chooses a target interaction point within the target length and raster amplitudes. The aluminum target is made of two aluminum targets, the events were randomly generated at these two target positions.

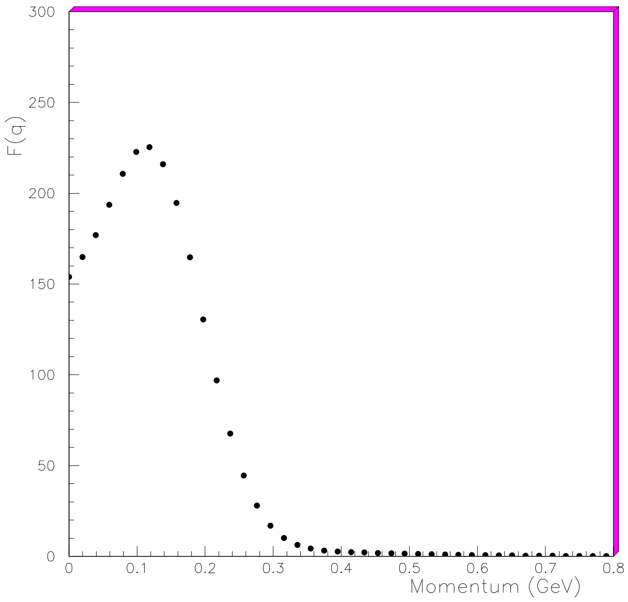

Figure 4.2: Momentum distribution for aluminum.

4.2 Spectrometer Simulation

The kaon and outgoing electron are then sent through the respective spectrometers. The particles are transported through the magnets to the detector huts by a set of matrix elements. The matrix elements are derived from the transport program, COSY Infinity [25]. The matrix elements are sequential for both the SOS and HMS. Multiple scattering is taken into account along the particles path in the simulation. The multiple scattering can occur anywhere along the particles path: at the vacuum windows, in air, on drift chamber wires, or in scintillator paddles. Once the particles make it through the required detector elements for a hardware trigger and particle ID the focal plane quantities are calculated, based on a smeared wire chamber position. The required detector elements for the SOS is the Čerenkov aerogel plane and the HMS requires the particle to make it to the third scintilator plane. The wire chamber position is smeared for each chamber plane for a realistic model of the chamber's resolution. The focal plane quantities are used to reconstruct the particle at the target. The reconstruction matrix elements are an inversion of the forward matrix elements used to transport the particle from the target to the focal plane.

4.3 Physics Model

Once both kaon and electron pass through the spectrometers apertures and the loose momentum and angle cuts, the event is assigned a physics cross section weight. The ratio of successes to attempts along with the initial five-dimensional generation volume gives the e-K coincidence acceptance of the spectrometers.

The cross section was obtain by parameterizing the binded hydrogen for the cross section dependence. This was done due to the poor agreement between data and theory, SL model [12]. The function is the sum of a constant and a resonance term as shown in equation (4.4) for hydrogen (e,e$'$K$^+$)Λ W-parameterizations.

$$\frac{A(1.65^2)(0.15^2)}{((W^2 - 1.65^2)^2 + (1.65^2)(0.15^2)) + B} \tag{4.4}$$

The same is done for Σ^o W-parameterization resulting in equation (4.5). A detailed description of the cross section parameterization can be found in [31]. Each event is then weighted by these parameterizations and the average value is computed.

$$\frac{A(1.90^2)(0.20^2)}{((W^2 - 1.90^2)^2 + (1.90^2)(0.20^2)) + B} \tag{4.5}$$

The invariant quantities Q^2, s , and t are determined for the event. The cross section in the center-of-mass system of the virtual photon and target nucleon $\frac{d\sigma}{d\Omega_K^*}$ for each event is calculated as a function of the invariant mass W. Through a Jacobian, $\mathcal{J}$ and the virtual photon flux Γ, we are then able to calculate the five-fold differential cross section in equation (4.6).

$$\frac{d\sigma}{dE_e d\Omega_e d\Omega_p} = \mathcal{J}\Gamma \frac{d\sigma}{d\Omega_p^*} \tag{4.6}$$

The cross section weight is multiplied by the probability that the kaon did not decay before the aerogel detector, located 9.8 m from the target. The correction factor for decay is calculated by evaluating the path length of the kaon through the SOS from the target to the aerogel. The path of the kaon is evaluated at discrete steps. The probability of decay over the steps is calculated and when the random number is less than this probability the kaon is considered decayed. Table 3.2 list the modes of decay for kaons. While the kaons is allowed to decay into the various decay products, SIMC does not track these particles.

The simulation yield is calculated by including target normalization and Monte Carlo weights which include, radiative correction, decay, spectrometer acceptance, and model cross section. The cross section is extracted from the data by multiplying the average cross section from the simulation by a scaling factor $\mathcal{F}$ needed to match the simulation to data.

4.4 Radiative Corrections

SIMC includes radiative corrections for the incoming and outgoing electron and also the produced hadron. The radiative code is similar to the original version of the simulation code.[29] [35] The radiative correction for A(e,e$'$ K$^+$)Y is based on the calculation of (e,e$'$p*), where p* is an off shell "proton". The off shell proton in this case is a kaon. The contribution to the radiative corrections from the outgoing hadron should be small and the p* approximation is fine. The contributions to radiative corrections, both hard and soft; internal and Bremsstrahlung; external are calculated. The relative probability for the particle to radiate in each arm, HMS and SOS, is calculated and the radiated photon is assigned to that particular arm. The initial range of outgoing electron momenta is large enough to include events which would radiate into the acceptances. The direction of the radiated photon is fixed to be in the same direction of the particle from which it radiates. When the incoming electron radiated the physics for that event is recalculated. When the final particles radiate only the 4-vector for the particle is modified. The radiation weight is combined with the physics cross section weight.

Nucleus	Z	V_c^{old}	V_c^{new}	$\frac{V_c^{new}}{V_c^{old}}$
		(MeV)	(MeV)	
Hydrogen	1	-	0.877	-
Deuterium	1	-	0.828	-
Carbon	6	3.198	3.840	1.2008
Aluminum	13	5.858	7.002	1.1953

Table 4.1: Coulomb potential comparison.

4.5 Coulomb Potential

The Coulomb potential was not important until the advent of the heavier targets (i.e. carbon and aluminum). The code was changed to include a new calculation of the Coulomb potential based on the work of Traini and Orlandini. [36] The potential calculation was changed from equation (4.7) to equation (4.8).

$$V_c = \frac{6}{5}\alpha(Z-1)\frac{\hbar c}{1.18A^{\frac{1}{3}}} \tag{4.7}$$

$$V_c = \frac{3}{2}\alpha Z R \hbar c \tag{4.8}$$

$$R = 1.12A^{\frac{1}{3}}\sqrt{1+3.84A^{-\frac{2}{3}}} \tag{4.9}$$

The comparison of the two calculation can be seen in the table 4.1. [37]

4.5.0.1 Carbon SIMC

The carbon data are corrected by an overall correction factor, Table 3.5, which corrects for efficiencies, absorption. The SIMC data are normalized to the same charge as the experimental data. The focal plane quantities for the carbon target are compared as a check for the SIMC code. Figure 4.3 and figure 4.4 show the agreement between SIMC (dash lines) and data (solid line). The SIMC data for Λ production are scaled, using a two-parameter χ^2 fit, between the Λ quasifree threshold, 11.37 GeV, and Σ^o quasifree threshold, 11.447 GeV. This is to ensure that only Λ are included in the scaling of the Λ for SIMC. Figure 4.5 shows the quasifree Λ distribution from the Monte Carlo code overlayed on the quasifree total hyperon production on carbon. The scaling factor, $\mathcal{F}$, is the amount the simulation must be adjusted to fit the data. The cross section for each target is extracted from the data by multiplying the average cross section from the Monte Carlo simulation by this scaling factor.

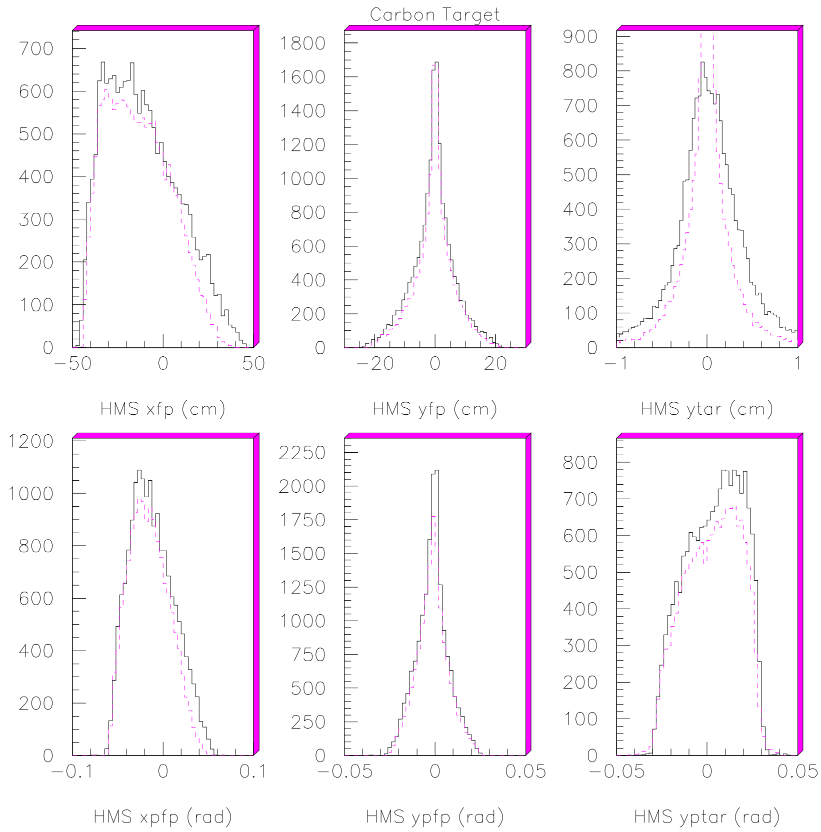

Figure 4.3: Data (solid line) to simulation (dash line) comparison for HMS. Data contains all hyperon contribution (Λ, Σ^o, and Σ^-). SIMC contains only Λ productions.

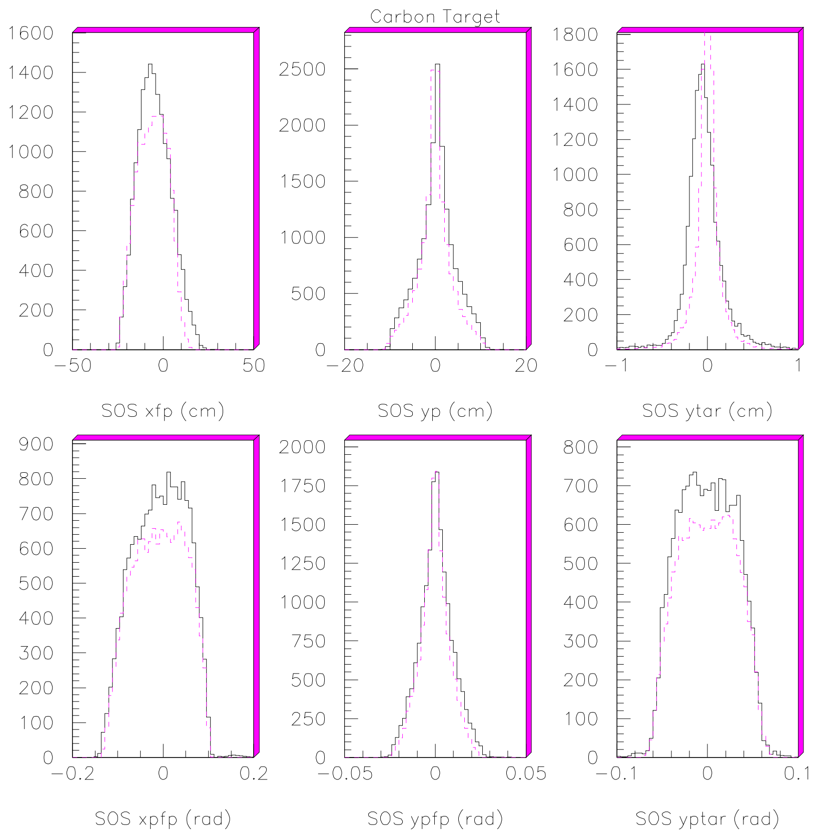

Figure 4.4: Data (solid line) to simulation (dash line) comparison for SOS. Data contains all hyperon contribution (Λ, Σ^o, and Σ^-). SIMC contains only Λ productions.

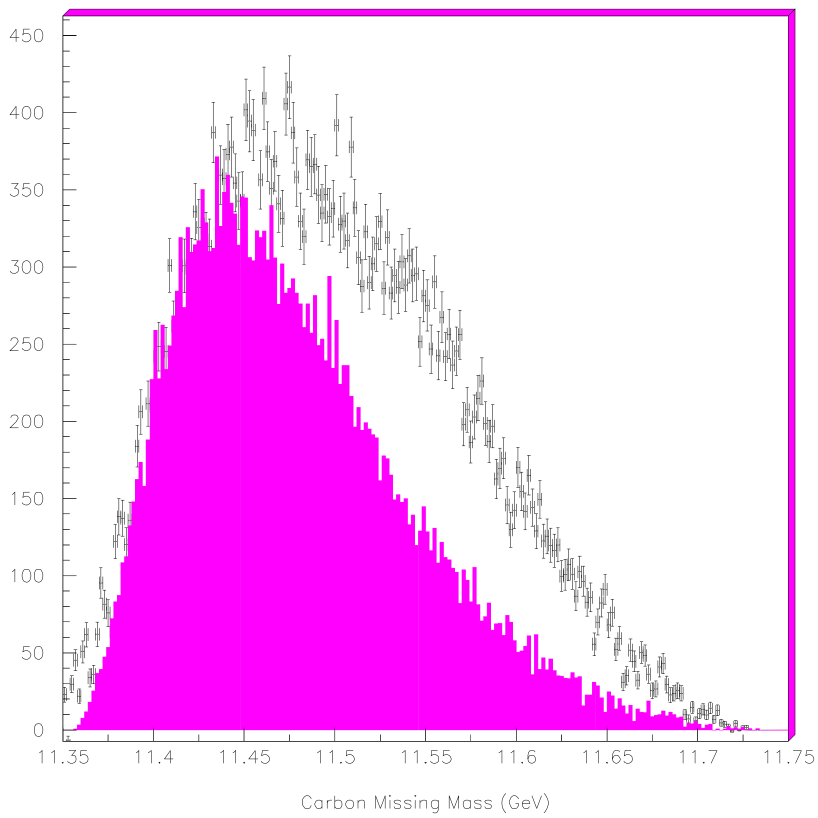

Figure 4.5: Carbon missing mass plot. The shaded region is the SIMC quasifree Λ distribution.

4.5.0.2 Aluminum SIMC

The SIMC for the aluminum target is similar to that for carbon. The differences are in the the generation of the target position, aluminum is made up of two targets, the mass of the recoil nucleus, conservation of energy and the fermi momentum distribution. Figure 4.6 is the comparison of the aluminum data (solid line) and SIMC data (dash line) of the y target for both spectrometers. The SIMC data for Λ production are scaled between the Λ quasifree threshold, 25.318 GeV, and Σ^o quasifree threshold, 25.397 GeV.

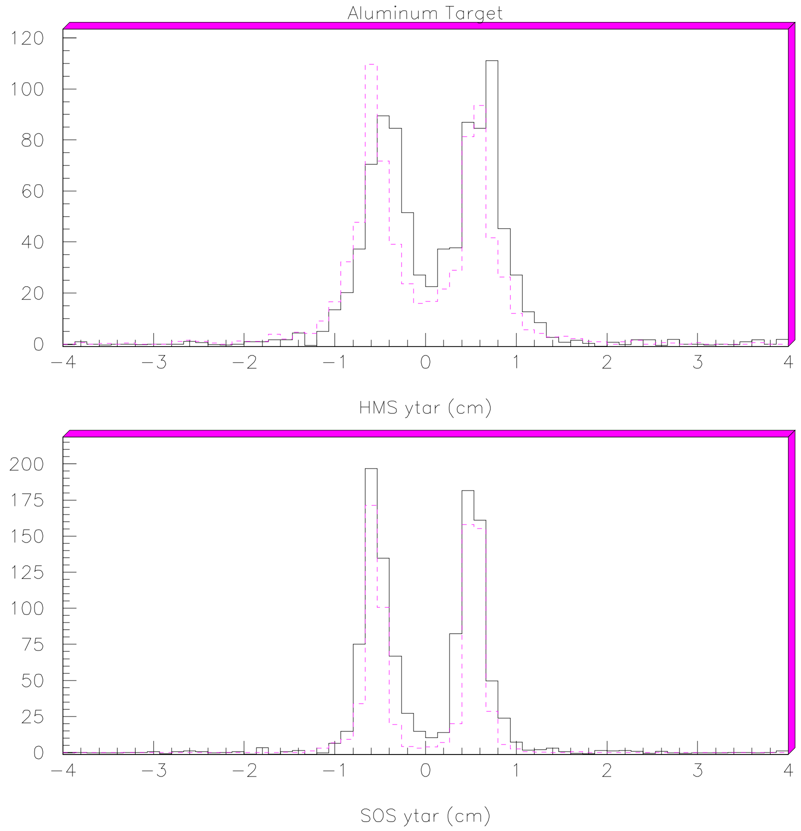

Figure 4.6: Data (solid line) to simulation (dash line) comparison for HMS and SOS target. Data contains all hyperon production contribution. SIMC only contains Λ contributions.

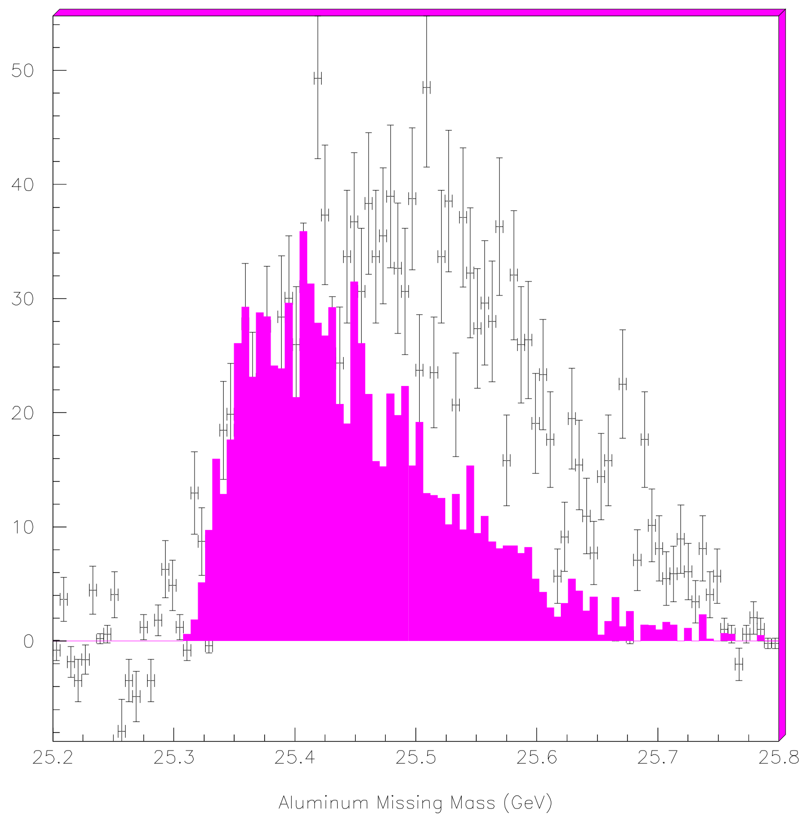

Figure 4.7: Aluminum missing mass plot. The shaded region is the SIMC quasifree Λ distribution.

CHAPTER 5

RESULTS AND DISCUSSIONS

5.1 Missing Mass

The bound and quasifree hyperon (Λ,Σ) regions of the ^{12}C(e,e$'$ K$^+$)YX reaction were both well within the acceptances of the spectrometers. The shaded regions in figures 5.1 and 5.2 are the random coincidence kaons and the unshaded regions are the 'reals' plus randoms coincidence events. The reconstructed missing mass for this process was calculated using equation (5.1).

$$M_x^2 = (\vec{q} - \vec{P}_k)^2 - (\omega + M_T - E_k)^2 \;\equiv\; missing\;\; mass^2 \tag{5.1}$$

The missing mass for the first data set of carbon (carbon I) is shown in figure 5.1. This represents a total of 14 hours of beam on target at a current of 35 μA ($\mathcal{L} = 1.88 \times 10^{41}$ cm^{-2}s^{-1}) corresponding to a total of 25,000 'true' kaon events. The second data set (carbon II) is shown in figure 5.2. It is from a total of 18 hours of beam on target at a current of 20 μA ($\mathcal{L} = 1.70 \times 10^{41}$ cm^{-2}s^{-1}) for a total of 36,000 'true' kaon events. A lower current setting for carbon II results in a better signal to noise ratio. The random events are proportional to the square of the incident beam current (I^2). The lucite Čerenkov was studied during the first carbon running and was consistently used as part of the trigger during the second data set, and also the aerogel Čerenkov threshold was lowered. These improvements to the trigger improved the signal to noise ratio and thus favored the recording of more good events.

The two carbon running periods have slightly different kinematic settings as seen in Table 1.1. These kinematic differences have a 3% variation in $\frac{d\sigma}{d\Omega}$. To increase the statistics of the distributions we have added the two sets together.

Data from the aluminum target are available for all the settings of hydrogen and deuterium, as shown in table 1.2 and 1.3. Only $Q^2 = 0.40$ and 0.50 $(GeV/c)^2$ are used in the analysis of Λ quasifree production. Figure 5.3 is a plot of the HMS momentum versus the SOS momentum. The x's represent the available kinematic settings for Λ threshold production. The boxes show the spectrometer settings for the aluminum data. The majority of the settings do not have adequate coverage of the threshold production within the spectrometer settings. The threshold raise is important in determining the effective nucleon number from Λ production. The Λ's which are found in the acceptance only represent the tail of the quasifree Λ production. Figure 5.4 is the missing mass plot of the quasifree production of hyperons for the $^{27}Al(e,e'\ K^+)YX$ reaction for $Q^2 = 0.4(GeV/c)^2$. The shaded region is the random kaons and the unshaded region is the 'real' coincidence events. Figures 5.5 and 5.6 are the remaining events from the aluminum targets at the Q^2 settings of 0.5, 0.75, 1.0, and 1.25 where the random events have been subtracted.

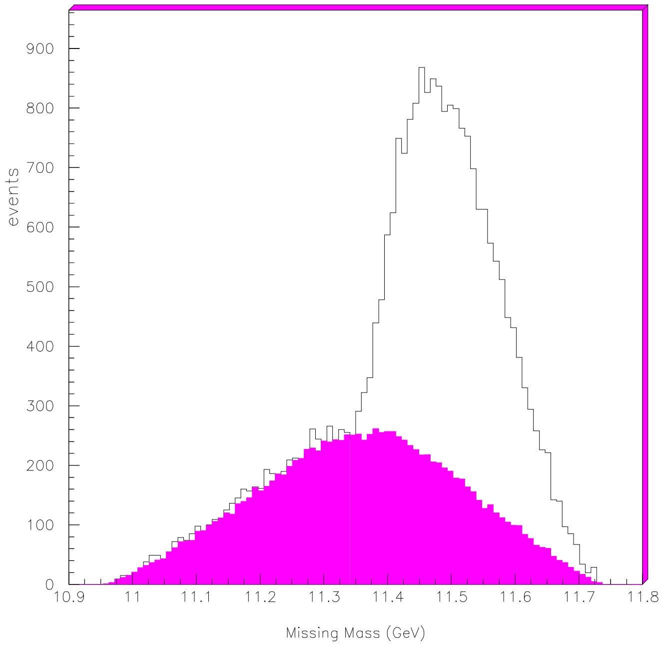

Figure 5.1: Quasifree production on carbon for the first data set (carbon I) at $Q^2 = 0.394$ (GeV/c)^2.

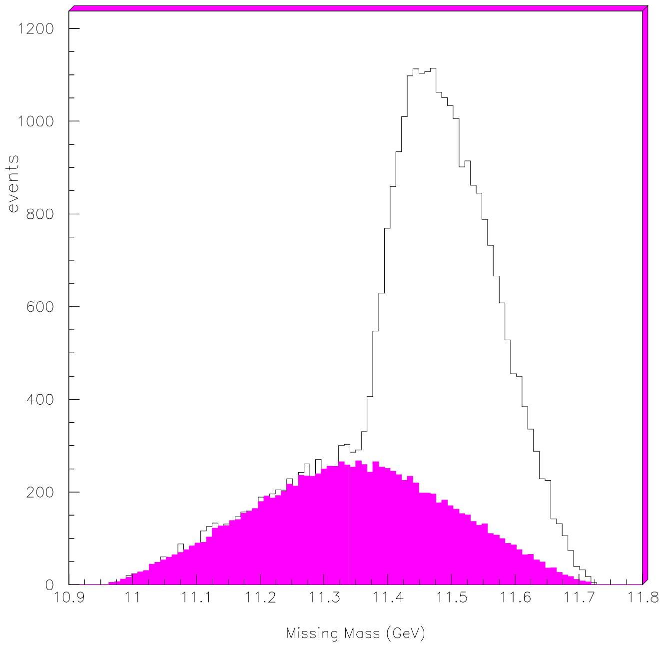

Figure 5.2: Quasifree production on carbon for the second data set (carbon II) at $Q^2 = 0.353$ (GeV/c)^2.

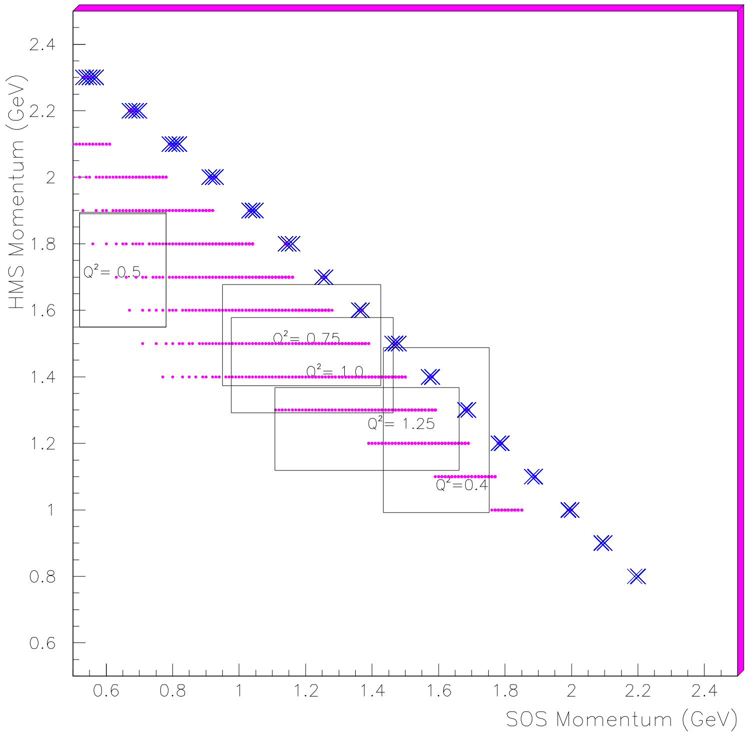

Figure 5.3: HMS momentum (GeV) versus SOS momentum (GeV). Xs represent the Λ production threshold on aluminum of all available kinematic settings. Whereas the dots represent Λ production threshold on hydrogen for all available kinematic settings.The boxes represent the SOS and HMS momentum coverage for the various spectrometer settings for the aluminum data.

These settings were not optimized for quasifree Λ production but were originally used to study the background contribution to the cryotargets from the aluminum walls of the cells.

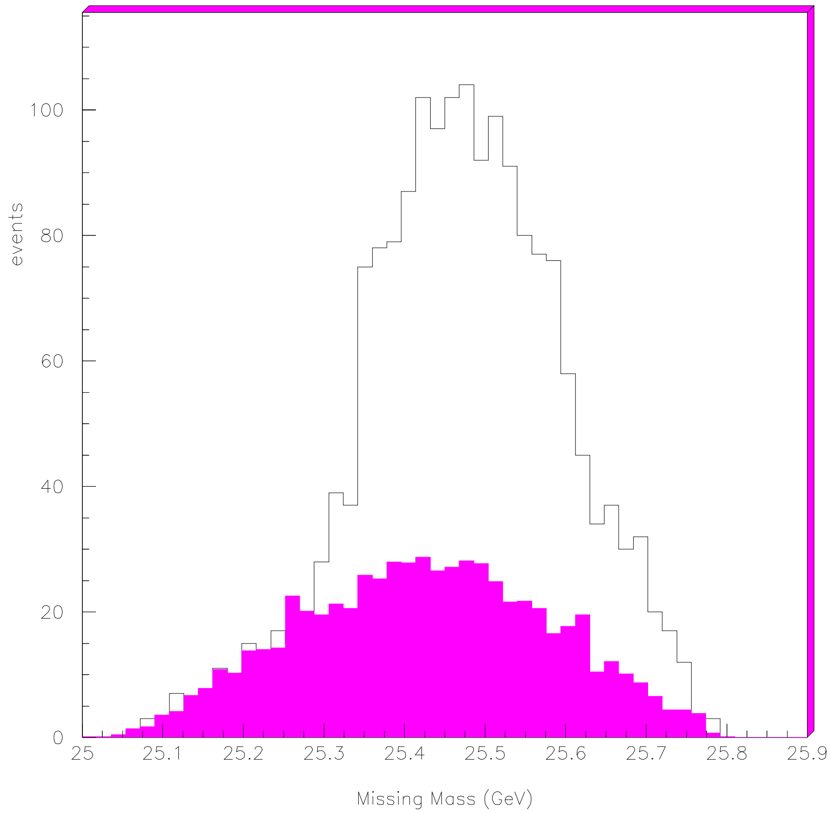

Figure 5.4: Quasifree hyperon production on aluminum at $Q^2 = 0.376\ (GeV/c)^2$

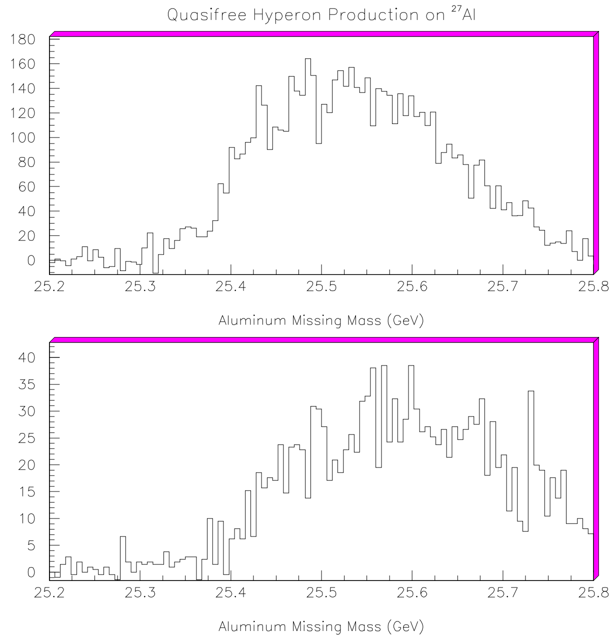

Figure 5.5: Quasifree hyperon production on aluminum. Q^2= 0.5 (GeV/c)^2, (top plot) and Q^2= 0.75 (GeV/c)^2,(bottom plot).

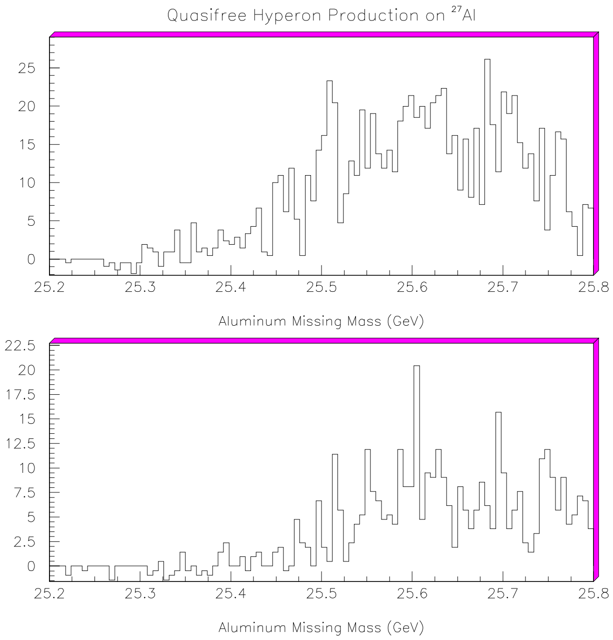

Figure 5.6: Quasifree hyperon production on aluminum. Q^2= 1.0 (GeV/c)^2, (top plot) and Q^2= 1.25 (GeV/c)^2, (bottom plot).

5.2 Simulation Comparison

5.2.1 Λ comparison

The elementary reaction p(e,e$'$ K$^+$)Λ(Σ^0), figure 5.7, shows the clear separation of the Λ and Σ^0 hyperons. When we move to ^{2}H nucleus the fermi motion of the nucleons begin to broaden the Λ and Σ^0 peaks. The addition of the neutron adds the Σ^- hyperon which contributes to the second peak in figure 5.8. The Λ, Σ^0 and Σ^- peaks in carbon and aluminum are smeared, due to the fermi motion of the nucleons, that one is unable to distinguish between the Λ and Σ peaks.

The average cross section for the carbon and aluminum quasifree production was extracted using the model cross section obtained from the individual simulation codes for Λ, Σ^o, and Σ^-. The simulation data were fitted to the experimental data for Λ production from 11.371 GeV (Λ threshold) to 11.447 GeV (Σ^o threshold) in missing mass. The procedure for aluminum was similar, but the data were fitted from a range between 25.319 (Λ threshold) and 25.395 (Σ^o threshold). Figures 5.9 and 5.10, carbon I and carbon II respectively are data (error bars) with the simulation overlaid (solid lines). Figure 5.11 is the aluminum where we also compare data (error bars) and simulation data (solid line).

The production thresholds for Λ, Σ^o, and Σ^- are marked on all plots. The region between the Λ and Σ^o threshold was chosen to fit the simulation, to insure that only quasifree Λ's were included in the fit. The simulation was fit using a χ^2 fitting routine where the coefficient is the scaling factor $\mathcal{F}$ which represents the

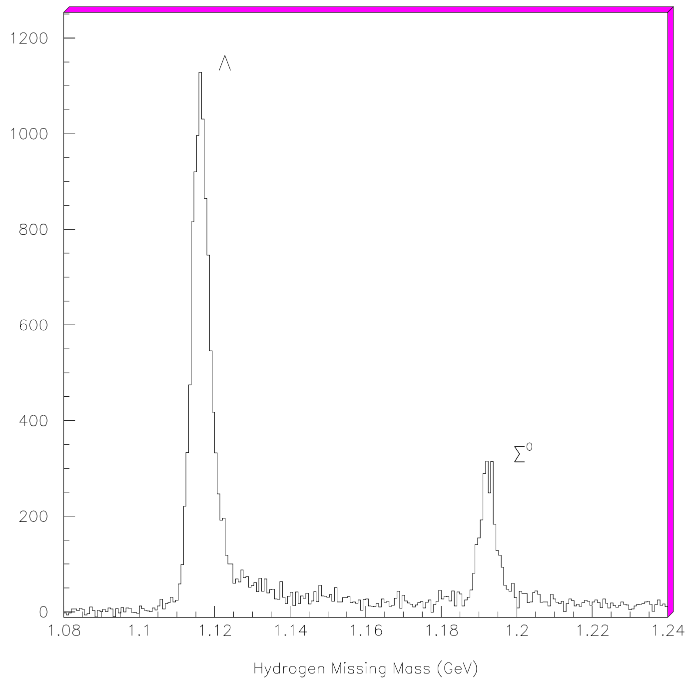

Figure 5.7: Missing mass plot of hyperon production on hydrogen Q^2=0.4 $(GeV/c)^2$.

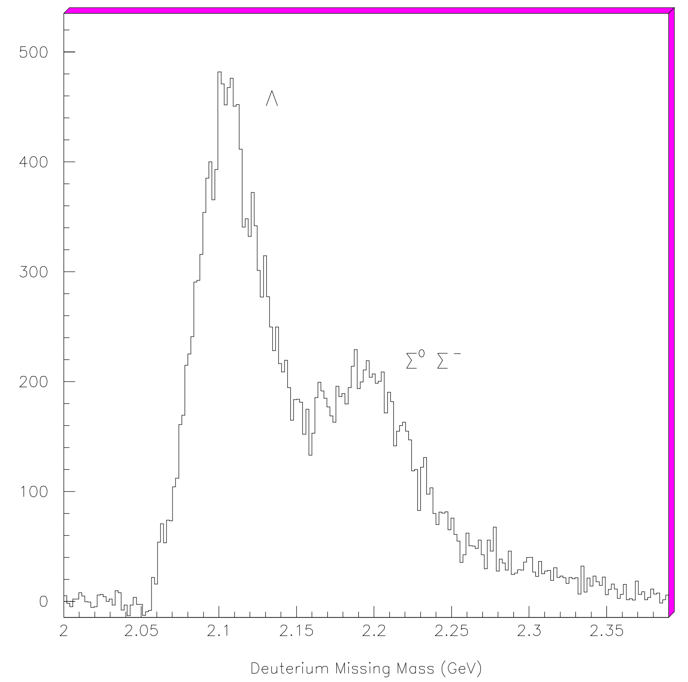

Figure 5.8: Quasifree Λ, Σ^o and Σ^- production on deuterium $Q^2 = 0.4$ $(GeV/c)^2$.

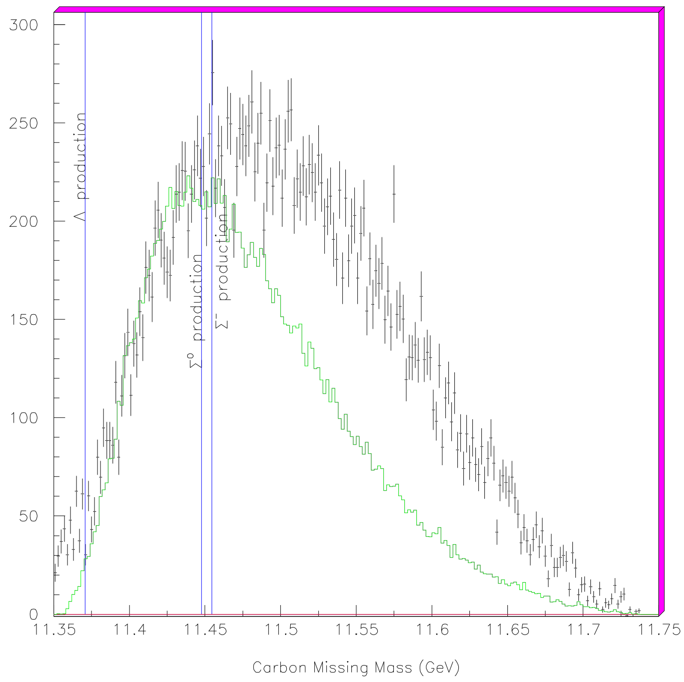

Figure 5.9: Quasifree Λ production on carbon first running (error bars) with simulation overlayed (solid line) for Q^2=0.393 (GeV/c)^2.

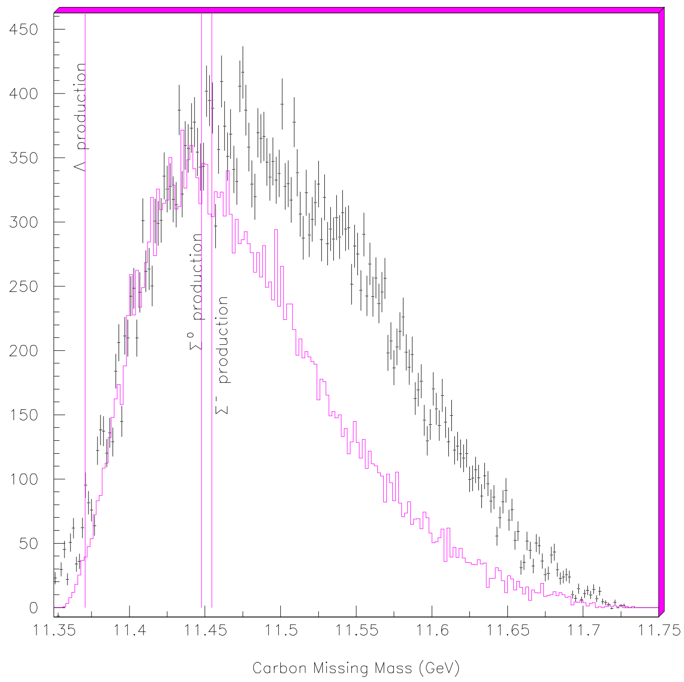

Figure 5.10: Quasifree Λ production on carbon second running (error bars) with simulation overlayed (solid line)for Q^2 = 0.353 (GeV/c)^2.

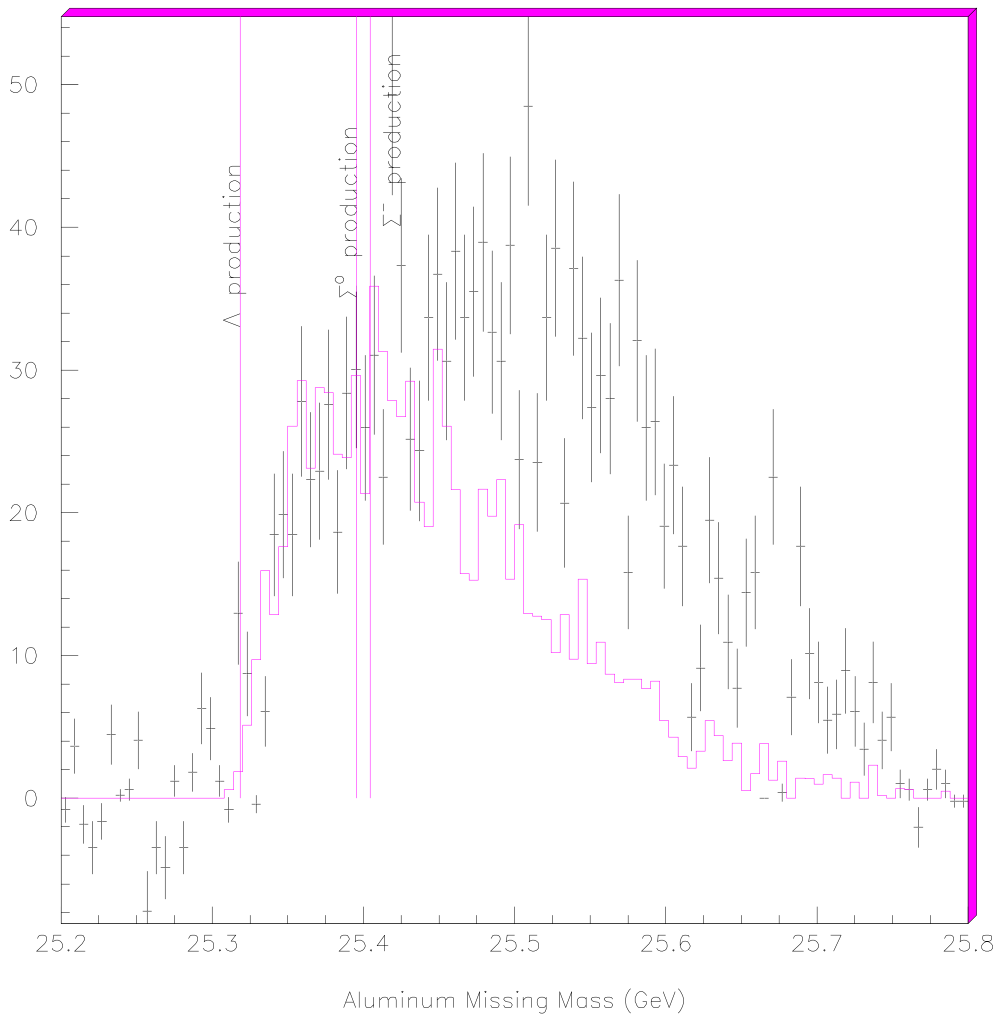

Figure 5.11: Quasifree Λ production on aluminum (error bars) with simulation overlayed (solid line) for Q^2=0.376. The Monte Carlo only includes the Λ production. The data includes both Λ and Σ production.

Target	$\mathcal{F}_{\Lambda}$	$\mathcal{F}_{\Sigma^o}$	$\mathcal{F}_{\Sigma^-}$
Hydrogen	1.32 $\pm$ 0.02	1.38 $\pm$ 0.03	-
Deuterium	1.27 $\pm$ 0.04	1.34 $\pm$ 0.05	0.48 $\pm$ 0.02
Carbon	5.35 $\pm$ 0.27	5.64 $\pm$ 0.40	6.11 $\pm$ 0.55
Aluminum	10.03 $\pm$ 0.50	10.57 $\pm$ 1.06	15.79 $\pm$ 1.90

Table 5.1: Hyperon scaling factor, $\mathcal{F}$, per target at $Q^2 = 0.400$ (GeV/c)^2

amount the simulation data has to be adjusted to fit the experimental data. The scaling factors for Λ production are given in table 5.1 for all four targets. There is a $\pm$10% fitting error for carbon and aluminum. The average center of mass cross section was taken from the simulation code and the appropriate scaling factor was applied to determine the cross section for quasifree Λ production for each target, equation(5.2).

$$\left(\frac{d\sigma}{d\Omega}\right)_{data} = \left(\frac{d\bar{\sigma}}{d\Omega}\right)_{MC} \times \mathcal{F} \tag{5.2}$$

The cross section value for the elementary process, hydrogen, and nuclear targets, deuterium, carbon, and aluminum were then applied to equation(5.3) to calculate the effective proton number for Λ production. The number of protons which *effectively* participate in the production of the quasifree Λ hyperon is defined as

$$Z_{eff} = \frac{(\frac{d\sigma}{d\Omega})_{nucl}}{(\frac{d\sigma}{d\Omega})_{elem}} \tag{5.3}$$

Target	Effective Proton Number
Hydrogen	1.000 ±0.10
Deuterium	0.967±0.0967
Carbon I	4.170±0.417
Carbon II	3.900±0.390
Carbon (γ,K^+)	4.2±0.588 [3]
Aluminum	7.597±1.1396

Table 5.2: Effective proton number for Λ production

Figure 5.12 shows the effective proton number for the different targets. The hydrogen and deuterium data are from Exp. 93-18 and Exp. 91-16. Included in this plot is the photoproduction data on carbon from [3] which is in agreement with the electroproduction $Q^2 = 0.4$ $(GeV/c)^2$ carbon data. The fit to the data points is a power fit Z^α, where $\alpha = 0.793 \pm 0.043$.

Table 5.2 list the values of the effective protons for $Q^2 = 0.4$ $(GeV/c)^2$ for all four targets and the value from the photoproduction data.

5.2.2 Σ comparison

The Σ^- production from the neutron contribution of deuterium,[32] carbon, and aluminum is calculated assuming the Λ to Σ^o production ratio of the nuclear targets is the same as that of the free proton. Table 5.1 lists the scaling factors for Σ^- calculated for deuterium, carbon and aluminum, keeping the Λ to Σ^o ratio constant and the remaining strength contribution attributed to Σ^- production.

Figure 5.13 shows both Σ^o and Σ^- production on carbon II. The Σ^- cross section in carbon electroproduction is slightly higher than the Σ^o cross section.

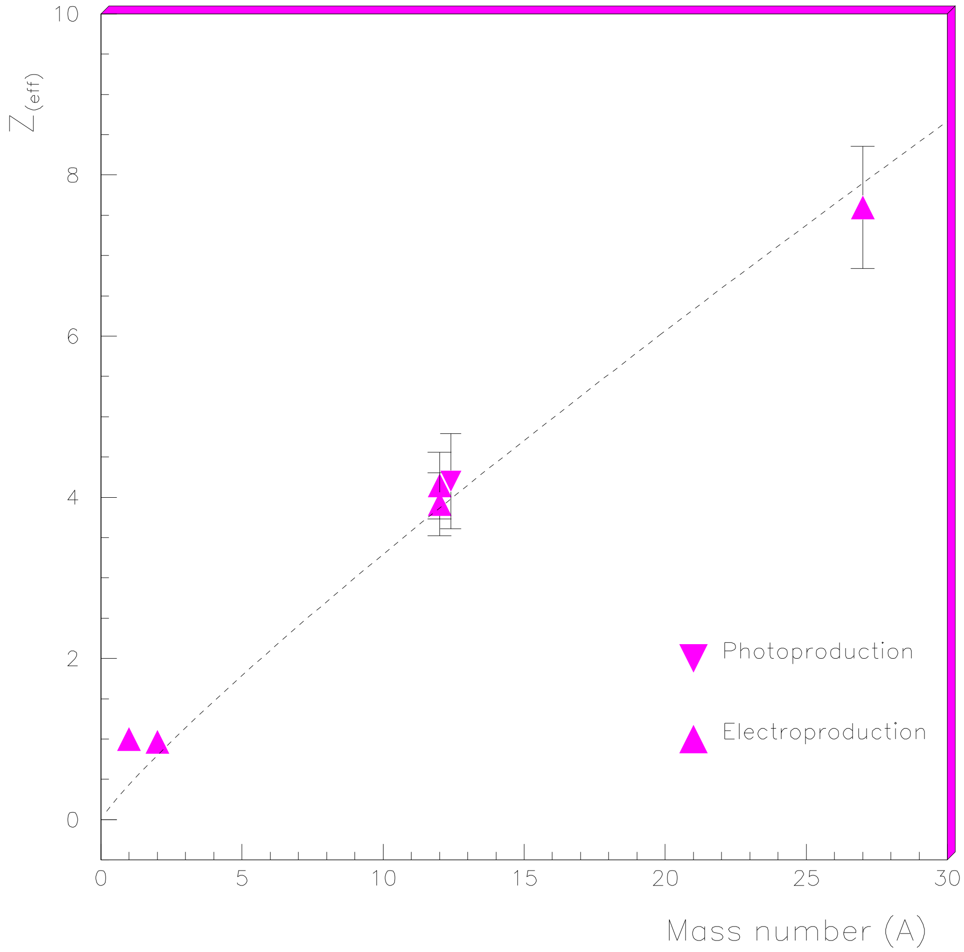

Figure 5.12: Effective nucleon number for Λ production at Q^2=0.4 (GeV/c)^2. The inverted triangle is the photoproduction data on carbon from [3].

Figure 5.14 shows both Σ^o and Σ^- production on aluminum. The cross section for Σ^- in aluminum electroproduction is also larger than the production cross section for Σ^o based on the assumption that the production ratio in the nuclear aluminum target is the same as the production ratio of a free proton in hydrogen. Using the cross section for both nuclear targets and the elementary neutron cross section from the deuterium analysis, we applied it to equation (5.4).

$$N_{eff} = \frac{(\frac{d\sigma}{d\Omega})_{nucl}}{(\frac{d\sigma}{d\Omega})_{elem}} \tag{5.4}$$

This will give the *effective* number of neutrons which take part in the production of quasifree Σ^- hyperon. According to these calculations effectively 12 neutrons in carbon and 29 neutrons in aluminum participate in the production of the Σ^-. There are only 6 neutrons available in carbon to interact with the virtual photon and only 14 neutrons in aluminum to interact with. Figure 5.15 is the plot of the overall Σ production plotted against the mass number. This gives an effective nucleon number (A_{eff}) for total Σ production. The dash line represents the results from the effective proton number. Figure 5.15 suggest that K^+-N interaction in Λ production is different from K^+-N interaction in $(\Sigma^0 + \Sigma^-)$ production.

Figure 5.16 shows the various production ratios compared to the elementary process of deuterium. The closed circles represents the Σ^o/Λ ratio which is calculated from the hydrogen production and assumed constant for the nuclear targets. The inverted triangles represent the sum of the Σ productions, Σ^o and Σ^-, to Λ.

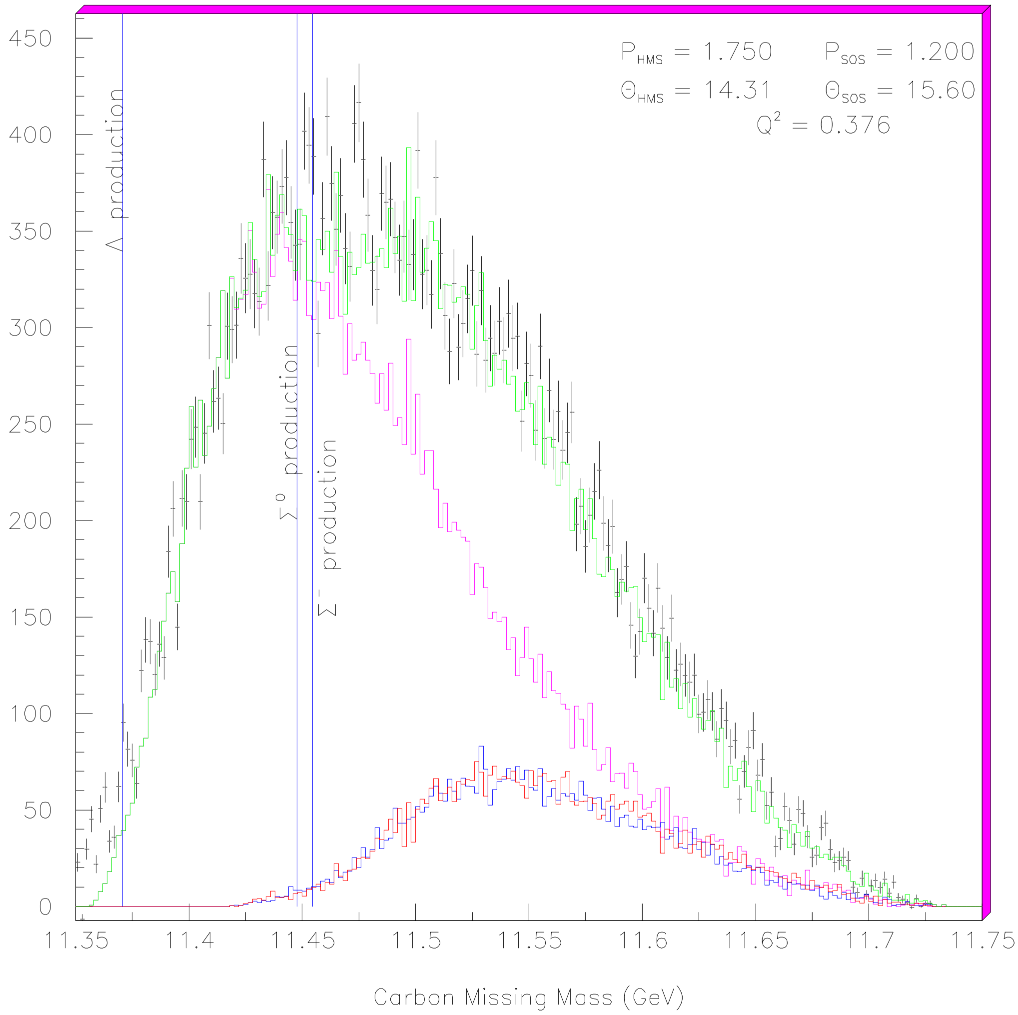

Figure 5.13: Quasifree production on carbon II with simulation overlayed for Λ, Σ^0 and Σ^-.

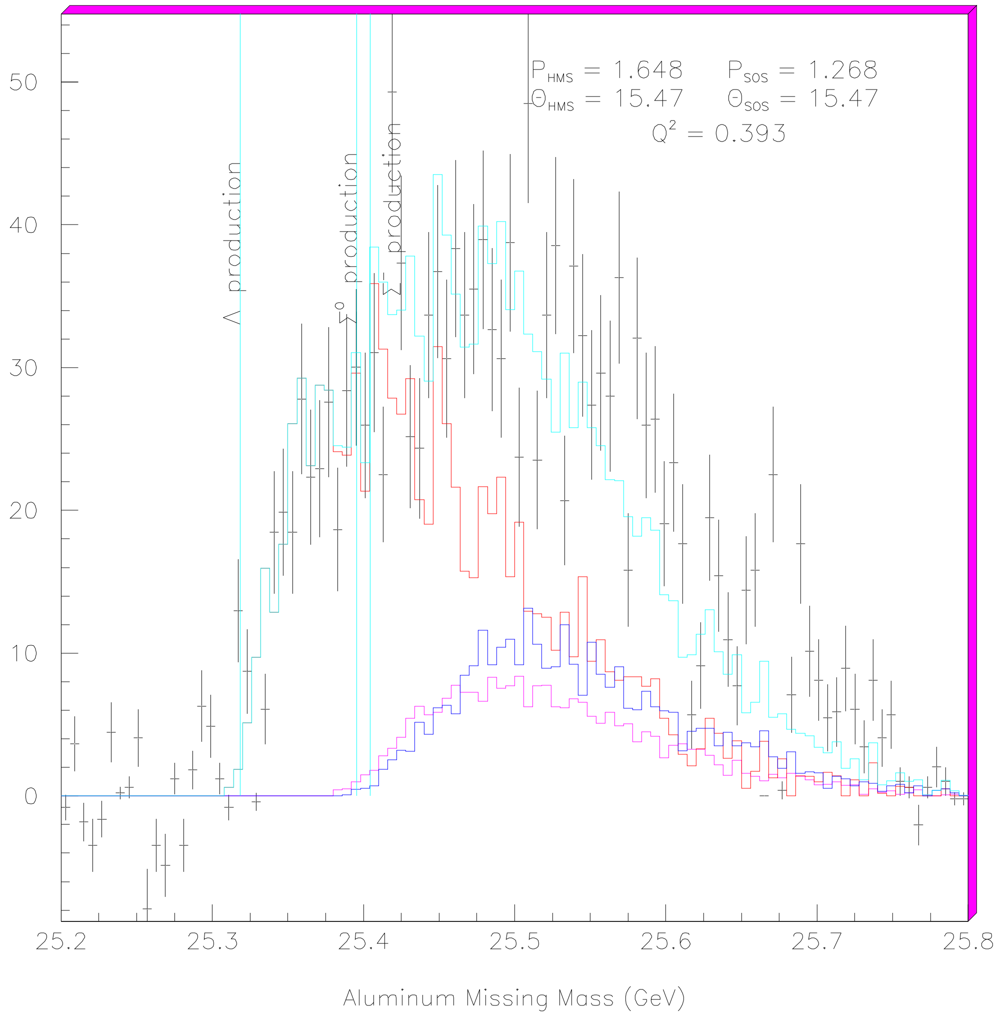

Figure 5.14: Quasifree hyperon production on aluminum with simulation overlay for Λ, Σ^0, and Σ^-

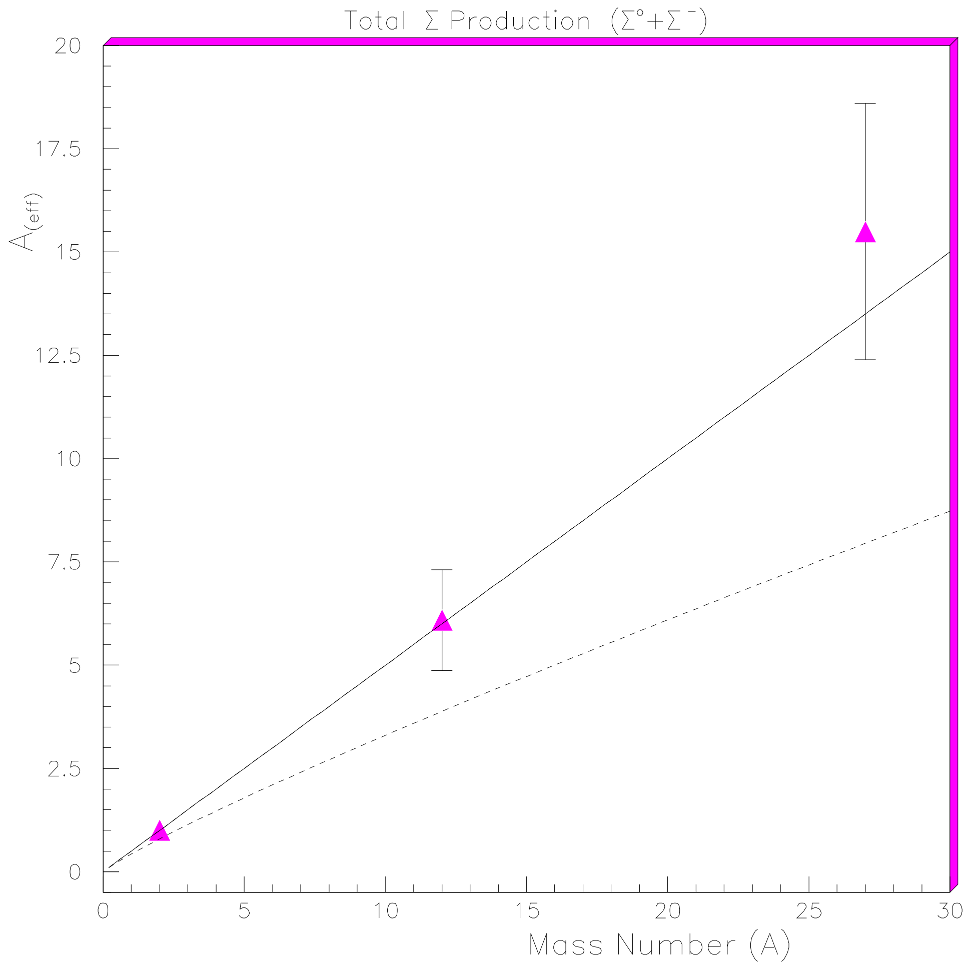

Figure 5.15: Effective nucleon number for the total Σ production. Normalized to deuterium Σ production. The dash line represent the fit from the effective proton number fit. Figure 5.12 The solid line is the $\mathrm{A}_{eff}=\frac{A}{2}$ fit.

This shows that the total Σ cross section is increasing for each target. The closed squares are the ratio of Σ^- to Σ^o which is also increasing as the atomic number increases.

The original assumption that the Λ to Σ^o ratio from a free proton is constant with increasing atomic number may not be a correct assumption. For example, it is surprising that N_{eff} could be larger than (A-Z) the actual neutron number. Another, perhaps less likely, possibility is that Σ^- production is enhanced in heavier nuclei. The data do not distinguish between these two above scenarios. However, the data do suggest in figure 5.16 the Σ production overall is enhanced.

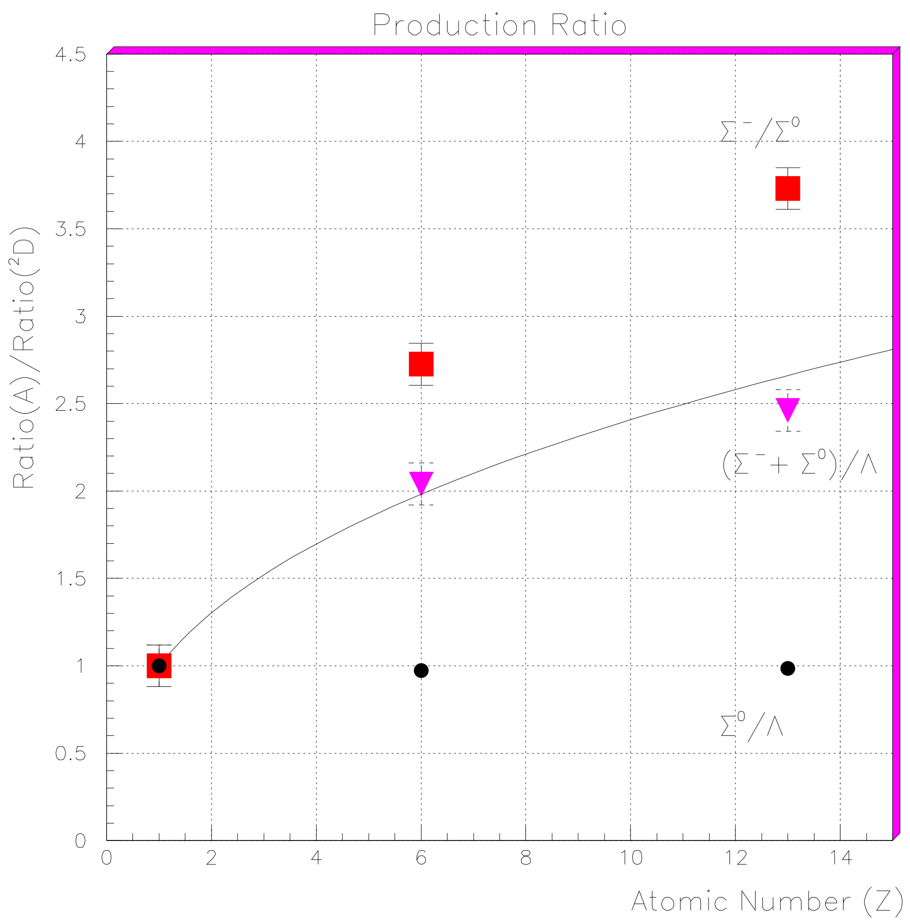

Figure 5.16: Ratios of Σ quasifree production normalized to deuterium (elementary process).

5.3 Escape Probability

The ability of the produced K meson to emerge from the nucleus without a collision with other nucleons in the nucleus is a measure of the escape probability of the K^+. It is expected that this probability will decrease as the nucleus size increases, providing a longer exit path and thus increased probability for scattering. The propagation is characterized in terms of the mean free path λ, which is the average distance between collisions.

$$\lambda = \frac{1}{\rho\sigma} \tag{5.5}$$

Where ρ is the nuclear density and σ is the scattering cross sections. The escape probability, T, was calculated using the following equations (5.6 - 5.8)

$$T = \frac{4\pi}{Z}\int_0^Z d^3\vec{r}'\rho_p(\vec{r}')P_T(\vec{r}') \tag{5.6}$$

$$P_T(\vec{r}') = e^{-\int_{z'}^{\infty} dz'\sigma} \tag{5.7}$$

$$\sigma = \frac{\sigma_{K^+n}\rho_n(r') + \sigma_{K^+p}\rho_p(r')}{Z} \tag{5.8}$$

The charge density distribution ρ(r) for each target is one of the functions: harmonic oscillator (HO), sum of Gaussian (SG), two-parameter Fermi (2pF) or three-parameter Gaussian (3pG). The functions and their parameters are given in detail

Target	Z	Effective Nucleon Number total	elastic	inelastic
Helium	2	1.02	1.451	1.408
Carbon	6	2.707	4.103	3.959
Oxygen	8	3.4488	5.3528	5.152
Calcium	20	5.994	11.274	10.662

Table 5.3: Effective nucleon (proton) number, based on total, elastic and inelastic 1 GeV K^+ scattering.

in [38]. P_T is the probability of the kaon at $\vec{r}'$ to escape without final-state interactions. σ_{Kn} and σ_{Kp} are the kaon-neutron and kaon-proton scattering cross section. The effective nucleon is defined from the Glaubar calculation by the following equation (5.9)

$$Z_{eff} \ = \ T * Z \tag{5.9}$$

The escape probability was calculated for total, elastic and inelastic KN scattering. Table 5.3 lists the effective proton number for the four targets calculated. Figure 5.17 is the plot of the calculated effective proton number for the total, elastic and inelastic scattering. The dash line represents the functional fit, Z_{eff}=0.431*$A^{0.884}$, for the experimental data. There is a good agreement between the experimental results and the calculation.

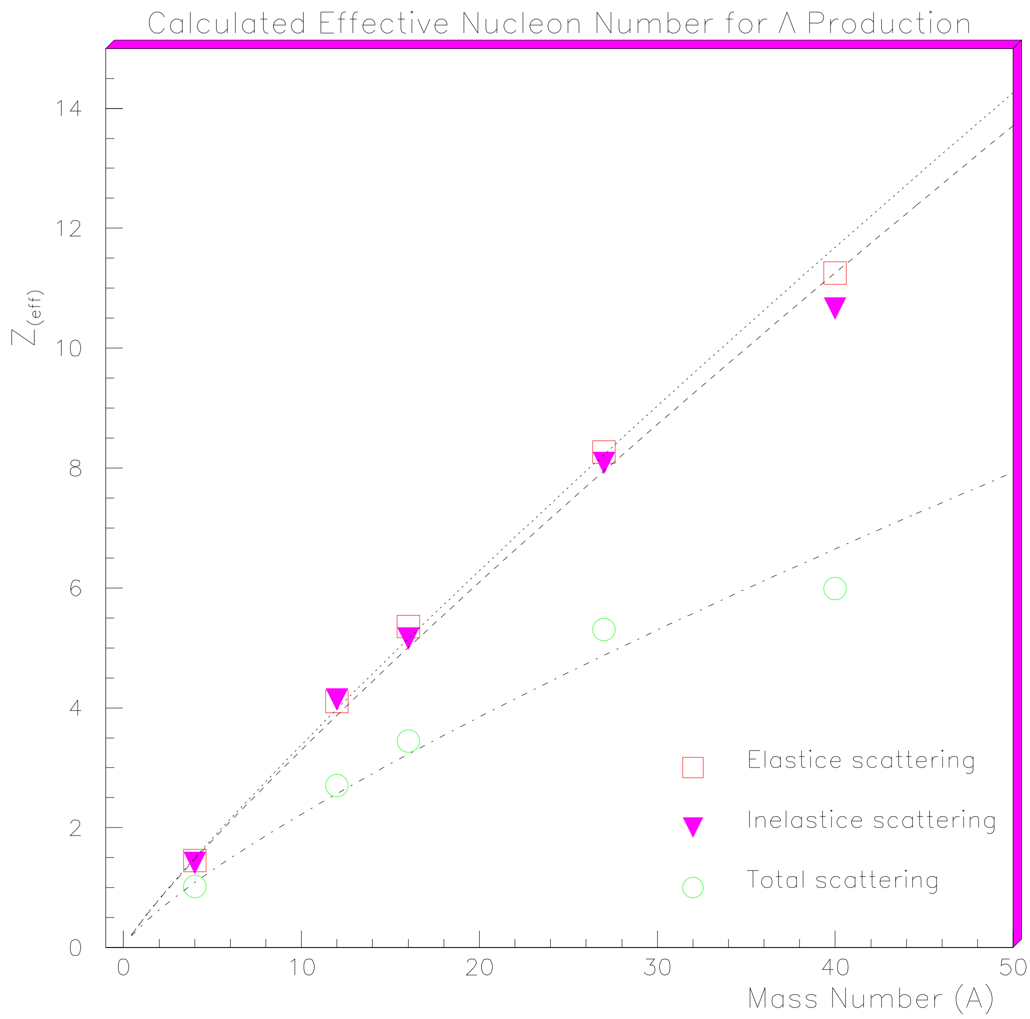

Figure 5.17: Effective proton number calculated for various targets. The dash line passing near the inverted triangles represents the A^{α} fit to the experimental data.

5.4 Other Results

5.4.1 Bound Region

The motivation for this experiment was not to resolve the bound states of carbon hypernuclei. The kinematic setting was not optimized for hypernuclear production. The spectrometer angles are large, causing the cross section for bound states in carbon to be very small. The expected cross section for the ground state of carbon at these kinematic settings was extracted from [39] using figure 5.18 to be $\approx 10^{-35} cm^2/sr^2/GeV$. The bound region is the area below the Λ quasifree threshold. After summing both carbon runnings together, the total expected number of events in the ground state of carbon is 34 event for 32 hours of beam time. The energy drift then smears the resolution of these few events making a precise bound state peak difficult to determine. The statistical fluctuation of the randoms subtractions adds to the uncertainty in this region.

After the randoms backgrounds are subtracted and carbon I and carbon II are summed together, a remaining strength does show up below the quasifree threshold as seen in figure 5.19. The quasifree Λ production from the SIMC program is overlayed on the plot (dashed lines). The SIMC program only simulates the elementary process of hyperon production on a single nucleon. Final state and bound states models are not included in the simulation. Below 20 MeV in the binding energy, there are other strengths which occur at $\approx$100 MeV in binding energy, seen in figure 5.1 and 5.2. Currently no conclusion has been reached to

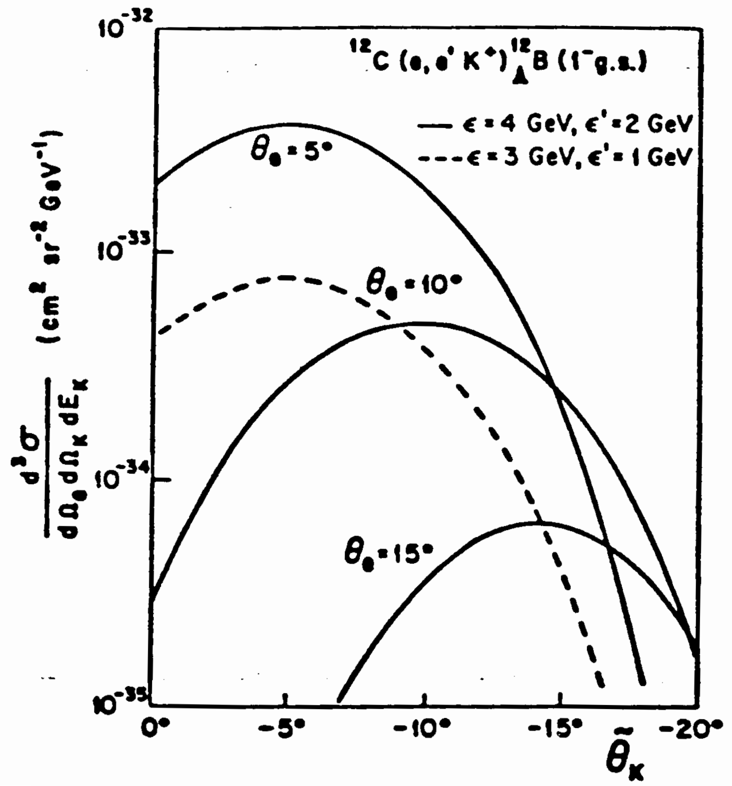

Figure 5.18: Multiple-differential cross section for^{12}C(e,e$'$K$^+$)$^{12}_{\Lambda}$B(1$^-$gs). From [39].

explain these peaks. These peaks are seen in both carbon I and carbon II.

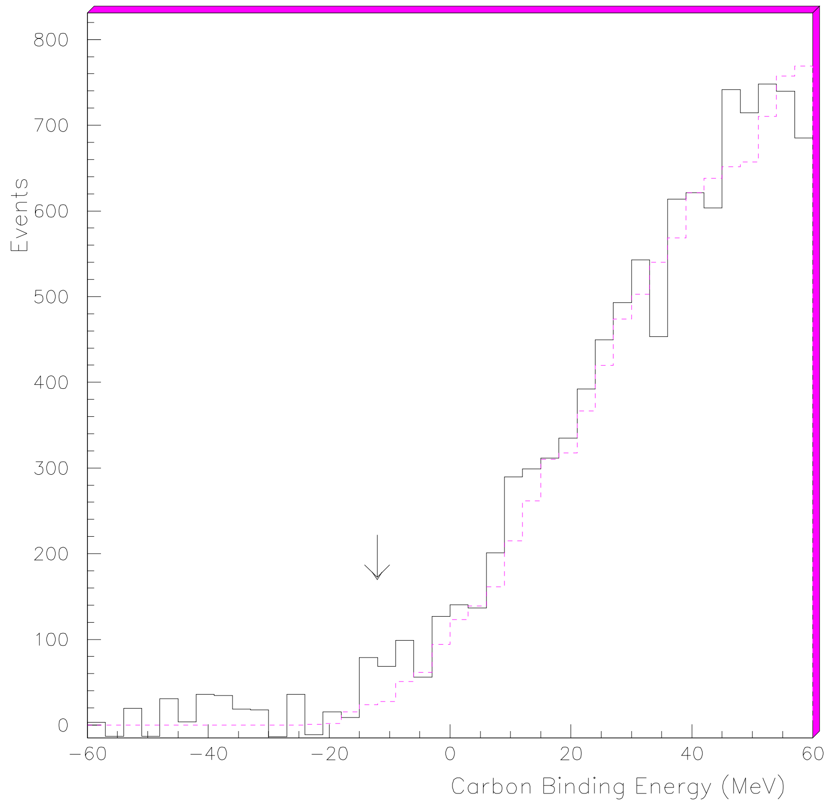

Figure 5.19: Bound Region of ^{12}C. The solid lines represent the sum of carbon I and carbon II. The dash line is the SIMC data.

CHAPTER 6

CONCLUSION

The first study of (e, e$'$ K$^+$) on carbon and aluminum was performed at Thomas Jefferson National Accelerator Facility. Carbon and aluminum quasifree electroproduction of hyperons was study at the Q^2 value of 0.40 (GeV/c)^2. The scattered electron and electroproduced kaon were cleanly detected in coincidence in the HMS and SOS spectrometers. The missing mass distribution of hydrogen and deuterium were also studied as a comparison to the heavier targets. The Λ and Σ^o missing mass peaks from hydrogen are sharp peaks which can be cleanly separated. Deuterium's missing mass distribution begins to show the effects of the fermi motion of the proton and neutron by broadening the Λ and Σ^0 peaks. The addition of the neutron permits the production of a Σ^- hyperon in deuterium. The internal motion of the individual nucleons inside carbon and aluminum cause the Λ and Σs peaks to be indistinguishable.

The A-dependences of the effective nucleon number was obtained, this is the participating proton number in the reaction process. The effective proton number from Λ production on carbon was determined to be 4.17 $\pm$ 0.42. The effective proton number for aluminum was determined to be 7.60 $\pm$ 1.14. The cross section data were fit to a power law ($\approx$ A$^\alpha$) with α = 0.88 $\pm$ 0.10, consistent with the

K^+'s relatively long nuclear mean free path. The attempt to separate the Σ^0 and Σ^-in carbon and aluminum using the assumption that scattering from a free proton scales to that of a nuclear target fails. This assumption extracts an effective neutron number which is larger than (A-Z) the actual number of neutrons in the target. Figure 5.15 suggest that K^+-N interaction in Λ production is different from K^+-N interaction in $(\Sigma^0 + \Sigma^-)$ production. The overall $\frac{\Sigma^0+\Sigma^-}{\Lambda}$ ratio cross section seems to be enhanced in heavier nuclei.

A feasibility test for hypernuclear spectroscopy on ^{12}C and ^{27}Al with the HMS-SOS was performed. The use of the lucite Čerenkov detector in the SOS trigger aided in decreasing the amount of background events written to tape. The PID techniques used to remove the background events were successful for the heavier target and can be used to extract the coincidence K^+ event in the hypernuclear studies. The quasifree contribution, which is background events for hypernuclear spectroscopy, can now be scaled as a function of A. The lower current setting for carbon II resulted in a better signal to noise ratio. The random events are proportional to the square of the incident beam current (I^2). Therefore, for a manageable random rates the high current runs should be avoided. Bound states were not the focus of this experiment but are certainly achievable with the Hall C detector equipment and the continuous electron beam at Jefferson Lab.

BIBLIOGRAPHY

[1] M. Danysz and J. Pniewski. *Philos. Mag.*, 44:348, December 1953.

[2] B.F Gibson and E.V. Hungerford. *Physics Report*, 257:349, 1995.

[3] H. Yamazaki and et. al. *Physical Review C*, 52(3):R1157, September 1995.

[4] C. Milner and et.al. *Physical Review Letter*, 54(12):1237, 1985.

[5] S. Ajimura and et.al. *Nuclear Physics*, A(577):271, 1994.

[6] M. Sotona and S. Frullani. *Progress of Theoretical Physics Supplement*, 1(117):151, 1994.

[7] C.B. Dover and D.J. Millener. *Electroproduction of Strangeness*, chapter 3. World Scientific, 1991.

[8] M. Sotona and et al. *Nuclear Physics*, A547:63c, 1992.

[9] D. Abbott and et.al. *Physical Review Letters*, 80(23):5072, June 1998.

[10] S. Hoibraten J. Ouyang and R.J. Peterson. *Physical Review C*, 47(6):2809, June 1993.

[11] T. Kishimoto. *Nuclear Physics*, A(450):447, 1986.

[12] J. C. David, C. Fayard, G. H. Lamot, and B. Saghai. *Physical Review C*, 53(6):2613, June 1996.

[13] C.J. Bebek and et.al. *Physics Review D*, 15(3):594, February 1977.

[14] P. Brauel and et.al. *Z. Physics*, C(3):101, 1979.

[15] SAPHIR collaboration. *Physic Letter*, B(445):20, 1990.

[16] W. Cummings. *The SOS Handbook (unpublished)*. Newport News, VA, 1.1 edition.

[17] Richard Mohring. PhD thesis, University of Maryland, College Park (unpublished), 1999.

[18] Liguang Tang. Private communication.

[19] J.V. Jelley. *Cherenkov Radiation and Its Applications*. Pergamon, London, 1958.

[20] C. Biino and et. al. *Nuclear Indtruments and Methods in Physics Research*, A(295):102–108, 1990.

[21] J. Litt and R. Meunier. *Annual Review of Nuclear Science*, 23:1, 1973.

[22] D.F.Geesaman and S. Wood. Hall c analysis software vade mecum. Technical report, Jefferson Lab Hall C Internal Report, 1994.

[23] CERN Application Software Group. *PAW- Physics analysis Workstation, The Complete Reference*. CERN Program Library Long Writeup Q121, version 2.03 edition, 1993.

[24] Derek Van Westrum. PhD thesis, University of Colorado (unpublished), 1998.

[25] M. Berz. *Nuclear Instrument and Method*, A(298):473, 1990.

[26] K. A. Assagaman, D. Dutta, and P. Welch. Hall c matrix element optimization package. Technical report, Jefferson Lab Hall C Internal Report, 1997.

[27] G. Niculescu. On pathlengths and corrected coincidence time. Technical report, Jefferson Lab Hall C Internal Report, 1997.

[28] Bernhard A. Mecking. In *Research Program at CEBAF Report of the 1985 Summer Study Group*, pages 7–25, Newport News, Va, January 1985. CEBAF, South Eastern Universities Research.

[29] N. C. R. Makins. PhD thesis, Massachusetts Institute of Technology (unpublished), 1994.

[30] Gabriel Niculescu. PhD thesis, Hampton University (unpublished), 1998.

[31] Douglas Koltenuk. PhD thesis, University of Pennsylvania (unpublished), 1999.

[32] Jinseok Cha. PhD thesis, Hampton University (unpublished), 2000.

[33] Xiangdong Ji and J. Engel. *Physical Review C*, 40(2):496, August 1989.

[34] Xiangdong Ji and R.D. McKeown. *Physics Letters B*, 236(2):130, February 1990.

[35] T. G. O'Neill. PhD thesis, California Institute of Technology (unpublished), 1994.

[36] M. Traini and G.Orlandini. Sum rules for electron nucleus scattering. Universita di Trento, 1990.

[37] Paul Gueye. Private Communication.

[38] C. W. De Jager, H. De Vriesm, and C. De Vries. *Atomic Data and Nuclear Data Tables*, 14(5,6):479, Nov/Dec 1974.

[39] T.W. Donnelly and Stephen R. Cotanch. In *Research Program at CEBAF Report of the 1985 Summer Study Group*. CEBAF, January 1985.

VITA

Wendy LaTrece Hinton resigns at 685 Plater Street Aberdeen, Maryland, was born in Tacoma, Washington. She received her Bachelor of Science in physics from Washington and Lee University in 1991. She then worked for the Department of Defense Army Environmental Health Agency as as physical scientist for a year before returning to continue her studies in physics at Hampton University. She completed her Master of Science in 1995, and went on to study kaon electron production for her dissertation work which she completed in December 2000 to receive her Doctor of Philosophy in physics.